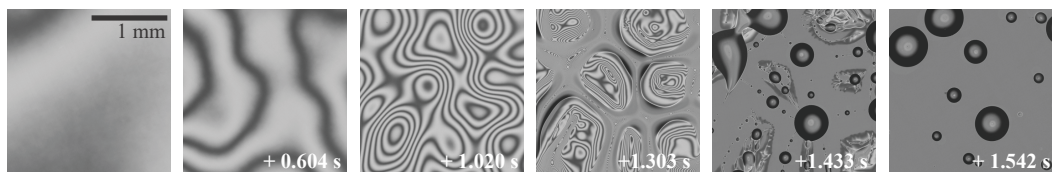

Experimental Study of Liquid Interfaces with Compositional Gradients

Distortion & Rupture of Ultra-Thin Films and Other Effects



DISSERTATIONSSCHRIFT

zur Erlangung des akademischen Grades

"doctor rerum naturalium"
(Dr. rer. nat.)

in der Wissenschaftsdiziplin "Physik weicher Materie"

Eingereicht an der

Mathematische-Naturwissenschaftliche Fakultät
Institut für Physik und Astronomie
der Universität Potsdam

von

Stephan Felix EICKELMANN

Eingereicht: Potsdam, 27. Juni 2018

Disputation: Potsdam, 12. November 2018

DOCTORAL ADVISORS:

Dr. habil. Hans RIEGLER

Max-Planck-Institut für Kolloid- und Grenzflächenforschung
Institut für Theorie und Bio-Systeme

&

Prof. Dr. Dieter NEHER

Universität Potsdam
Mathematische-Naturwissenschaftliche Fakultät
Institut für Physik und Astronomie

THIS WORK IS LICENSED UNDER A CREATIVE COMMONS LICENSE
Attribution-NonCommercial-NoDerivatives 4.0 International

To view a copy of this license visit
<https://creativecommons.org/licenses/by-nc-nd/4.0/>



PUBLISHED ONLINE AT THE MPG.PURE
(publication repository of the Max Planck Society)
<http://hdl.handle.net/21.11116/0000-0002-8B11-E>

DIGITAL OBJECT IDENTIFIER
DOI: 10.17617/2.3010222

“Goodbye, Jean-Luc. I’m gonna miss you...you had such potential. But then again, all good things must come to an end...”

UNIVERSITÄT POTSDAM

Zusammenfassung

Mathematische-Naturwissenschaftliche Fakultät

"doctor rerum naturalium"
(Dr. rer. nat.)

Experimental Study of Liquid Interfaces with Compositional Gradients Distortion & Rupture of Ultra-Thin Films and Other Effects

von Stephan Felix EICKELMANN

Der Inhalt dieser Arbeit ist die experimentelle Untersuchung von verdunstenden dünnen Filmen auf glatten Oberflächen, und die Anreicherung, das Kristallwachstum so wie Marangoni-Fluss in der Nähe der Dreiphasenlinie bei partiell benetzenden Mischungen aus flüchtigen und nichtflüchtigen Flüssigkeiten. Im Detail werden die Eigenschaften von planaren Flüssigkeitsfilmen und dünnen Flüssigkeitsabschnitten in der Nähe der dreiphasigen Kontaktlinie behandelt. In beiden Fällen verliert die Flüssigkeit kontinuierlich eine Komponente durch Verdampfung. Ein Thema ist das Entnetzungsverhalten ultradünner Filme aus binären Mischungen eines flüchtigen Lösungsmittels und eines nichtflüchtigen Stoffes. Dabei wird analysiert wie die Dicke, bei der der Film reißt, mit der Kristallisation des gelösten Stoffes an der Grenzfläche zwischen Flüssigkeit und Substrat in Verbindung steht, sobald der gelöste Stoff seine Übersättigung erreicht. Die Resultate dieses Projektes zeigen eine universelle Beziehung zwischen der Entnetzungsdicke und dem Sättigungsverhalten. Das zweite Forschungsgebiet sind einzelne Nanopartikel, die in molekular dünne Filme auf planaren Substraten eingebettet sind. Es zeigt sich, dass die Nanopartikel eine unerwartet

große Filmoberflächenverzerrung (Meniskus) verursachen. Diese Verzerrung kann durch herkömmliche Reflexionsmikroskopie quantitativ gemessen werden, obwohl die Nanopartikel viel kleiner als die Rayleigh-Beugungsgrenze sind. Untersuchungen mit binären Mischungen flüchtiger Lösungsmittel und nichtflüchtiger Stoffe (Polymere) zielen auf ein besseres Verständnis/Vorhersage der finalen Schichtdicke, zeitaufgelösten Verdünnung, zeitaufgelösten Verdunstung und der Entwicklung der Konzentration des gelösten Stoffes innerhalb des verdünnenden Filmes. Eine quantitative theoretische Beschreibung der experimentellen Ergebnisse wird hergeleitet. Unerwarteterweise zeigen die Experimente, mit vollständig mischbarer binärer Mischungen flüchtiger Flüssigkeiten, die einzeln glatte Filme bilden, dass Filme dieser Mischungen nicht notwendigerweise kontinuierlich und glatt sind. Vielmehr können sie Oberflächenwellen bilden oder sogar aufreißen. Dies wird mit Oberflächen-Marangoni-Strömungen erklärt.

Es wird eine neue Methode für die schnelle Herstellung von ultralang gerichteten Diphenylalanin-Einkristallen (Dip-Casting) (mm/min) vorgestellt. Dabei

wird gezeigt, wie die spezifischen Verdunstungsbedingungen an der Dreiphasenlinie für einen kontrollierten Peptidkristallwachstumsprozess verwendet werden können. Abschließend wird gezeigt, wie die Beschränkung innerhalb einer kleinen Kapillare die Peptidkristallisation beeinflusst, diese verstanden und verwendet werden kann.

UNIVERSITÄT POTSDAM

Abstract

Mathematische-Naturwissenschaftliche Fakultät

"doctor rerum naturalium"

(Dr. rer. nat.)

**Experimental Study of Liquid Interfaces with Compositional Gradients
Distortion & Rupture of Ultra-Thin Films and Other Effects**

by Stephan Felix EICKELMANN

The topic of this thesis is the experimental investigation of evaporating thin films on planar solid substrates and the enrichment, the crystal growth and Marangoni flows near the three phase line in the case of partially wetting mixtures of volatile and non volatile liquids. In short, it deals with the properties of planar liquid films and with those of thin liquid sections near the three phase contact line. In both cases the liquid loses continuously one component by evaporation.

One topic is the rupture behavior of ultra-thin films of binary mixtures of a volatile solvent and a nonvolatile solute. It is studied how the thickness at which the film ruptures is related to the solute crystallization at the liquid/substrate interface as soon as the solute reaches supersaturation. A universal relation between the rupture thickness and the saturation behaviour is presented. The second research subject are individual nanoparticles embedded in molecularly thin films at planar substrates. It is found that the nanoparticles cause an unexpectedly large film surface distortion (meniscus). This distortion can be measured quantitatively by conventional reflective microscopy although

the nanoparticles are much smaller than the Rayleigh diffraction limit. Investigations with binary mixtures of volatile solvents and non-volatile solutes (polymers) aim at a better understanding/prediction of the final solute coverage, the time-resolved film thinning, the time-resolved solvent evaporation, and the evolution of the solute concentration within the thinning film. A quantitative theoretical description of the experimental findings is derived. Experiments of completely miscible binary mixtures of volatile liquids, which individually form continuous planar films show unexpectedly that films of mixtures are not necessarily continuous and planar. Rather, they may form surface undulations or even rupture. This is explained with surface Marangoni flows.

A new method for the exceptionally fast fabrication (mm/min) of ultralong aligned diphenylalanin single crystals via dip casting is presented. It is shown how the specific evaporation conditions at the three phase line can be used for a controlled peptide crystal growth process. It is further demonstrated how the confinement inside a small capillary affects the peptide crystallization and how this can be understood (and used).

Contents

Zusammenfassung	ix
Abstract	xi
I Preface	1
1 Introduction	3
1.1 Motivation & Introduction	3
2 Theoretical Background	7
2.1 Interfacial Energies	7
2.1.1 Van der Waals interactions	7
2.1.2 Disjoining pressure	8
2.1.3 Laplace-Pressure and Capillary length	9
Laplace-Pressure	9
Capillary length	10
2.2 Wetting and Hydrodynamics	10
2.2.1 Contact angle and macroscopic wetting	10
2.2.2 Young-Dupé Equation	11
2.2.3 (De-)wetting mechanisms	11
2.2.4 Marangoni effect	12
Marangoni number	12
Marangoni wavelength	13
2.3 Hydrodynamic-evaporative film thinning (Spin Casting)	13
2.3.1 Pure volatile liquid	14
2.3.2 Dilute solutions	15
2.3.3 Sherwood number	16
2.3.4 Concentration and crystallization scenario for continuously thinning films	17
2.4 Nucleation and Growth	19
2.4.1 Homogeneous nucleation	20
2.4.2 Heterogeneous nucleation	20
2.5 Interference-enhanced imaging of ultra-thin films	20
3 Methods & Materials	23
3.1 Methods	23
3.1.1 Optical Microscopy for planar thinning films	23
Height reconstruction by interference pattern	24
Height reconstruction from the gray variation	25
3.1.2 Setup for Dip Casting	26

3.1.3	Setup for droplet experiments	27
	Contact angle measurements	27
3.1.4	Dry sample analysis	28
	Atomic force microscopy	28
	Ellipsometry	28
3.1.5	Liquid analysis	28
	Surface tension measurements	28
	Solubility	29
	Evaporation rate at zero velocity	29
3.2	Experimental procedures	29
3.2.1	Spin casting	29
3.2.2	Dip casting	29
3.2.3	Crystallization in a capillary	30
3.3	Materials	30
3.3.1	Solvents and Solutions	30
3.3.2	Substrates	30
	Cleaning and Preparation	31
II	Evaporating thin films on planar solid substrates	33
	Overview	35
4	Rupture of ultrathin solution films	37
4.1	Abstract	37
4.2	Introduction	38
4.3	Film rupture heights for mixtures of toluene/ $C_{36}H_{74}$	38
4.4	Film rupture heights for mixtures of $H_2O/NaHCO_3$	40
4.5	Film rupture thicknesses for various different binary mixtures	41
4.6	Discussion	42
4.7	Summary	45
4.8	Conclusion	45
5	Meniscus shape around nanoparticles	47
5.1	Abstract	47
5.2	Introduction	48
5.3	Optical footprints of NPs in various films thicknesses	49
5.4	Occurrence of optical footprints for different liquids	51
5.5	Meniscus profiles derived from the local gray levels	51
5.6	NPs embedded in solid polymer films	53
5.7	Meniscus geometries	54
5.8	Universal meniscus profile and distortion length L	56
5.9	Discussion	57
5.10	Conclusion	59
6	Deposition of polymer films by spin casting	61
6.1	Abstract	61
6.2	Introduction	62
6.3	"Zero-order" approach	63
6.4	Shortcomings of the zero-order approach	64

6.5	Thinning Behavior of Concentrate Polymer Solutions	65
6.6	Evaporation and Spin-Off	68
6.7	Speed depended Evaporation	70
6.8	Discussion	73
6.9	Conclusion	75
7	Thin Films with Lateral Surface Tension Gradients	77
7.1	Materials and Methods	77
7.2	Results	78
7.2.1	Film topography evolution of many different binary mixtures with component ratios of 90% to 10%	80
7.2.2	Film topography of mixtures with $\Delta\gamma > 0$ as a function of the mixing ratio	80
7.2.3	Evolution of the undulation wavelength as function of the ratio x_0	80
7.2.4	Evolution of undulation wavelength during film thinning as a function of time (thickness)	82
7.3	Discussion	82
7.3.1	Destabilization mechanism	82
7.4	Conclusion	83
III	Partially wetting mixtures: Crystal growth and Marangoni flows near the three phase line	85
	Overview	87
8	Self-assembly of ultralong aligned single crystals	89
8.1	Abstract	89
8.2	Introduction	90
8.3	Results and discussion	91
8.4	Conclusion	99
9	Directed self-assembly of single crystal in a capillary	101
9.1	Abstract	101
9.2	Introduction	102
9.3	Results and Discussion	103
9.4	Conclusion	108
IV	Conclusion, Outlook and Ongoing Work	111
10	Outlook	113
10.1	Film rupture for (less-)ideal mixtures	113
10.1.1	Behavior for very high concentrations $0.1c_{sat} < c_0 < 0.9c_{sat}$	113
10.2	Meniscus shape around nanoparticle	115
10.2.1	Reversible switching between different menisci	115
11	Conclusion	119

V Appendix	121
A Appendix A	123
A.1 Gray to Thickness	123
A.1.1 Fresnel Equations	123
A.2 Supporting information for Chapter 5	123
A.2.1 Analytical Expression of the Film Distortion	123
A.2.2 Surface Shape	124
A.2.3 Contact to the particle	125
A.2.4 Numerical Data Analysis	125
A.3 Supporting Information for Chapter 8	125
A.3.1 The influence of initial concentration of NH_4OH and tempera- ture on the structures of FF fibers.	125
A.3.2 Movie S1	127
A.3.3 Author information, Acknowledgments & Rights	127
A.4 Supporting Information for Chapter 9	129
A.4.1 Movie S1	129
A.4.2 Movie S2	130
A.4.3 Author information, Acknowledgments & Rights	130
A.5 Characterization methods for Chapter 8 and 9	130
A.5.1 Characterization of FF	130
A.5.2 Optical Waveguiding Property of the FF Single Crystal	131
Bibliography	137
Acknowledgements	151
Eidesstattliche Erklärung	153

For the most important person...

Part I

Preface

Chapter 1

Introduction

1.1 Motivation & Introduction

Tears of wine[1, 2], ouzo effect[3], bubble nucleation in a pint of beer[4], the chocolate blooming on a cake[5], and the coffee stain on the kitchen table[6], all these phenomena have been observed by most of us. They have one thing in common: They all are dominated by interfacial effects. Interfacial effects induce flows caused by surface tension gradients, the non-trivial solubility of ternary systems leading to emulsification and they affect the nucleation and growth of new phases. Of course there are ongoing strong fundamental research activities in the field of interfacial phenomena.

An area where interfacial phenomena are quite important are ultra (molecularly) thin films. Thin films (coatings) are basic ingredients in many applications, such as in electronics devices, solar cells, optical coatings. They also play an important role in painting, window cleaning, etc. Although thin films can be found everywhere, in many cases it is not completely understood how thin films finally form a desired final coating/casting? Often studies only try to find the proper parameters for a desired coating result by trial and error without aiming at a deeper understanding of the processes. If the aim is a thin film coating with a precise thickness, or a controlled deposition of layers of particles, the fundamental knowledge of the film forming mechanisms can be very important. The thinner a final film becomes, the more important become for instance the surface properties of the supporting interface. Dewetting, film rupturing, and film deformation can be the result of the substrate chemistry and topology. In short, to gain a desired result, we should understand the fundamental film forming mechanism to be able to better control the outcome.

There are a number of processes to manufacture thin films and coatings. This study will focus on film formation with the help of solvent evaporation. Two of the most common methods for this type of thin film formation are spin casting (spin coating) and dip casting (dip coating) from solutions with a volatile solvent. In the case of spin casting a certain amount of solution is deposited on a rotating substrate. The combination of radial and hydrodynamic (viscous) forces will flatten the deposited liquid and form a planar film. Through evaporation of the solvent this planar liquid film will continuously become thinner. With a nonvolatile component the finally result is a dry coating of the substrate. Dip casting is the withdrawing of a substrate from a bulk solution. At the three phase line the solvent will drain and evaporate from the substrate. As result a dry coating remains.

Several key questions are linked to these methods. How do these thin films evolve until we end up with a dry coating? How does solute enrichment or even solute precipitation affect the thinning of the film? What is the topography of a thinning film on a substrate with small (nano-size) objects? How does the film evolve and how can the coverage be predicted in the case of a binary mixture with a polymer as nonvolatile solute? What are the impacts of compositional gradients in thinning binary mixtures? How can a self-assembly process like crystal growth be directed and controlled if it occurs in thinning films?

High speed cameras nowadays allow optical real-time microscopy optical imaging during the film formation process[7–9]. This gives on-line insights into processes of the film formation, which before could only be concluded indirectly based on phenomena observed after the film formation ([10–20]) or studied with help of simulations[21–24]. The essential investigation technique of this work is a home build on-line optical microscopy setup, which allows the on-line observation during film formation via spin and dip casting with millisecond time resolution and with a spatial resolution of μm (laterally) and nm (vertically).

Within this thesis the presentation of the results is sectioned into two parts. The first part (*Evaporating thin films on planar solid substrates*) deals with continuously evaporating planar films in a spin cast configuration. The second part (*Partially wetting mixtures of volatile and non volatile liquids: Enrichment, crystal growth and Marangoni flows near the three phase line*) focuses on (directed) crystallization processes in the vicinity of a (moving) three phase line.

Chapter 4 investigates the rupture behavior of ultra-thin films of binary mixtures of a volatile solvent and a nonvolatile solute. The pure solvent completely wets the substrate. Unexpectedly, the solution films rupture at certain film thicknesses. It is investigated how this rupture depends on the solute crystallization at the liquid/substrate interface. *Chapter 5* looks at individual nanoparticles embedded in molecularly thin films at planar substrates. The focus is on the resulting film surface distortion (meniscus) adjacent to the nanoparticles. It is shown that conventional reflection microscopy can be used to measure and analyze the shape of the meniscus. In *Chapter 6* binary mixtures with non-volatile solutes (polymer) are studied. Through the polymer enrichment in the course of the evaporative thinning, the hydrodynamic and evaporative properties of the film change drastically. It is investigated how the final solute coverage, time-resolved film thinning, time-resolved solvent evaporation, and the evolution of the solute concentration within the thinning film occurs. *Chapter 7* presents experiments with completely miscible binary mixtures of volatile liquids. Both liquids individually wet the surface completely and form continuous thinning films until the substrate is completely dry. However, under certain conditions mixtures of such liquids may form films, which become unstable, form undulations and even rupture during the evaporative film thinning.

In the second part of the results section of this work different procedures for the controlled assembly of the dipeptide diphenylalanine into aligned single crystals are investigated. *Chapter 8* describes a new method for the exceptionally fast fabrication (mm/min) of ultralong aligned dipeptide single crystals via dip casting. The specific evaporation conditions at the three phase line allow for a better control of the peptide growth process. In *Chapter 9* the crystallization of the dipeptide inside of

a thin capillary is studied. The precipitation under confinement allows a certain control of the growth of the crystals.

The final part of this thesis (*Part IV Conclusion, Outlook and Ongoing Work*) presents the conclusion, outlook and ongoing work. Substantial parts of this thesis have already been published in scientific journals. This is described in more detail at the beginning of the respective chapters. Also, at beginning of each chapter a detailed description of the author contributions to these publications is presented. Details of the experimental procedures are described in Chapter 3. Additional supporting information can be found in Appendix A. The scientific concepts of interfacial interactions relevant for the understanding of the result interpretations, such a wetting phenomena, nucleation & growth, and a short introduction on hydrodynamic-evaporative film thinning (spin casting)[25] are presented in *Chapter 2*.

Chapter 2

Theoretical Background

2.1 Interfacial Energies

An interface is the zone separating two immiscible, condensed phases (e.g. liquid/solid, liquid/liquid or solid/solid). If one of the phases is a gas, the interfacing region is called surface. The interface (surface) region has a finite thickness (usually smaller than sub-microns) and composition and energy vary continuously from one phase to the other. Unlike in the bulk, the pressure (force field) in the interfacial zone is inhomogeneous, having a gradient perpendicular on the interface. A consequence of this is that a net energy is required to create an interface by the reversible transition of matter from the bulk to the interfacial zone. The reversible work needed to create a unit interface area is the interfacial tension, γ_{AB} :

$$\gamma_{AB} \equiv \left(\frac{\partial G}{\partial A} \right)_{T,p,n} \quad (2.1)$$

with G the total Gibbs free energy, A the interfacial area, T the temperature, p pressure, and n the total number of moles of matter in the system. The expression surface tension (force per unit length) is generally used for liquids. It is dimensionally the same as surface energy (energy per unit area), which is commonly used for solids.

2.1.1 Van der Waals interactions

The denotation *Van der Waals* interactions summarizes the long ranging *London*-, *Kessom*- and *Debye*-interactions. All three contributions are commonly summed up, since they are acting on the same length dependence. These contributions account for the material specific *Hamaker* coefficient. Most commonly the *Lenard-Jones-potential* is used to determine the long and short ranged interactions between uncharged molecules/atoms.[26]

In systems without charged particle all interactions are van der Waals interactions. They originate from permanent, induced and spontaneous dipole interactions. *Debye*-interactions between permanent and induced dipoles with the permanent dipole moment of a molecule μ and the polarization α :

$$W_{ind}(r) = -\frac{C_{ind}}{r^6} = -\frac{\mu^2\alpha}{(4\pi\epsilon_0)^2r^6} \quad (2.2)$$

Kessom-interactions are interaction between permanent dipoles μ_1 and μ_2 . The forces are dependent on the orientation of the molecules. This varies because of thermal movement, but can be averaged on the relative orientation with a temperature dependent pre-factor.

$$W_{orient}(r) = -\frac{C_{orient}}{r^6} = -\frac{\mu_1^2 \mu_2^2}{3(4\pi\epsilon_0)^2 k_b T r^6} \quad (2.3)$$

London-interactions describe the interaction between spontaneous dipole moments with the polarizability α_1 and α_2 . The spontaneous polarization of molecules are a result of electro movement in the shell. This quantum mechanic effect causes attractive interactions:

$$W_{disp}(r) = -\frac{C_{disp}}{r^6} = -\frac{3hv_1v_2}{2(v_1+v_2)} \frac{\alpha_1\alpha_2}{(4\pi\epsilon_0)^2 r^6} \quad (2.4)$$

The sum of all three interactions defines the *van der Waals*-interactions. In literature the constant of proportionality is summarized by C .

$$W_{vdW}(r) = -\frac{C_{ind} + C_{orient} + C_{disp}}{r^6} = -\frac{C_{vdW}}{r^6} \propto -\frac{1}{r^6} \quad (2.5)$$

2.1.2 Disjoining pressure

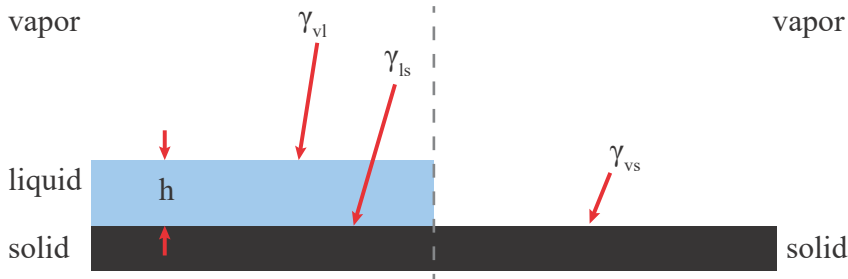


FIGURE 2.1: On the left a thin, liquid film between a solid and a vapor phase vs. the vapor directly in contact with the solid, and indication of the surface energies corresponding to the various interfaces.

The cartoon in Figure 2.1 depicts on the left a thin, liquid film between a solid and a vapor phase against the vapor directly in contact with the solid. The thickness of the liquid film is h , and the various γ_{xy} describe the corresponding surface energies. The total energy density depends on $P(h)$ of film thickness h :

$$\frac{W}{A} = \gamma_{sl} + \gamma_{lv} + P(h) = \Delta\gamma + P(h) \quad (2.6)$$

(With W as an Energy, and A an area) $P(h)$ arises from the molecular interactions, like van der Waals, electrostatic-, ionic-, and/or metallic interactions. It becomes more important as the film thickness h approaches the length scales of the respective interactions. If the film thickness is taken to zero, we get the energy of the bare surface minus the surface energies of the solid/liquid and liquid/vapor interfaces: $h \rightarrow 0 : \frac{W}{A} = \gamma_{sv} + \gamma_{sl} - \gamma_{lv}$

In the other limit where the film is extremely thick, the thickness of the film does not matter, and the only energy will come from the interfaces: $h \rightarrow \infty : \frac{W}{A} = \gamma_{sl} - \gamma_{lv}$. The disjoining pressure (Π) describes the extra bit of pressure that results from the molecular interactions when both interfaces come close.

$$\Pi(h) = -\frac{dP(h)}{dh} \quad (2.7)$$

This pressure may have either positive or negative values. If the disjoining pressure is positive, the system is stable and the thin film will not de-wet. If the disjoining pressure is negative, the system becomes unstable, and de-wetting can occur for a thin film.

Van der Waals interactions between the two interfaces are described with the Hamaker coefficient A_{ij} [27]:

$$P(h) = -\frac{A_{ij}}{12\pi h^2} \quad (2.8)$$

Assuming only van der Waals interactions (no electrostatics etc.) this leads to a disjoining pressure:

$$\Pi_D = -\frac{1}{A} \left(\frac{\partial G}{\partial h} \right) \quad (2.9)$$

For example liquids like toluene, nonane and water wet a silica surfaces completely. They build a stable film. Precipitation of a solute or a local defect in the solid surface can change the van der Waals interactions and induce a non-stable system, which de-wets.

2.1.3 Laplace-Pressure and Capillary length

Laplace-Pressure

A curved interface shows, in addition to its static pressure, an extra pressure component, resulting from the surface tension, referred to as the *Laplace-Pressure*. This pressure results from the tangential forces, which span the curved surface and are at an angle $\neq 0$ to another. This causes a force opposite to the direction of the radius of curvature.

For a spherical droplet in a surrounding phase with the pressure p_{out} , the following term is obtained for the pressure difference:

$$\Delta p = p_{in} - p_{out} = \frac{2\gamma}{r} \quad (2.10)$$

γ is the surface tension, and r the radius of the droplet with the inner pressure p_{in} . The *Laplace-Equation* for a 2-dimensional potential $z(x, y)$ describes the equilibrium conditions for arbitrarily curved surfaces.

$$\frac{d^2z}{dx^2} + \frac{d^2z}{dy^2} = 0 \quad (2.11)$$

This leads to an universal expression for the Laplace-pressure, which describes the change in hydrostatic pressure at the interface between two phases with the interfacial curvature. With R_1 and R_2 as the curvatures of the interface in Figure 2.2(a).

$$\Delta p = \gamma \underbrace{\left(\frac{1}{R_1} + \frac{1}{R_2} \right)}_{\text{interfacel curvature}} \quad (2.12)$$

Capillary length

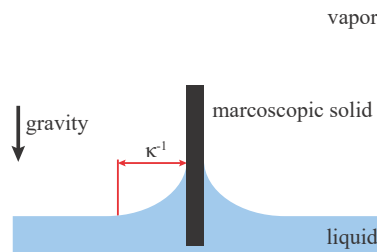


FIGURE 2.2: Showing the characteristic length of menisci for a completely wetting macroscopic object sticking in a liquid.

The length scale κ^{-1} marks the crossover between gravitational forces and interfacial forces is called *Capillary length*.

$$\kappa^{-1} = \sqrt{\frac{\gamma}{\rho g}} \quad (2.13)$$

where g is gravity, ρ the density of the liquid and γ its liquid/vapor surface tension. A typical capillary length, (e.g. for water) is $\kappa^{-1} \simeq 2.7$ mm. All experiments in the following chapters were far under this length. Thus, gravity can be neglected.

2.2 Wetting and Hydrodynamics

2.2.1 Contact angle and macroscopic wetting

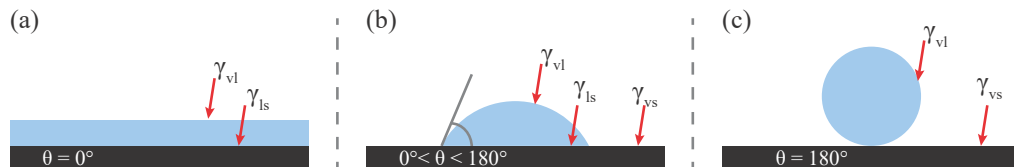


FIGURE 2.3: The contact angle θ is a macroscopic measure of the wettability of a surface: (a) complete wetting: $\theta = 0^\circ$, (b) partially wetting $0^\circ < \theta < 180^\circ$ and non-wetting $\theta = 180^\circ$

A liquid is considered (*partial-*)wetting, if the adhesion between liquid and solid substrate is bigger than the cohesion inside the liquid itself. The contact angle θ

describes the angle at the contact line between liquid, solid and vapor phase of a droplet (Fig.2.3 & 2.4).

Complete wetting is, when a liquid wets the complete surface, shown in Figure 2.3(a). If the contact angle is between 0° and 180° the liquid is considered *partial wetting*¹ (Fig.2.3(b)). In case of a contact angle of 180° the solid is *non-wetting* (Fig.2.3(c)).

2.2.2 Young-Dupé Equation

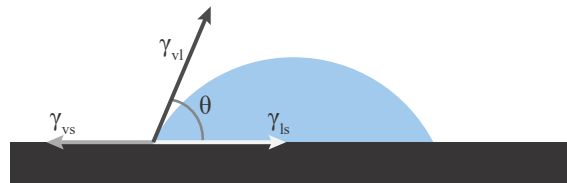


FIGURE 2.4: The Young-Dupé Equation allows the description of partially wetting surfaces of liquid/solid interfaces.

If partially wetting phases come into contact with a solid surface, a *three phase line* will be formed (Fig.2.3). In equilibrium, the relation between the various interface tensions and contact angle is handled by the *Young-equation*:

$$\gamma_{VS} = \gamma_{LS} + \gamma_{VL} \cdot \cos(\theta) \quad (2.14)$$

2.2.3 (De-)wetting mechanisms

Two mechanisms are known to induce de-wetting: *nucleation* and *spinodal* de-wetting [18, 29, 30]. In the case of spinodal de-wetting, capillary waves form on the surface

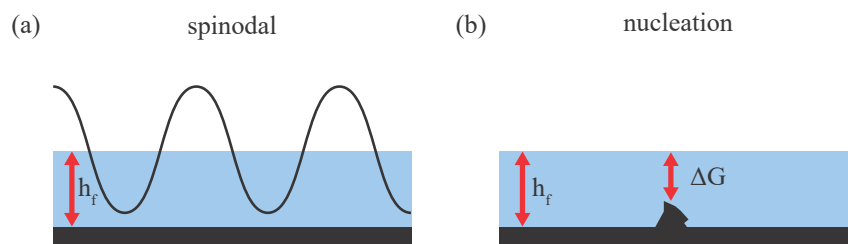


FIGURE 2.5: (a) Capillary waves may touch the solid interface and cause dewetting without an energy barrier. (b) a small defect lowers locally the energy barrier of the film and can act as a nucleation side for dewetting.

of the film. When the amplitude of these waves reaches the average film height, a de-wetting hole may spontaneously occur (no energy barrier) shown in Fig.2.5(a). In the nucleation and growth mechanism, an impurity in the film or on the substrate (e.g. scratch, dust, or other imperfections) acts as a nucleation site for the growth of a hole in the film (energy barrier) as shown in Fig.2.5(b).

¹In literature, it is sometimes distinguished between partially wetting $0^\circ - 90^\circ$ and partially non-wetting $90^\circ - 180^\circ$ [28]

2.2.4 Marangoni effect

The *Marangoni effect* describes a flow caused by a surface tension gradient, in vicinity of an interface.[1, 2] A surface tension gradient can be result of a temperature gradient² or a concentration gradient³ (eg. solute, surfactant, or binary liquid mixture[31]) as illustrated in Figure 2.6.

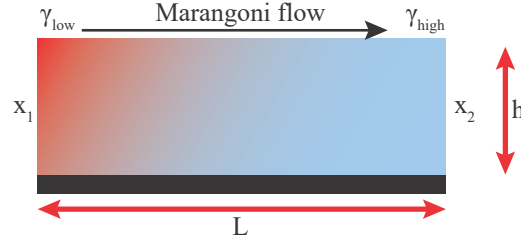


FIGURE 2.6: Schematic cartoon depicting the marangoni flow as a result of a surface tension gradient.

Marangoni number

The marangoni number is defined by the ratio of driving force caused by surface tension and a breaking force due to viscosity.

$$Ma = \frac{F_\gamma}{F_\eta} \quad (2.15)$$

In a binary mixture the surface tension is a function of the composition. We first have considered a 2 dimensional problem[32]. As in Figure 2.6 shown, we can consider a thin film of thickness h . On the lateral length, we have locally two different compositions x_1 and x_2 with a distance L . A characteristic time scale τ for this system is defined by diffusive mass transport ($D = L^2/\tau$). Thus, for the movement of molecule/particle along this distance, we can write down the following:

$$\partial r = v \cdot \tau \cdot \frac{h}{L} \quad (2.16)$$

The difference of compositions between both sides (with $\Delta x_{w/w} = x_2 - x_1$):

$$\frac{\partial x_{w/w}}{\partial r} \cdot \frac{\partial r}{\partial \tau} = \frac{\Delta x_{w/w}}{L} \cdot v \cdot \tau \quad (2.17)$$

Thus the driving force follows:

$$F_\gamma = L \cdot \frac{\partial \gamma}{\partial x_{w/w}} \cdot \frac{\partial x_{w/w}}{\partial r} \frac{\partial r}{\partial \tau} = \frac{\partial \gamma}{\partial x_{w/w}} \cdot v \cdot \tau \cdot \Delta x_{w/w} \quad (2.18)$$

²the phenomenon is called thermo-capillary convection also known as Beñard-Marangoni convection

³Solutal Marangoni

This will be countered by viscosity.

$$F_{\eta} = \frac{\eta \cdot v}{h} \cdot L^2 \quad (2.19)$$

This force is inverse proportional to the film thickness, increasing its strength in a thinning scenario. This both forces then lead the definition for a solutal marangoni number as followed:

$$Ma^x = \frac{F_{\gamma}}{F_{\eta}} = \frac{\partial \gamma}{\partial x_{w/w}} \frac{\Delta x_{w/w} \cdot h}{\eta D} \quad (2.20)$$

with D the diffusion coefficient, $\Delta x_{w/w}$ - concentration difference, γ surface tension and η the dynamic viscosity.⁴

To cause an instability, the driving force has to overcome the breaking force, thus a Marangoni number > 1 is needed. Typically, $Ma < 80$ show no instabilities. However, for a thinning film, it depends how quickly it thins. If this is a very fast process, the marangoni flow has no time to cause an instability. But if the drying is slower, already a small $Ma \approx 40$ can lead to an instability of the film.

Marangoni wavelength

[33] An fast and easy way to quantify a Marangoni instability of a planar film is to measure the characteristic wavelength of the resulting undulations, (Fig. 2.7).

$$\lambda = 2\pi \cdot \frac{h_{Ma}}{\sqrt{\frac{Ma}{8}}} \quad (2.21)$$

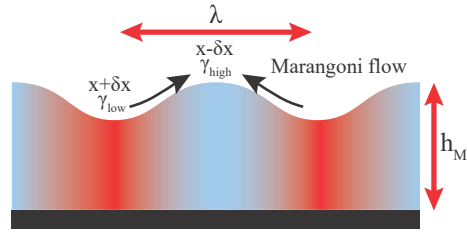


FIGURE 2.7: Depending on the thickness h_{Ma} , convection cells with a wavelength λ appear.

2.3 Hydrodynamic-evaporative film thinning (Spin Casting)

In a spin cast configuration film thinning as well as the evolution of the solvent composition are meanwhile quantitatively well understood for mixtures of non-volatile

⁴This is analog to the typical thermal Marangoni number: $Ma^T = -\frac{\partial \gamma}{\partial T} \frac{L \Delta T}{\eta a}$ with L as a characteristic length scale of the system, a the thermal diffusion coefficient, ΔT - Temperature difference, γ surface tension and η the dynamic viscosity.

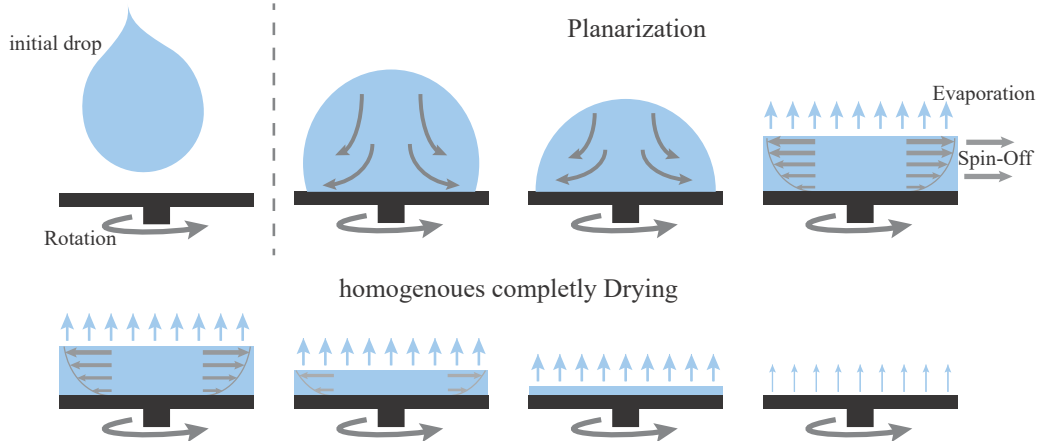


FIGURE 2.8: Schematic of the spin cast process for a completely drying liquid.

solutes and volatile solvents [8, 25, 34]. All thinning films were prepared and investigated under constant rotation speed. A small amount of liquid ($\approx 200\mu\text{l}$ = "excess volume", see [25, 34]) is deposited on the rotating planar substrate. Right after liquid deposition the interplay of hydrodynamics and viscous forces planarizes the liquid into a flat film [35]. With volatile liquids this planar film is continuously thinning due to hydrodynamically driven flow as well as evaporation [36]. Whereas at the beginning, with relatively thick films, the film thinning is dominated by hydrodynamics, at later stages its thinning is dominated by evaporation. The crossover between hydrodynamic and evaporative film thinning occurs at the so-called transition height h_{tr} [25]:

2.3.1 Pure volatile liquid

Thinning of a film on a rotating supporter was theoretical first described by Emsli et al. [35] in 1958. The focus was on a non-volatile solvent and described the hydrodynamic process. An ideal Newtonian viscous liquid with the typical fluid dynamic boundary conditions was assumed – no evaporation, no slip etc. The time evolution of the height of a uniform film on a rotation support is:

$$\frac{dh}{dt} = -2Kh^3 \quad (2.22)$$

The spin-off coefficient K includes the kinematic viscosity ν and therefore the viscosity η and density ρ . ω is the rotational velocity (including the frequency f):

$$K = \frac{\omega^2}{3\nu} = \frac{4\pi^2 f^2 \rho}{3\eta} \quad (2.23)$$

This is solved analytically for the film thickness evolution:

$$h(t) = \frac{h_0}{\sqrt{1 + 4Kh_0^2 \cdot t}} \quad (2.24)$$

With the initial film height h_0 at $t = 0$. In the following years this approach was extended by Acrivos [37] for non-Newtonian liquids. This approach completely neglects evaporation.

In 1987 Meyerhofer [36] addressed evaporation. He added a constant evaporation rate E to equation 2.22:

$$\frac{dh}{dt} = -2Kh^3 - E \quad (2.25)$$

He presented only a numerical solution for this equation. It showed that in the beginning hydrodynamic flow dominates thinning. Later evaporation dominates the process. Subsequently, more authors presented in more detail the relation between film thinning and rotational speed [38], solvent evaporation [39, 40], viscosity [40–42], heat transfer [43], molar mass [44], or initial solution concentration [45]. Despite plenty of research activity aiming on spin casting, an analytical solution of this equation was not presented in literature. In order to solve the equation 2.25 Kapitschka et al. [25] wrote its fundamental form

$$\frac{d\tilde{\zeta}}{d\tau} = -\tilde{\zeta}^3 - 1 \quad (2.26)$$

which is obtained by rescaling with $\tilde{\zeta} = h/h_{tr}$ and $\tau = t/t_{sc}^*$, the system inherent "natural" scales:

$$h_{tr} = (E/2K)^{1/3} \quad (2.27)$$

$$t_{sc}^* = (2E^2K)^{-1/3} \quad (2.28)$$

h_{tr} is the transition height when evaporation and hydrodynamic thinning are equal. t_{sc}^* represents the "reduced" process duration. This relation is monotonous and can be inverted. This leads to an ordinary linear differential equation of zeroth order ($\frac{\tau}{d\tilde{\zeta}} = \frac{1}{-\tilde{\zeta}^3-1}$), which can be solved:

$$\tau(\tilde{\zeta}) = \frac{\sqrt{3}}{6} \left\{ \pi + 2 \arctan \frac{1-2\tilde{\zeta}}{\sqrt{3}} + \frac{1}{\sqrt{3}} \log \frac{1-\tilde{\zeta}-\tilde{\zeta}^2}{(1+\tilde{\zeta})^2} \right\} \quad (2.29)$$

The duration of the process (starting at $h \rightarrow \infty$, ending $h = 0$) is: It is found that always hydrodynamic film thinning dominates 30% of the spin cast time in the beginning and then 70% of the film thinning is driven by evaporation.

$$t_{sc} = \frac{2\pi}{3^{3/2}} (2E^2K)^{-1/3} = \frac{2\pi}{3^{3/2}} \cdot t_{sc}^* \quad (2.30)$$

2.3.2 Dilute solutions

Practical application of spin casting includes the enrichment and deposition of solute, which is caused by evaporation. Non-volatile solute will be enriched on the vapor/liquid interface due to evaporation, which migrates through the film due to diffusion. The spatio-temporal evolution of the solute concentration c is described by:

$$\partial_t c = D \partial_z^2 c + Kz^2(3h-z) \partial_z c \quad (2.31)$$

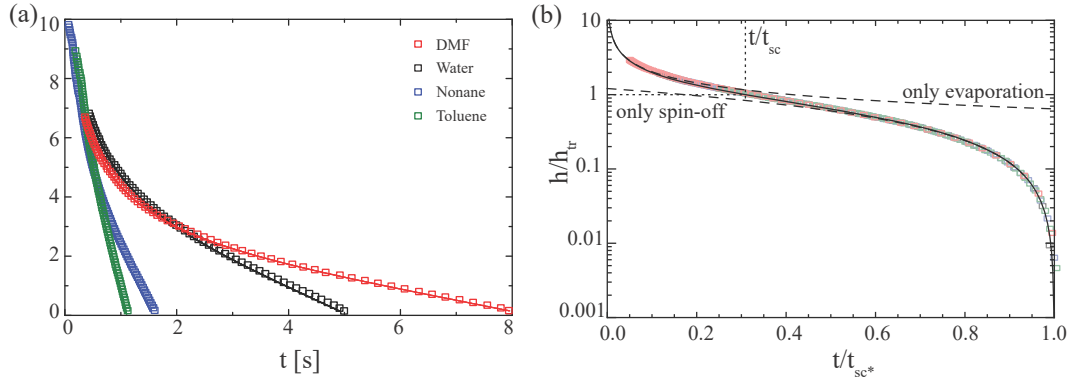


FIGURE 2.9: (a) shows the thickness evolution of various solvents. The solid line indicates the fit of equation 2.29. (b) shows the universal thinning behavior of the same data. Rescaled with the transition height h_{tr} and process time t_{sc} .

With the boundary conditions⁵ $D\partial_z c|_{x=h'} = Ec|_{z=0} = 0$

$$\Phi dz = 2\pi r u(r, z) dz = 6\pi K r^2 z (h - z/2) dz \quad (2.32)$$

This yields in combination with the continuity equation the thinning induced vertical motion of the horizontal stream lines:

$$\frac{dZ}{dt} = -\frac{1}{2\pi r} \int_0^z \partial_r \Phi dz' = -Kz^2(3h - z) \quad (2.33)$$

To solve equation 2.31 $h(t)$ is required, but not known explicitly, only its inverse, $t(h) \rightarrow \tau(\xi)$. Because it is bijectiv, the variable can be transformed to:

$$\partial_t c = \frac{d\tau}{dt} \cdot \frac{d\xi}{d\tau} \cdot \partial_\xi c = -(2E^2 K)^{1/3} (\xi^3 + 1) \partial_\xi c \quad (2.34)$$

In order to avoid the moving boundary, the system is rescaled (between substrate and surface) with $y = z/h \in [0, 1]$. Which leads to:

$$\partial_\xi c = -\frac{\partial_y^2 c}{Sh_{tr} \xi^2 (\xi^3 + 1)} - \left\{ \frac{(\xi y)^2 (3 - y)}{2(\xi^3 + 1) - \frac{y}{\xi}} \right\} \partial_y c \quad (2.35)$$

$$\partial_y c|_{y=1} = Sh_{tr} \xi c|_{y=1}, \partial_y c|_{y=0} = 0 \quad (2.36)$$

2.3.3 Sherwood number

The Sherwood number Sh_{tr} at $h = h_{tr}$, parameterizes the ratio of evaporation to diffusive mass transport on the characteristic length scale of the system, the transition height.

$$Sh_{tr} = (E \cdot h_{tr}) D^{-1} = E^{4/3} (2K)^{-1/3} D^{-1} \quad (2.37)$$

⁵Stefan Condition [46]

By scaling c with the initial solute concentration c_0 , the initial condition is $c|_{\xi \rightarrow \infty} = 1$, the system is parameterized completely by Sh_{tr} . With ξ as independent variable, equation 2.35 can be solved numerically. Together with equation 2.29 it provides τ as function of ξ thus finally providing $c(t, z)$.

The Sherwood number Sh_{tr} reveals the competition between solute enrichment due to evaporation, solvent/solute loss due to spin-off, and diffusive dilution. In general, larger Sh_{tr} means more produced gradients in c . If $h \gg h_{tr}$ solute enrichment occurs only locally near the free surface and $c = c_0$ near to the substrate. If $h \ll h_{tr}$, c also increases near the substrate. $Sh_{tr} = 1$ and $h = h_{tr}$ marks the transitions: The solute gradient just reaches the film/substrate interface and c just begins to increase globally.

For $Sh_{tr} \ll 1$ diffusion dominates and c is mostly homogeneous (Fig. 2.10(a)). The final solute coverage for $Sh_{tr} < 1$ is (in agreement with equation 2.35):

$$\Gamma = \frac{N(h \rightarrow 0)}{A} \approx c_0 \cdot h_{tr} \quad (2.38)$$

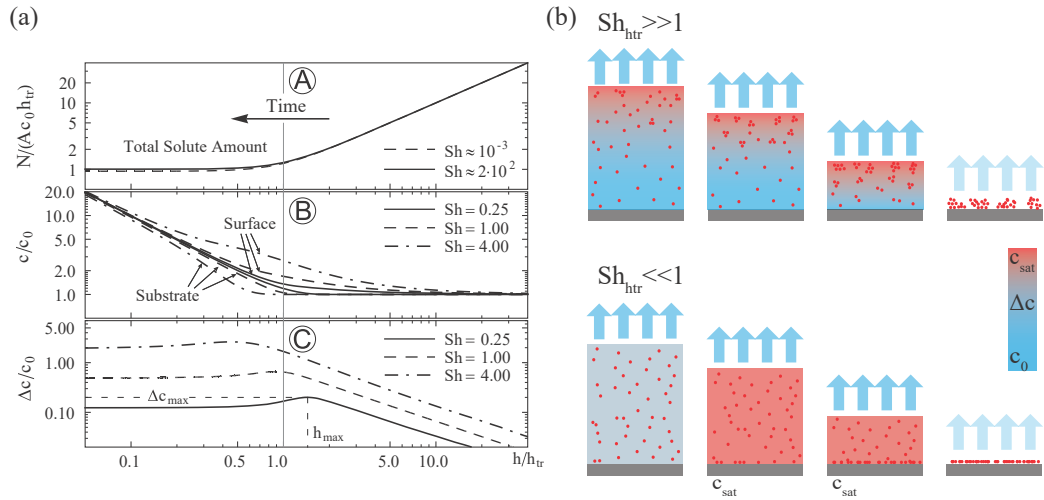


FIGURE 2.10: (a) taken from (Ref. [25]). (b) shows the influence of diffusion speed on the solute distribution inside a thinning film.

2.3.4 Concentration and crystallization scenario for planar, continuously thinning solution films

With typical evaporation rates of $E = 1.5 \mu\text{m/s}$ and typical spin cast parameters of $K = \omega^2/(3\nu) = 5 \cdot 10^{-9} \text{mm}^{-2}\text{s}^{-1}$ ($\omega = 1000 \text{rpm}$, $\nu = 0.65 \text{mm}^2/\text{s}$) h_{tr} is in the range of a few μm . Therefore, as soon as the films are thinner than $\approx \mu\text{m}$ the time evolution of the film thickness is dominated by evaporation.

If the liquid film consists of a mixture of a volatile solvent and a nonvolatile solute the solvent will evaporate and the solute will continuously get enriched until it remains on the substrate as a final deposit. Because the solvent evaporates from the

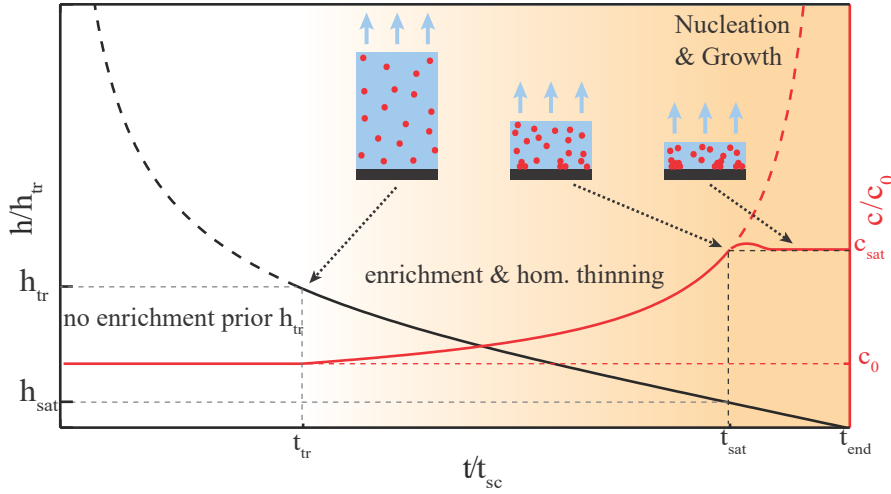


FIGURE 2.11: Schematic of the film thinning behavior and the concentration evolution in the case of a mixture of a volatile solvent and a non-volatile solute. A homogeneous vertical solute distribution is assumed during solute enrichment as result of the continuous solvent evaporation (i.e., $Sh_{tr} < 1$, which is the case in most practical cases).

film surface the solute primarily gets enriched near the surface. However, this local solute enrichment is counterbalanced by dilution through diffusion away from the surface. The competition between solute enrichment through the loss of solvent via E and solute dilution through diffusive transport quantified through its diffusion constant D can be estimated by a Sherwood number. The Sherwood number for the largest relevant distance, Sh_{tr} , i.e., on the length scale of a film with the thickness of the transition height h_{tr} is:

$$Sh_{tr} = (E \cdot h_{tr})D^{-1} = E^{4/3}(2K)^{-1/3}D^{-1} \quad (2.37)$$

If $Sh_{tr} < 1$, even though the solute enrichment primarily occurs near the film surface, diffusive dilution is very efficient and effectively the vertical solute distribution is rather homogeneous. If $Sh_{tr} < 1$, i.e. it is small for a film thickness of h_{tr} , it is even smaller for thinner films (the distribution within thinner films is even more homogeneous [25]). Typical Sherwood numbers⁶ Sh_{tr} for the various solvent/solute systems investigated in this report are significantly smaller than 1. Therefore, it can be assumed that the vertical distribution of the solute remains rather homogeneous during the entire process of evaporative film thinning respectively solute enrichment. Assuming continuous homogeneous solute enrichment Figure 2.11 depicts the essential relations between film thinning, solute enrichment, nucleation and growth as it occurs during spin casting of a mixture of a volatile solvent and a nonvolatile solute. It shows the film thickness and the solute concentration as function of the time between the transition time, t_{tr} , and complete drying at $t = t_{end}$. As discussed earlier, for $h_f \ll h_{tr}$ the film thickness decreases due to solvent evaporation approximately

⁶ $Sh_{tr}(C_{36}H_{74}/toluene) \leq 0.037$, $Sh_{tr}(C_{30}H_{60}/toluene) \leq 0.031$, $Sh_{tr}(C_{36}H_{74})/MCH \leq 0.110$, $Sh_{tr}(C_{36}H_{74}/nonane) \leq 0.008$ and $Sh_{tr}(NaHCO_3/H_2O) \leq 0.0003$ [47]. Diffusion coefficients from Stokes-Einstein-Relation [48]: $D = k_B T / 6\pi\eta R_0$ (with $R_0 = \sqrt{l^2/12}$ for $C_{30}H_{62}$ and $C_{36}H_{74}$ as cylindrical molecules with lengths of $\sim 4.6\text{nm}$ and $\sim 5.6\text{nm}$).

linearly with:

$$h(t) \simeq h_{tr} - E \cdot t \quad (2.39)$$

At the same time the solute concentration in the film, $c(h)$, increases with (c_0 is the weighing in solute concentration):

$$c(h) \simeq c_0 \cdot (h_{tr}/h) \quad (2.40)$$

This means that the solute concentration reaches its saturation value, c_{sat} , at a film thickness h_{sat} (at a time t_{sat}):

$$h_{sat} \simeq c_0 \cdot (h_{tr}/c_{sat}) \quad (2.41)$$

With a nucleation barrier, right after t_{sat} , the solute concentration will temporarily exceed c_{sat} until it overcomes the nucleation barrier and the solute starts to crystallize. Then the solute concentration will decrease to c_{sat} and remain at this value until the system gets completely dry.

2.4 Nucleation and Growth

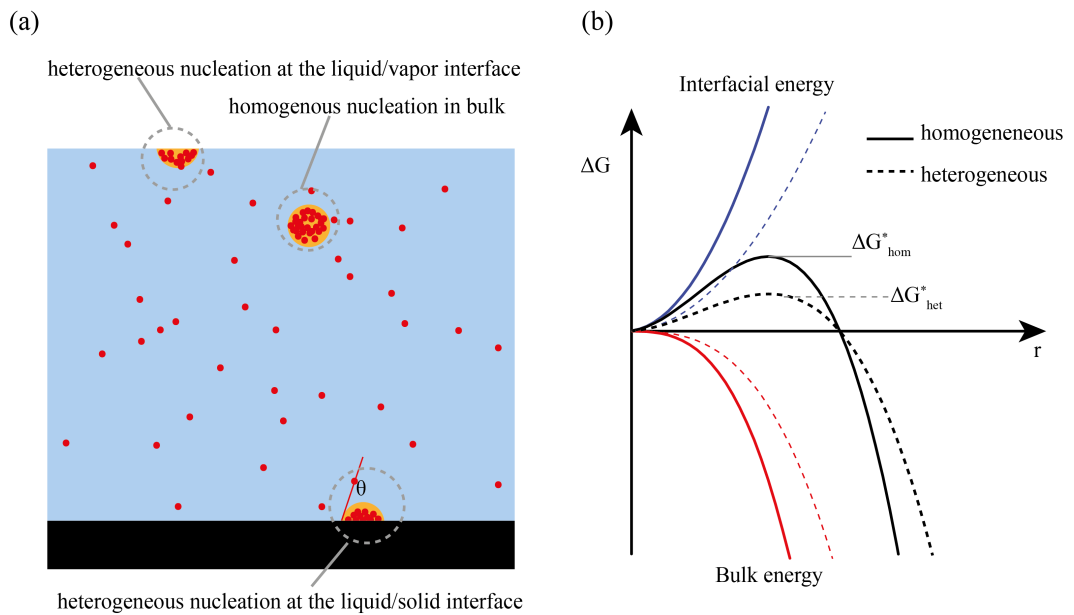


FIGURE 2.12: (a) shows heterogenous and homogenous nucleation behaviors at different locations. (b) shows the competition of bulk and interfacial energy, resulting in the nucleation barrier

The nucleation process is described as a competition of bulk energy (ΔG_{bulk}) and interfacial free energies ($\Delta G_{interface}$). The total free energy of the system will first increase and then decrease with the proceeding of the phase transition, and an energy barrier keeps the supersaturated old phase metastable. The height of the barrier can be calculated for the individual nucleation process. Depending on the location of the nucleation, there is homogeneous nucleation and heterogeneous nucleation.

2.4.1 Homogeneous nucleation

Homogeneous nucleation occurs when clusters of the new phase are only in contact with the old phase. Therefore only one new interface needs to be taken into consideration. For an ideal spherical cluster of radius r , the total free energy change is:

$$\Delta G_{tot} = \Delta G_{bulk} + \Delta G_{interface} = \underbrace{\Delta\mu \cdot \frac{4}{3}\pi r^3}_{\Delta G_{bulk}} + \underbrace{\gamma_{\alpha\beta} \cdot 4\pi r^2}_{\Delta G_{interface}} \quad (2.42)$$

As the radius increases, the free energy ΔG will first rise and then decrease. The radius at which free energy is at its maximum is called critical size. Clusters larger than the critical size will grow unlimited into new bulk phase. The height of the energy barrier at $d\Delta G_{tot}/dr = 0$ is:

$$\Delta G_{hom}^* = \frac{16\pi\gamma_{\alpha\beta}^2}{3\gamma\mu^2} \quad (2.43)$$

2.4.2 Heterogeneous nucleation

If nucleation takes place in the vicinity of an additional interface, it is considered *heterogeneous nucleation*. In this case, this second interface has to be taken into account. In order to induce heterogeneous nucleation, the nucleation barrier has to be lower compared to the homogeneous case.

For a spherical cap forming at this interface, ΔG_{het} is

$$\Delta G^{het} = f(\theta)\Delta G^{hom} \quad (2.44)$$

with

$$f(\theta) = \frac{1}{4}(2 + \cos\theta)(1 - \cos\theta)^2 \quad (2.45)$$

Thus the critical nucleation barrier $\Delta G^{*,het}$ follows:

$$\Delta G^{*,het} = \frac{4\pi\gamma_{\alpha\beta}^2(2 + \cos\theta)(1 - \cos\theta)^2}{3\gamma\mu^2} \quad (2.46)$$

There is no energy barrier resulting in a continuous phase transition for a complete wetting surface ($\theta = 0^\circ$). If the contact angle is $\theta = 180^\circ$, $f(\theta)$ becomes 1, resulting in the same nucleation behavior like homogeneous nucleation. Otherwise, ΔG^* is always smaller than 1. This means that heterogeneous nucleation is always favored.

2.5 Interference-enhanced imaging of ultra-thin films

To resolve image thickness variations in ultra-thin layers, contrast-enhancement was applied [49]. Using an appropriate substrate a “ h_{off} ” is introduced, which shifts the interference pattern [50] by fourth period length to the range of maximum contrast-change.

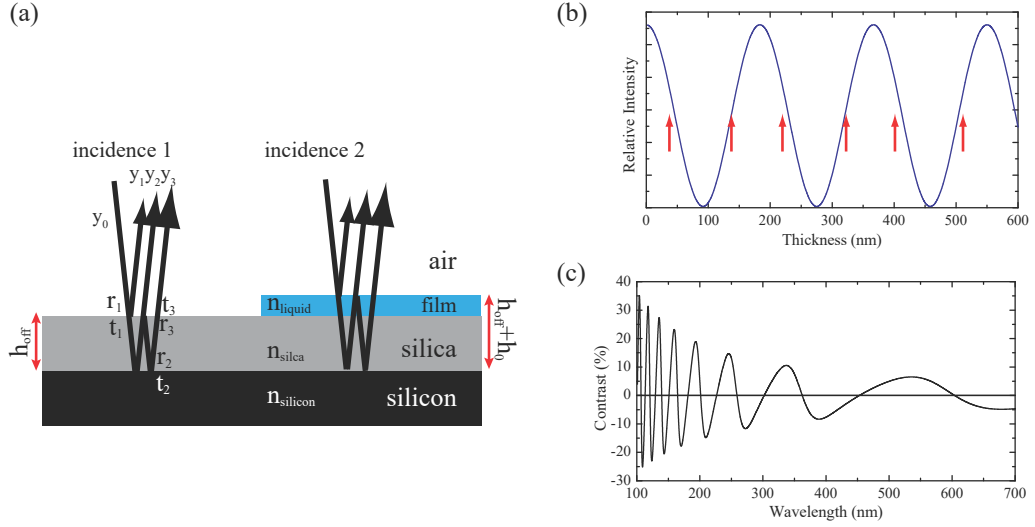


FIGURE 2.13: a) Reflection from various surfaces. b) Relative intensity depending on film thickness. c) Contrast enhancement depending on illumination wavelength.

The silicon-oxide layer has almost the same optical properties as an organic solvent film like toluene or *n*-alkene. The thickness of this oxide layer can be used to achieve an optimum “ h_{off} ”. In the system of a silicon/silica substrate and a film on top (illustrated in Figure 2.13(a)), the reflections from the various interfaces are:

$$\begin{aligned}
 \Phi_1 &= r_1 \Phi_0 e^{i\pi}, \\
 \Phi_2 &= t_1 r_2 t_3 \Phi_0 e^{i\pi}, \\
 \Phi_3 &= t_1 r_2 r_3 r_2 t_3 \Phi_0 e^{2i\pi}, \\
 &\dots
 \end{aligned}
 \tag{2.47}$$

Where Φ_i is the complex amplitude, and r_i and t_i are reflectance and transmittance, which are given by the Fresnel relations[51]:

$$\begin{aligned}
 r_1 &= (1 - t_1) = r_{\text{vapor/film}} = \left(\frac{n_1 - 1}{n_1 + 1} \right)^2 \\
 r_2 &= (1 - t_2) = r_{\text{film/solid}} = \left(\frac{n_2 - n_1}{n_2 + n_1} \right)^2 \\
 r_3 &= (1 - t_3) = r_{\text{film/vapor}} = \left(\frac{1 - n_1}{1 + n_1} \right)^2
 \end{aligned}
 \tag{2.48}$$

For a film characterized by thickness h and refractive index n , illuminated by monochromatic light of wavelength λ , the phase shift Φ for normal incidences is:

$$\phi = \frac{2\pi 2n_1 h}{\lambda} + \pi
 \tag{2.49}$$

The sum of all reflected waves is:

$$\begin{aligned}
 \Phi_r &= \sum \Phi_i \\
 &= r_1 \Phi_0 e^{-i\pi} + t_1 r_2 t_3 \Phi_0 e^{i\phi} \sum (1 + r_2 r_3 e^{i\phi} + (r_2 r_3 (e^{i\phi})^2 + \dots)) \\
 &= r_1 \Phi_0 e^{i\phi} + t_1 r_2 t_3 \Phi_0 e^{i\phi} \left(\frac{1}{1 - r_2 r_3 e^{i\phi}} \right)
 \end{aligned} \tag{2.50}$$

Hence the reflected intensity I_r is given by:

$$I_r = \left\| \frac{r_1 r_2 t_3}{e^{-i\phi} - r_2 r_3} \right\|^2 \|\Phi_0\|^2 \tag{2.51}$$

In the experiments for this thesis, the “substrate” is silica/silicon, with a refractive index for silicon of ≈ 3.88 and silica of ≈ 1.46 . The film is an organic solvent with the refractive index of ≈ 1.46 . For example with green light ($\lambda = 550\text{nm}$), the $I_r / \|\Phi_0\|^2$ as function of film thickness h is shown in Figure 2.13(b). The goal is to have the best contrast for small film thickness changes, thus to maximize $(dI_r)/dh$. The easiest way is to shift the thickness to the range around the maxima of dI_r/dh , indicated by the arrows in Figure 2.13(b). The silica layer acts as an auxiliary layer interlaced between the film under investigation and the silicon substrate. It increases the overall thickness to the range around the maxima of dI/dh . As a result the image contrast for the thin films is improved (illustrated in Figure 2.13(c)). Vertically the resolution is increased to the nano-meter scale. Thickness variations in the range of molecular thin films (4nm per layer) can easily be distinguished.

Chapter 3

Methods & Materials

3.1 Methods

3.1.1 Optical Microscopy for planar thinning films

All experiments were performed with a reflection microscopy setup (ZEISS Axio Scope.A1 Vario) and processed and analyzed by a homebuilt image analysis software. Figure 3.1(a) presents a schematic overview of the experimental setup. For the spin

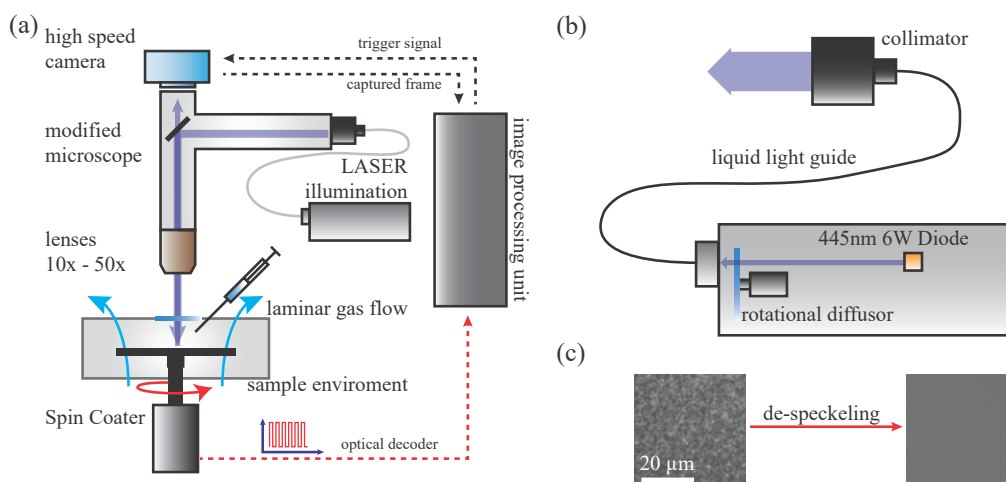


FIGURE 3.1: (a) Schematic overview of the experimental setup. (b) LASER illumination with de-speckleing apparatus. (c) Effect of de-speckleing of an image of a clean silica surface taken at $t_{exp} = 20 \mu s$ with the rotational diffusion, before (left) and after (right).

cast experiments a fast CMOS camera (EoSense®CL MC1362, Mikrotron GmbH) is used and illuminated by a LASER[7, 8]. The spin coater is mounted on a X-Y table to simplify alignment and focusing (to align the rotational- and optical axis). Samples are held in place with a vacuum created by a small membrane pump. An optical encoder provides a periodic trigger at fixed orientations for 60 images per rotation. The sample rotates in a custom build environmental chamber, which provides a laminar and homogeneous gas flow. In post processing the frames were rotated and appropriately shifted relative to each other to yield a rotation-free movie.

In Figure 3.1(b) the laser illumination is shown in detail. The illumination consists of a blue diode laser (6 W, 445 nm, LDM-445-6000, LASERTACK). In order to produce a speckle free light source the laser, a rotational diffusor running at 10000 rpm in combination with a liquid light guide. The rotational creates a fast variation of different speckle pattern over time, which can be averaged out even at very short exposure times.

Fig.3.1(c) demonstrates the effect of de-speckleing on an image of a clean silica surface. Before starting the rotation of the diffusor a typical speckle pattern is visible, with rotation, even at very short exposure times $t_{exp} = 20 \mu\text{s}$, a clean and homogeneous image is visible. Additional vibration¹ of the liquid light guide assist this effect[52, 53].

The bright illumination allows for very short exposure times ($< 80 \mu\text{s}$), to avoid motion blur. With 1000 fps, the time between two acquired frames is 1 ms. Typical thinning rates are around $\mu\text{m}/\text{s}$ which results in a height resolution of nm. In combination with high working distance lenses, typical microscopic lateral resolutions $0.27 \mu\text{m}/\text{px}$ were possible. This leads to typical fields of view (FOV) of $250 \mu\text{m} \times 250 \mu\text{m}$.

Height reconstruction by interference pattern

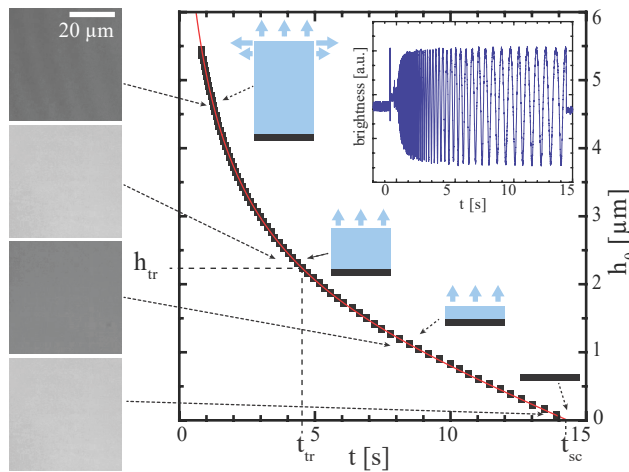


FIGURE 3.2: Time resolved imaging data and corresponding time dependent film thickness curve measured from the hydrodynamic-evaporative thinning of toluene on a rotating SiO_2 substrate ($\omega = 1000\text{rpm}$). The transition height h_{tr} characterizes the transition between the early (hydrodynamic) stage of film thinning controlled by viscous forces, and the later stage determined by liquid evaporation. Experiments for this report focus on the very late stages of film thinning with film heights, h_f , smaller than 100nm . In this case ($h_f \ll h_{tr}$) film thinning is dominated by evaporation.

With Figure 3.2 as an exemplary measurement the height reconstruction is shown. The variation of the gray level during the film thinning allows precise height reconstructions with an resolution of nm^2 . Choosing a homogeneously drying area

¹even the normal thermal vibration at room temperature

²like in reflectometry [54, 55]

in the measurement the change in intensity is analyzed. The resulting intensity (interference) curve is shown in the inset of Figure 3.2.

According to the Bragg equation³ for perpendicular incidence every peak in the curve corresponds to a certain interference maximum or minimum. The thickness change between two extrema is:

$$\Delta h = \frac{\lambda}{4 \cdot n_{\text{liquid}}} \quad (3.1)$$

To reconstruct the absolute thickness change, a reference point is needed⁴. When the film is completely dry, the absolute thickness is known (zero), and a value can be assigned to every interference mini- and maximum. Additionally, the contribution of the auxiliary silicon oxide layer has to be taken into account:

$$h_{\text{off}} = \frac{n_{\text{SiO}_2}}{n_{\text{liquid}}} d_{\text{SiO}_2} \quad (3.2)$$

With this, the absolute film thickness can be reconstructed.

$$h_i = \Delta h \cdot i - h_{\text{off}} \quad (3.3)$$

with thickness h_i at peak i . Additional data can be gained by linear extrapolation between the fringes.

Height reconstruction from the gray variation

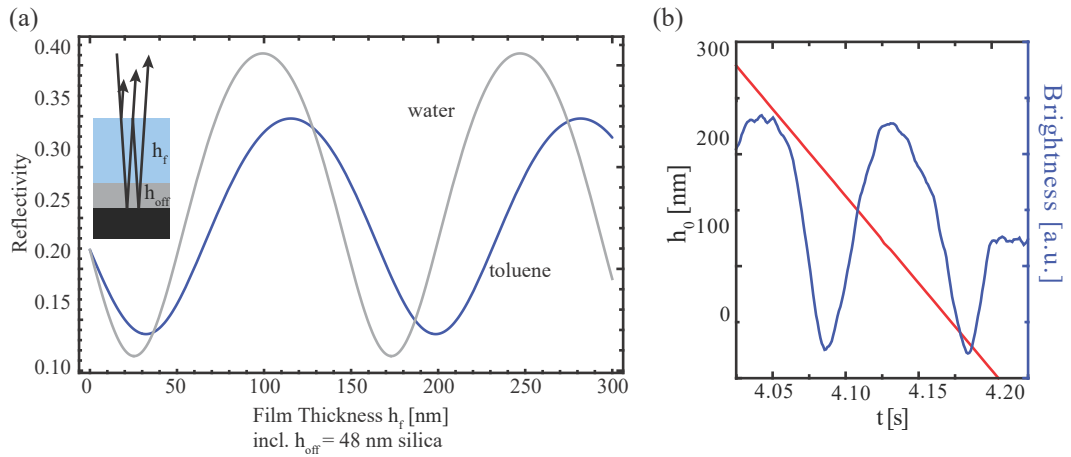


FIGURE 3.3: (a) shows the thickness depending reflective signal for water and toluene on a 48 nm silica oxide. (b) shows the brightness (blue) measured over time of a thinning toluene film. The thickness (red) is reconstructed by using the method described under chapter 3.1.1.

³Bragg relation equation $i\lambda = 2d \sin \theta$ [56]

⁴A Point of reference can be the complete drying (only substrate), the last maxi, or minimum, or the thickness of a planar and homogeneous final deposit (e.g. polymer film).

For a more precise analysis of thickness (also of static films) the gray variation between interference fringes is analyzed. This is similar to white light interferometry[57].

The reflectivity response of a thin film system can be calculated with the help of the fresnel equations. To solve these relations, calculations were done, using the Mathematica version of the program code⁵ by Steve Byrnes[59]. This method requires the knowledge about the refractive indices of the system. Figure 3.3(a) shows the reflectivity signal as function of the liquid thickness for water and toluene on 48 nm silica oxide. (Parameters for this calculation are shown in the appendix A.1.1.)

The absolute brightness measured by the camera under fixed illumination conditions can be calibrated via a homogeneous thinning liquid film (as shown in Figure 3.3(b)), assuming a linear evaporation in the last steps of drying, ergo a constant change of thickness. The gray value of each individual pixel can be translated into thickness. This can be done both by hand and by applying a polynomial fit to the thickness/reflective data⁶ to automatically translate the gray value of each pixel into thickness.

3.1.2 Setup for Dip Casting

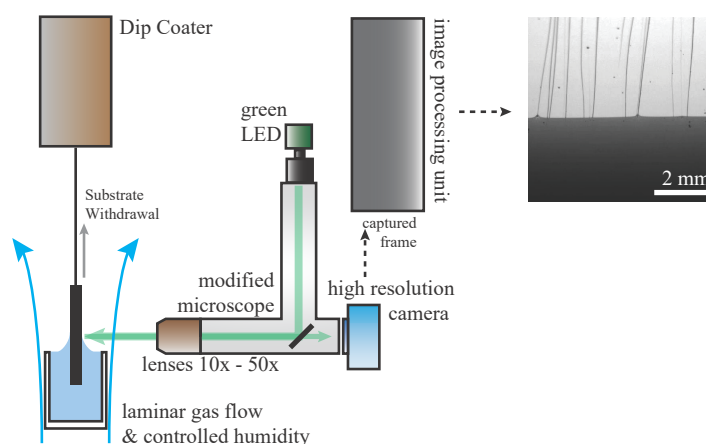


FIGURE 3.4: Schematic of the experimental setup for dip casting. A horizontal position microscope, directed at the three phase line on a substrate withdrawing from solution. The illumination was achieved by a high power LED (Luminus SST-90 green, 30 W, 527 nm), with an additional bandpass filter (527 nm, 22 nm FWHM (Edmund optics)), to sharpen the wavelength of the emitted light.

The in-situ visualization of crystal growth in a dip-cast configuration was achieved with the reflective microscope (ZEISS Axio Scope.A1 Vario). The microscope (ZEISS Axio Scope.A1 Vario) was tilted into a horizontal position (as demonstrated in Figure 3.4), to investigate the behavior of the three phase line during dip-casting. A high resolution monochromatic CMOS-camera (xiQ-series, MQ042MG-CM, Ximea GmbH) was used to record images during the substrate withdrawal from aqueous

⁵The program is available at his website[58].

⁶between the Bragg reflections i and $i + 1$ order

solution (typical speeds of 0.5 – 10 $\mu\text{m/s}$). The dip casting was done under a laminar gas flow on a vibration damping table.

3.1.3 Setup for droplet experiments

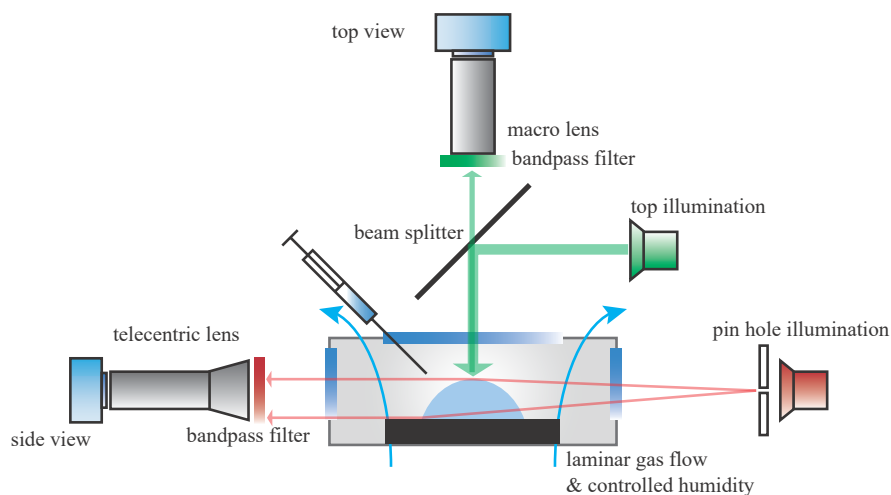


FIGURE 3.5: Schematic view of the droplet & contact angle setup. The macroscopic top view images the lateral footprint of small sessile drops. The side view depicts the contour of a droplet for contact angle measurements.

Figure 3.5 presents the experimental setup to investigate the behavior of evaporating sessile droplets (a detailed description can be found in following references [31, 60]). It consists of a macroscopic top view, which is homogeneously illuminated with a green LED, and an telecentric side view. An environmental chamber allows to control the vapor saturation of up to 3 components. This makes it possible to measure the apparent contact angle (θ_{app}) as function of various solvent vapor saturations/humidities.

Contact angle measurements

Contact angle measurements were performed in the setup described above. Sample and drop were observed simultaneously from the top and the side. The top view was used to observe the circularity of the drop footprint and overall contact line motion during the experiment⁷.

The telecentric side view images the cross section of the droplet and gives a distortion-free depiction of the droplet contour. To determine the contact angle, this contour could be extracted and fitted with a spherical cap (with a home build software). Typical drop sizes were below the capillary length, thus gravity could be neglected. The contact angle can be determined with a typical error of $\approx \pm 0.1^\circ$ [60]. To minimize evaporation effects, the duration of the experiments was kept as short as possible (typically < 20 s from placing the drops till the end of the observation).

⁷indicating pinning and wetting defects that possibly influence the measurement, or drastically composition changes during precipitation and nucleation events inside the droplet

3.1.4 Dry sample analysis

Atomic force microscopy

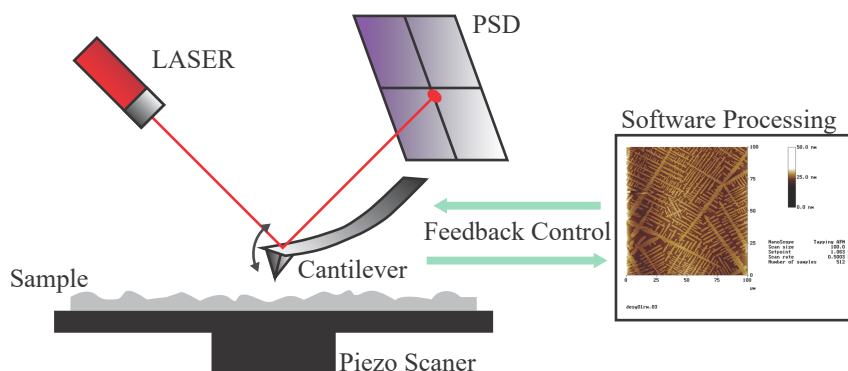


FIGURE 3.6: Schematic illustration of an atomic force microscope. The substrate topography influences the response of the cantilever which is detected by the LASER reflection on a Photodiode (PSD)

To study the topography and coverage of the samples atomic force microscopy [61] was used. This method provides a three-dimensional representation of the surface topography on a sub-nanometer length scale. To investigate the surfaces “tapping mode” is selected. Figure 3.6 shows the schematic setup of an AFM. For the measurements, the atomic force microscope “JPK Nanowizard” was used. Cantilevers with a tip radius of ~ 10 nm, with a force constant $K_F \sim 50$ N/m and a resonance frequency in the range $\sim 200 - 300$ kHz were used.

Ellipsometry

The thicknesses, h_f , of the dry polymer films (equivalent: coverages Γ) were determined by ellipsometry for thickness up to 150 nm⁸, with a Multiskope setup⁹ (HeNe-Laser @632.8 nm) in null- ellipsometry mode. The index of refraction of the uncoated silicon substrate was measured as 3.86 (silicon), the one of the silica layer as 1.46. The index of refraction for PMMA was assumed as 1.49 [62]. The index of refraction of PS was assumed 1.58 [63] and 1.56 for the block copolymer. These indices were derived from comparisons of the film thicknesses respectively coverages measured by AFM and ellipsometry in the range between 20 – 100 nm.

3.1.5 Liquid analysis

Surface tension measurements

Surface tensions for binary mixtures were measured at 20C via Wilhelmy-Method¹⁰. In order to avoid solute precipitating on the Wilhelmy-Plate (for high concentrated

⁸above 150 nm it was determined by measuring the depth of a scratch by AFM

⁹Oprel GbR, Sinzing, Germany

¹⁰K11 tensiometer, Krüss GmbH, Hamburg, Germany

solution), the measurement time was reduced. The reproducibility of the measurements was $\pm 0.5 \text{ mN/m}$.

Solubility

Solubility of FF in aqueous NH_4OH solution was measured by a weighing method. Saturated solutions were prepared by addition of excess quantities of FF into NH_4OH solution of different concentrations (from 0.01% to 28%). The samples were centrifuged after standing for 24 h and the supernatant solutions were taken for analysis. The supernatant solution was placed on microscope slides and weighed. Then, samples were heated at 100°C until dry and the residue was weighed. The solubility (S) was calculated by the following formula:

$$S = \frac{(m_2 - m_0) \cdot \rho}{(m_2 - m_1) \cdot M} \cdot 1000 \quad (3.4)$$

where m_0 is the weight of the microscope slide, and m_1 the weight of the microscope slide with supernatant solution, and m_2 the weight of the microscope slide with the FF residue, respectively. M is the molar mass of FF. ρ is the density of the aqueous NH_4OH solutions.

Evaporation rate at zero velocity

The evaporation rate at zero velocity was derived from the evaporative loss of weight per time for a petri dish ($d = 33$ mm diameter, about 5 mm deep) filled with solution in a non-convective ambient air environment. Using a high precision balance (Ohaus Adventure AX), the weight loss over time was measured. Knowing the diameter of the petri dish, and the density of the liquid the Evaporation rate could easily be calculated with following formula:

$$\frac{\Delta m}{\rho_{liquid}} \cdot \pi^{-1} d^{-2} = E^{\omega=0 \text{ rpm}} \quad (3.5)$$

3.2 Experimental procedures

3.2.1 Spin casting

For all spin cast experiments an excess volume of liquid was drop on an already rotating substrate. Typically, at a speed of 1000 rpm. The thinning was then recorded until the film became completely dry.

3.2.2 Dip casting

Aligned Growth of Single Crystals.– FF powders were dissolved in aqueous NH_4OH (FF concentration: 0.026 g/L). A 2 mL solution was added in a Teflon container, and a silicon wafer was put into the solution with the scratch near the air-liquid

interface and fixed by a clamp to the dip casting machine. The temperature was controlled by heating the container by an oil bath. After several minutes, the silicon wafer was withdrawn out of the solution by the pulling device with a constant speed, whereupon white assemblages formed on the silicon wafer. The aligned crystals formed on the silicon wafer. *Formation of "Gradient-Aligned Single Crystals" on a Silicon Wafer.*— In the experiment, the withdrawal speed of the silicon wafer was set at 2.0 $\mu\text{m/s}$ at first for several minutes. Then the speed was raised to 4.6 $\mu\text{m/s}$, resulting in the formation of fewer but longer fibers. The speed was then reduced to 2.0 $\mu\text{m/s}$ for the growth of larger numbers of fibers. Finally, when the speed was increased to 4.6 $\mu\text{m/s}$, fewer linear fibers were obtained on the silicon wafer.

3.2.3 Crystallization in a capillary

Growth of FF Single Crystals in a Capillary.— FF powders (3 mg) were dissolved in a HFP/water (110 μl /40 μl) solution. This solution was inserted into a capillary by capillary pressure. One end of the capillary was sealed by nail polish, and the other end was kept open. The capillary was placed under atmospheric pressure or lower pressure for growth of the long FF fiber. The aligned crystals formed inside the capillary. *Disassembly of FF Single Crystals in a Capillary.*— A HFP/water (5 : 1, v/v) solution was injected into a capillary with an ultralong FF single crystal formed in the oriented growth process. Then two ends of the capillary were sealed by nail polish. The capillary was held at room temperature, and the disassembly of the long FF fiber was observed by optical microscopy (described above).

3.3 Materials

3.3.1 Solvents and Solutions

For the preparation of solutions of hexatriacontane n-alkane ($\text{C}_{36}\text{H}_{74}$ high purity 99.99%, Sigma-Aldrich) and triacontane n-alkane ($\text{C}_{30}\text{H}_{62}$ high purity 99.99%, Sigma-Aldrich), high purity toluene (C_7H_8 Chromasolv Plus for HPLC, 99.9+%), methylcyclohexane (MCH C_7H_{14} high purity 99.5%, Sigma-Aldrich) and n-nonane (C_9H_{20} high purity 99.8%, Sigma-Aldrich) were used. NaHCO_3 (99.7+%) was diluted in MilliQ.

3.3.2 Substrates

As substrates, different types of polished silicon wafers were used: substrates with a natural oxide layer (Si(100), p, $d = 30$ cm) double sided polished silicon wafers¹¹ with an artificial oxide layer of 1000 Å grown by wet oxidation (Si(100), p, $d = 30$ cm). single sided polished silicon wafers¹² were used with an artificial oxide layer of 500 Å, grown by wet oxidation (Si(100), p, $d = 20$ cm). The wafers were broken into

¹¹Lam Research AG, Villach, Austria

¹²Siegert Wafer, Aachen, Germany

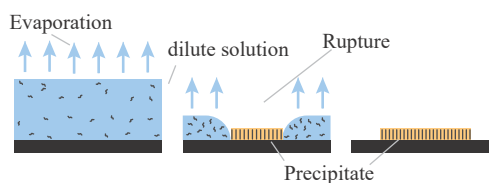
pices of roughly 1×1 cm. Great care was taken to prevent dust contamination of the samples.

Cleaning and Preparation

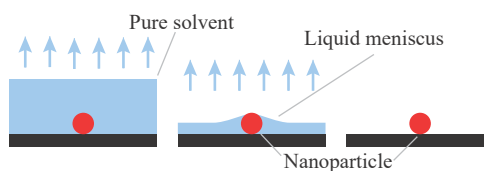
After cutting, the substrates were sonicated in a low power supersonic bath 4 – 5 min sequentially in MilliQ , ethanol , acetone, ethanol, and MilliQ. Then the samples were cleaned with piranha (3:1 – $\text{H}_2\text{SO}_4/\text{H}_2\text{O}_2$) for approximately 30 min at 70 °C to remove organic contaminations. After flushing with copious amounts of water, the samples were sonicated again in MilliQ water for about 10 min to remove traces of the acid. After cleaning they were stored under MilliQ in a closed beaker for a maximum of 6h. Directly before use they were rinsed again with fresh MilliQ and dry-blown with clean nitrogen (purity 5.0).

Part II

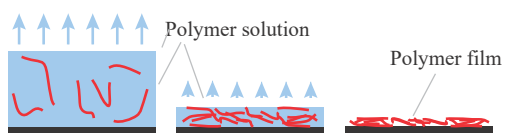
Evaporating thin films on planar solid substrates



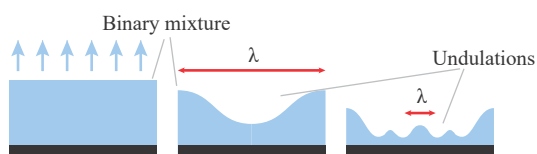
Rupture of ultrathin solution films on planar solid substrates induced by solute crystallization



Meniscus shape around nanoparticles embedded in molecularly thin liquid films



Deposition of polymer films by spin casting: A quantitative analysis



Thin Films with Lateral Gradients

Chapter 4

Rupture of ultrathin solution films on planar solid substrates induced by solute crystallization

The Chapter is reprinted and adapted from: [8] Stephan Eickelmann and Hans Riegler. "Rupture of ultrathin solution films on planar solid substrates induced by solute crystallization". In: *Journal of Colloid and Interface Science* 528 (2018), pp. 63–69.

S. Eickelmann designed the study in consultation with *H. Riegler*. *S. Eickelmann* planned and build the experimental setup used for the on-line imaging of planar thinning films (Chapter 3.1.1), conducted, analyzed and evaluated all the experimental data, drafted the first few versions of the manuscript, and designed the figures. *J. Danglad-Flores* helped to measure the two AFM measurements shown in Fig. 4.2&4.3. The manuscript was then revised by *H. Riegler*.

4.1 Abstract

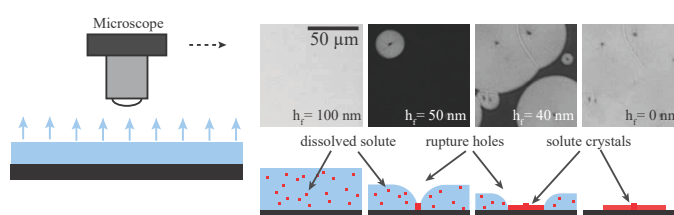


FIGURE 4.1

A liquid deposited on a solid surface may wet the surface completely or only partially. As a result it may form a planar closed film or rupture and form a film with holes, or even rearrange into individual droplets. The wetting and rupture behavior of thin films on planar solid substrates is a permanent research topic [29, 64–67] not the least because it is of eminent practical relevance [68–73]. For liquid films thinner than millimeters gravitational forces can be neglected. Their wetting behavior is determined by the interactions between the substrate and the film [74–77]. With smooth substrate surfaces the interactions depend on the composition and state of

the film (e.g. its temperature). It depends also on the film thickness and of the bulk properties of the substrate (e.g. with VdW interactions the disjoining pressure and its sign).

4.2 Introduction

For liquid films thinner than millimeters gravitational forces can be neglected. Their wetting behavior is determined by the interactions between the substrate and the film [74–77]. With smooth substrate surfaces the interactions depend on the composition and state of the film (e.g. its temperature). It depends also on the film thickness and of the bulk properties of the substrate (e.g. with VdW interactions the disjoining pressure and its sign).

Typical wetting studies address the relation between all these parameters and the wetting and film rupture behavior. There have been experimental studies on the rupture of liquid films [10–14], as well as thin polymer or thin metal films [15–20]. The film rupture has also been investigated theoretically [21–24]. In most cases investigated up to now the composition of the liquid film was kept fixed.

However, in most naturally occurring and industrially applied cases, in particular with volatile liquid components, the composition of the liquid changes with time and film thickness [78]. Aside from the film thickness this constitutional change can have a very strong impact on the interactions determining the wetting and rupture behavior. The change in film composition, for instance, may switch its behaviour from inherently wetting to non-wetting and thus lead to film rupture.

For experimental investigations addressing the impact of the (changing) film composition on the rupture behaviour the composition has to be (continuously) controlled and known while the wetting and rupture behavior is monitored. In the following we will present studies on the wetting/rupture behavior of continuously thinning liquid planar films consisting of binary solvent/solute mixtures deposited on smooth planar substrates. The wetting/rupture properties are investigated by continuously imaging a small area of the liquid film with reflection optical microscopy, while the film is continuously thinning due to the evaporation of the volatile liquid component. At the same time the nonvolatile solute gets continuously enriched in the thinning film. Practically the experiments are performed in a spin cast configuration, where the thinning of the film and the evolution of its composition is well known [25, 34]. The investigations show that the film composition affects the wetting and rupture behavior. The local crystallization of the solute at the interface leads the formation of holes at these locations if the film is thin enough so that film rupture is energetically favorable.

4.3 Film rupture heights for mixtures of toluene/ $C_{36}H_{74}$

In Figure 4.2, the rupture (hole formation) behavior of planar thinning film of a solution of $C_{36}H_{74}$ in toluene is shown. The optical image sequence illustrates that shortly after the liquid deposition on the rotating substrate, a homogeneously planar

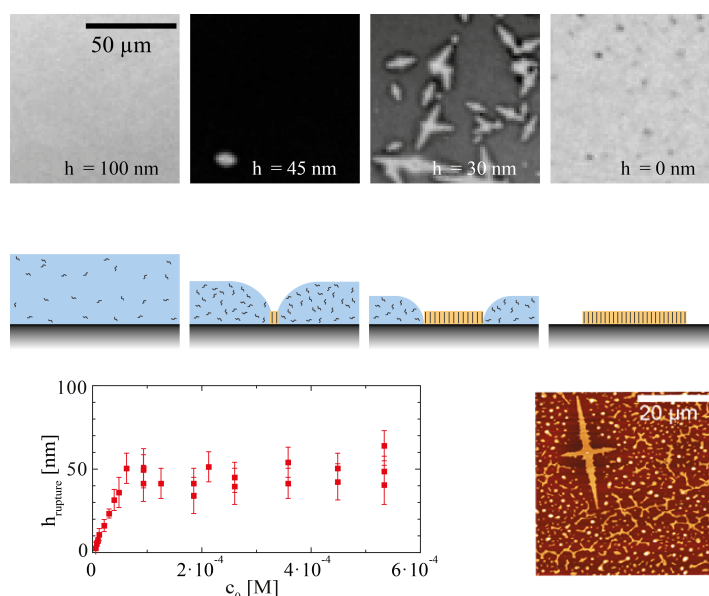


FIGURE 4.2: Rupture behavior of films of mixtures of toluene/ $C_{36}H_{74}$. The top rows show examples of images recorded as the films become thinner due to solvent evaporation ($c_0 = 2.6 \cdot 10^{-4}M$). The cartoons depict the corresponding cross sections through the films indicating the crystallization of the solute at the substrate/film interface and the hole formation at this location. The plots shows the film heights, $h_{rupture}$, at which hole formation is observed/commences as function of the weighing in concentration of the solute, c_0 . Also shown are AFM images of the dry solute on the substrates after complete solvent evaporation.

film is formed (for all weighing in solute concentrations, c_0 , all solutions first form a closed). During the evaporating thinning, all liquid films remain closed and planar, as long as they are thicker than about 50 nm. Pure solvent films remain whole during the entire film thinning until all liquid has completely dried.

The plot in Figure 4.2 shows the rupture thickness $h_{rupture}$ as function of the in weight concentration c_0 . With thinner than $h_f = 50$ nm films, the wetting behavior (planarity of the film) depended on the solute concentration. Films of solutions form holes and rupture as soon as they become thinner than a specific film thickness, $h_{rupture}$. This $h_{rupture}$ depends on the solution composition, in particular on the solute concentration. If the weighing in solute concentration, c_0 , is very low, $h_{rupture}$ is rather small. $h_{rupture}$ increases linearly with c_0 until it reaches a maximum rupture thickness of $h_{rupture} \approx 50$ nm. Upon increasing c_0 further, $h_{rupture}$ remains constant at ≈ 50 nm.

The optical investigations during and after the film thinning as well as AFM (one explanatory measurement shown in Figure 4.2) studies on the dry samples show that the hole formation starts at spots, where the solute crystallizes at the interface between substrate and liquid film. $C_{36}H_{74}$ forms the typical dendritic 2-dimensional mono- or multilayer aggregates that are described already in the literature elsewhere.

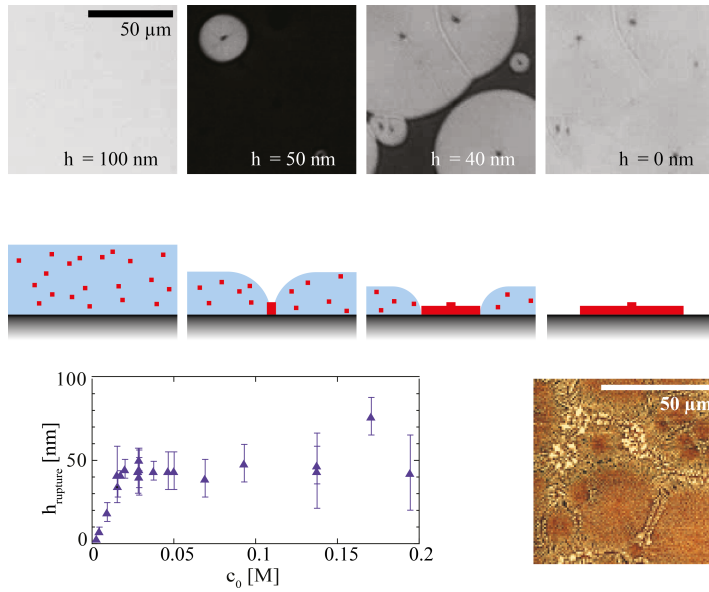


FIGURE 4.3: Rupture behavior of films of $\text{H}_2\text{O}/\text{NaHCO}_3$. The top rows show examples of images recorded as the films become thinner due to solvent evaporation ($c_0 = 1.4\text{M}$). The cartoons depict the corresponding cross sections through the films indicating the crystallization of the solute at the substrate/film interface and the hole formation at this location. The plots shows the film heights, h_{rupture} , at which hole formation is observed/commences as function of the weighing in concentration of the solute, c_0 . Also shown are AFM images of the dry solute on the substrates after complete solvent evaporation.

4.4 Film rupture heights for mixtures of $\text{H}_2\text{O}/\text{NaHCO}_3$

Figure 4.3 presents the hole formation (rupture) behavior of planar films of solutions of NaHCO_3 in water. The optical imaging shows that after liquid deposition on the rotating substrate, in both cases and for all weighing in solute concentrations, c_0 , all solutions first form a closed, homogeneously planar film. During evaporative thinning all liquid films remain closed as long as they are thicker than about 50 nm. With thinner films the wetting behavior depends on the solute concentration. Pure solvent films remain closed during the entire film thinning until all the liquid has evaporated. Films of solutions form holes and rupture as soon as they become thinner than a specific film thickness, h_{rupture} . This h_{rupture} depends on the solution composition, in particular on the solute concentration. If the weighing in solute concentration, c_0 , is very low, h_{rupture} is rather small. h_{rupture} increases linearly with c_0 until it reaches a maximum rupture thickness of $h_{\text{rupture}} \approx 50\text{nm}$. Upon increasing c_0 further, h_{rupture} remains constant at $\approx 50\text{nm}$.

The optical investigations during and after the film thinning as well as AFM studies on the dry samples show that the hole formation starts at spots, where the solute crystallizes at the interface between substrate and liquid film. NaHCO_3 forms¹ small crystals with the typical monoclinic structure [81].

¹The crystallization of anorganic salts from evaporating aqueous solutions is described elsewhere [79, 80].

4.5 Film rupture thicknesses for various different binary mixtures

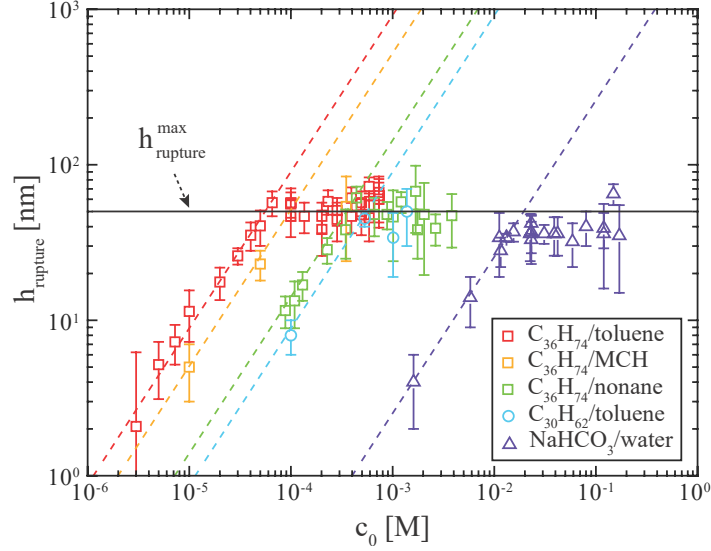


FIGURE 4.4: Film rupture (hole formation) thicknesses, $h_{rupture}$, as function of the weighing in solute concentrations, c_0 , for various solutions: $C_{36}H_{74}$ /toluene ($c_{sat} = 1.8 \cdot 10^{-3}M$, $h_{tr} \approx 5\mu m$), $C_{36}H_{74}$ /MCH ($c_{sat} = 1.4 \cdot 10^{-2}M$, $h_{tr} \approx 7\mu m$), $C_{36}H_{74}$ /nonane ($c_{sat} = 2.5 \cdot 10^{-2}M$, $h_{tr} \approx 3\mu m$), $C_{30}H_{62}$ /toluene ($c_{sat} = 5.5 \cdot 10^{-2}M$, $h_{tr} \approx 5\mu m$), $NaHCO_3$ /water ($c_{sat} = 1.1M$, $h_{tr} \approx 3\mu m$). The dashed lines show h_{sat} , the film thicknesses, where the solute concentration reaches its saturation.

Figure 4.4 presents the hole formation behavior i.e., the film rupture thicknesses, $h_{rupture}$, of five different solutions as a function of the solute concentration. All pure solvents wet the substrate completely. As already presented for two solutions in Figure 4.2 & 4.3, in all cases $h_{rupture}$ increases linearly with the solute concentration, c_0 . As soon as $h_{rupture}$ reaches $h_{rupture}^{max} \approx 50$ nm, it remains constant, even as c_0 is increased further. The solubilities of the solutes in the different solvents vary considerably. Accordingly, the transition from the increasing $h_{rupture}$ to the plateau with $h_{rupture}^{max} \approx 50$ nm is orders of magnitude different for different solutions. Figure 4.5 shows the same data in a plot of $h_{rupture}$ vs. h_{sat} . The dashed line shows $h_{rupture} = h_{sat}$. With this rescaling all data collapse into one universal behaviour. $h_{rupture}$ increases linearly with h_{sat} up to a maximum value of $h_{rupture}^{max}$ and then remains at this value, even if h_{sat} increases further. Optical imaging reveals that the holes in the film always develop where solute crystals start to grow at the substrate/liquid interface for the case when $h_{sat} < h_{rupture}^{max}$. For $h_{sat} < h_{rupture}^{max}$ solute crystals probably grow already as soon as $c > c_{sat}$ for films thicker than $h_{rupture}^{max}$. In this case hole formation commences as soon as $h_{sat} \leq h_{rupture}^{max}$ at locations with solute crystals at the interface between film and substrate. These scenarios are depicted in the cartoons of Figure 4.5.

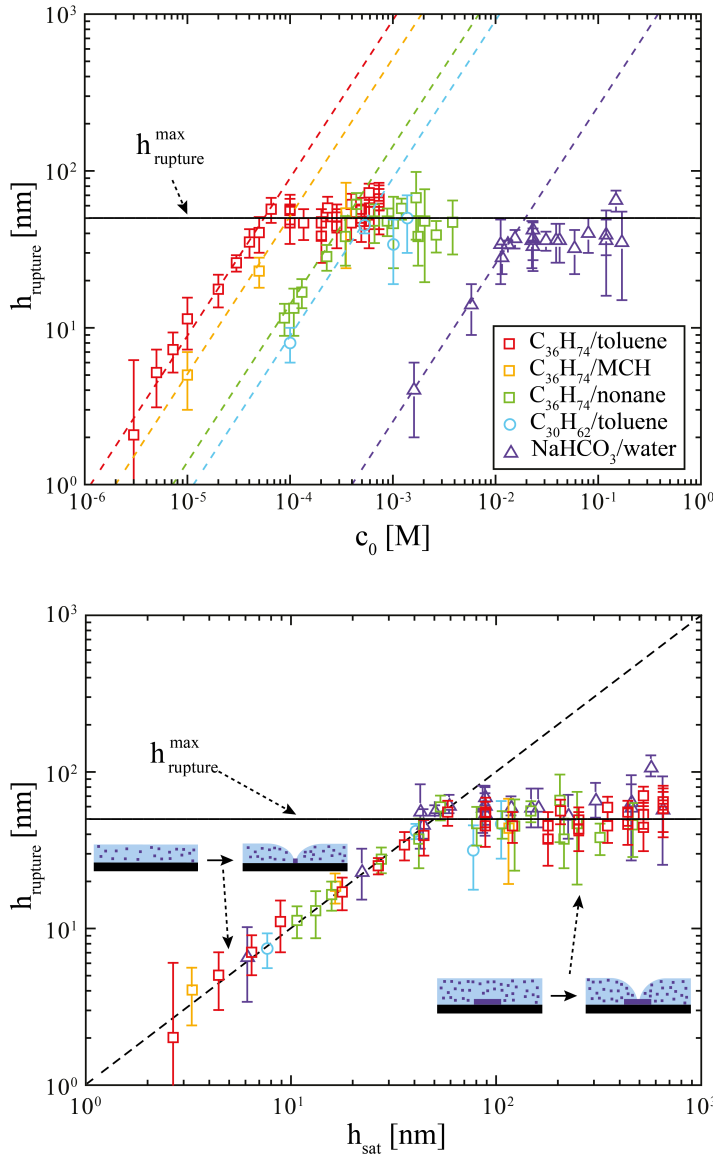


FIGURE 4.5: Plot of h_{rupture} as function of h_{sat} . The dashed line shows $h_{\text{rupture}} = h_{\text{sat}}$. The cartoons show how for $h_{\text{sat}} < h_{\text{rupture}}^{\text{max}}$ solute crystallization and hole formation occurs approximately simultaneously, whereas for $h_{\text{sat}} > h_{\text{rupture}}^{\text{max}}$ solute precipitation occurs before film rupture.

4.6 Discussion

Figure 4.4 shows that for small solute weighing in concentrations, c_0 , the rupture film thicknesses, h_{rupture} , increase proportional to c_0 . As soon as $h_{\text{rupture}} \approx 50$ nm, it remains constant at this value $h_{\text{rupture}}^{\text{max}}$ (independent of c_0). The linear increase of h_{rupture} with c_0 and the limit with $h_{\text{rupture}}^{\text{max}} \approx 50$ nm is observed for all the various combinations of solutes and solvents investigated although the transition between the linear increase and the plateau behavior occurs with c_0 , which are different by orders of magnitude.

The key to understanding this behavior is the solute enrichment during the evaporative film thinning in a spin cast configuration, which has recently been analyzed quantitatively [25, 34]. Figure 2.11 (in Chapter 2.3.4) shows qualitatively the increase of the solute concentration as the film becomes thinner due to the solvent evaporation. With the setup shown and described in Chapter 3.1.1 (figure 3.1) the evaporation rates, E , of the various solutions can be measured (Equation 2.39). Thus, the increase of the solute concentration can be determined (Equation 2.40) and h_{sat} can be calculated. The measurements show that the transition between the range with a linear increase of $h_{rupture} \propto c_0$ and the plateau behaviour with $h_{rupture} = const = h_{rupture}^{max}$ occurs in all cases when the solute concentration within the film reaches its saturation value, c_{sat} , at film thickness of $h_f \approx 50$ nm. Taking this into account the rupturing behaviors of all the different solutions can be rescaled and plotted universally as depicted in Figure 4.4.

The time-resolved optical imaging of the films during the film thinning and rupturing reveals the possible reason for the hole formation. It appears as if film rupturing always occurs at locations, where the solute is forming (or has already formed) crystals at the interface between substrate and liquid film. This indicates the following film rupture scenario: As soon as the solute becomes sufficiently supersaturated (i.e., $c = c_{sat} + \delta c$, where δc accounts for the extra concentration to overcome the nucleation barrier) it starts to crystallize. Basically, nucleation and crystal growth might occur at three different locations: 1.) at the substrate surface, 2.) within the solution, or 3.) at the film surface. During nucleation and early crystal growth the crystals are very small and they are not directly visible with optical microscopy. As soon as they grow to micron size they may become optically visible and their location at this stage indicates where their nucleation and early growth may have occurred.

Alkanes form quasi-2-D mono- or multilayer domains, which indeed can be imaged by optical microscopy [82, 83]. For the alkane solutions investigated for this report, with initial alkane concentrations substantially lower than the saturation concentration ($c_0 < 0.1c_{sat}$), we do *not* observe any alkane domains *before* the film ruptures (neither within the solution nor at the substrate/film or the film/air interface). On the other hand, we find that the film always ruptures and forms a hole at a spot, where an alkane domain is attached to the substrate. These domains can be seen either already during the widening of the hole or later on the dry substrate. This is the scenario depicted in Fig. 4.2. It is corroborated by experiments with films of very high initial alkane concentrations ($c_0 > 0.1c_{sat}$), which are not the subject matter of this chapter, because their thinning behavior is fundamentally different to the case described in this report/chapter (shown in a later part of this thesis under *Outlook 10.1.1*).

As in the case of the alkane solutions, with solutions of $\text{NaHCO}_3/\text{water}$ we also never see crystals before film rupture. And, as in the case of the alkanes, the film always ruptures and forms a hole at a spot, where we always find (later) optically (or by AFM) a crystal of NaHCO_3 (see for example Fig. 4.3). This crystal is usually larger than the other crystals in its vicinity (which result from the receding three phase contact line). With NaHCO_3 also the three nucleation and growth scenarios at the three different locations are conceivable, as discussed above for the alkanes. However, with NaHCO_3 these cases cannot be distinguished by optical microscopy

in a way as described for the alkanes, because NaHCO_3 forms 3-D crystals. Therefore, as soon as the crystals are large enough to be optically observable, they already are larger (higher) than the thickness of the film in which they grow.

It should be mentioned that the results of a few selective experiments with aqueous solutions of NaCl agree with the findings obtained with NaHCO_3 and with the alkanes. By and large, the observation with the alkane domains agrees with the expectation that the crystallization preferentially commences at the film/substrate interface, because heterogeneous nucleation at this interface is more favorable than homogeneous nucleation within the film or heterogeneous nucleation at the film/air interface [84].

The observations indicate that, if the film is sufficiently thin (a few tens of nm), film rupture is initiated at a spot, where the interface between film and substrate is locally modified by a crystal. The local growth of a crystal effectively changes a) the local wetting properties and b) it reduces locally the film thickness. In the case of long chain alkanes, the local crystal is a flat mono- or multilayer domain, typically only a few nm thick. Therefore, the local film is not much thinner (on the scale of $h_{rupture}^{max}$) than the film on the substrate without the alkane domain and the locally different wetting properties might be more important than the locally thinner film. It is known that surfaces of solid long chain alkanes are not wetted by liquid short chain alkanes, such as *nonane* ([82, 85–87]). It can be assumed that they are also not wetted completely by other hydrophobic liquids, such as *toluene* or *methylcyclohexane*. Very little is known about the wettability of anorganic crystals (NaHCO_3) by anorganic solute/solvent mixtures ($\text{NaHCO}_3/\text{water}$), with the solute and the crystals being identical substances. The observed rapidly retreating contact line of the $\text{NaHCO}_3/\text{water}$ solutions as soon as the film is thinner than $h_{rupture}^{max}$ and has ruptured indicates that the $\text{NaHCO}_3/\text{water}$ solutions do not wet completely substrate surfaces that are (partially) covered by NaHCO_3 crystals. In any case, with a globally continuously thinning film, the local non-wetting properties in combination with the locally thinner film eventually will lead to film rupture either by a spinodal [14, 88] or a nucleated process [18, 30].

The wetting behavior of films is affected by VdW interactions and in the non-wetting case film rupture driven by VdW-interactions typically occurs for film thicknesses of a few tens of nanometers. This is what we observe ($h_{rupture}^{max}$). This is also in agreement with the cases of low solute concentrations, when the films rupture instantaneously as soon as the substrate (locally) switches from wetting to non-wetting due to the local growth of a crystal at the interface between film and substrate ($h_f < h_{rupture}^{max}$ for low c_0).

Based on the assumption that VdW-interactions drive the film rupture we performed experiments with different Hamaker constants. We used substrates with oxide layers of different thicknesses (natural oxide layers of only ≈ 1.5 nm thickness, artificial oxide layers 50 nm and 100 nm thick). These variations are part of the data presented in Figures 4.2, 4.3, 4.4, and 4.5. They are not indicated individually, because there is no systematic correlation between the variations and the observed behaviour. Aside from modifications of the substrate surface, the VdW-interactions of systems with water as solvent should be different to those with toluene (the refractive indices and thus the Hamaker constants of both systems are significantly different). Figure 4.5 shows that within the errors the results are not sensitive to these variations.

The results with different substrates and solvents do neither support nor exclude VdW-interactions as main cause for the film rupture, because the errors for $h_{rupture}^{max}$ are quite large. Even if differences in the VdW-interactions had an impact on $h_{rupture}^{max}$, this hardly could be derived from the data.

4.7 Summary

A setup has been designed and implemented to optically image time-resolved the thinning and rupture behavior of thin planar films of binary mixtures of a volatile solvent and a non-volatile solute on planar substrates in a spin cast configuration. The solutes form crystals as soon as the concentration exceeds a known saturation value. The focus is on the wetting/rupturing behavior of very thin films. The thinning behavior and time-dependent variation of the film composition in the applied spin cast configuration has been studied and is well-known. At the very late stages of the spin cast process, hydrodynamic flow can be neglected. The system is essentially a planar liquid film, which is thinning due to a constant evaporation rate. It is observed that depending on the type of solvent/solute mixture and solute concentration the films rupture at certain film thicknesses. This behavior is analyzed and discussed in some detail.

4.8 Conclusion

In conclusion, the experimental results and their analysis reveal three significant, important, and hitherto unknown findings: 1.) the films rupture if a.) the solute concentration reaches its saturation value and if b.) the film is as thick or thinner than a certain film thickness, $h_{rupture}^{max}$, 2.) The rupture behavior is remarkably universal in view of the really very large variation of initial solute concentrations and different combinations of solute/solvent, 3.) In all cases $h_{rupture}^{max}$ has a value somewhere between more than 10 nm and less than 100 nm. Supposedly the crystallization of the solute at the film/substrate interface alters locally the wetting properties. This leads to the film rupture at this location. The value of $h_{rupture}^{max}$ is an indication and consistent with VdW-interactions as main reason for the film rupture. It can be assumed that such a film rupture behavior occurs very often. For instance, most natural aqueous solutions contain non-volatile, precipitating/crystallizing components such as salts. Regarding application, the findings can also be used to tailor-make solutions to trigger the rupture of evaporating films at specified thicknesses with specific hole formation scenarios (e.g. by adjusting how the solute crystallization/precipitation occurs).

Chapter 5

Meniscus shape around nanoparticles embedded in molecularly thin liquid films

The chapter is based on a manuscript currently under evaluation at Science Advances: [89] Stephan Eickelmann, José Danglad-Flores, Gouxiang Chen, Markus S. Miettinen, and Hans Riegler. “Meniscus shape around nanoparticles embedded in molecularly thin liquid films”. 2018.

S. Eickelmann build the microscopy setup used for the experiments, conducted the optical imaging on evaporative thinning- and dry solid- films, evaluated the optical data, and developed a protocol to translated them into topological data (see Chapter 3.1.1, leading to Figure 5.2, 5.3, 5.4, 5.5, and 5.8), wrote the first few versions of the manuscript and designed the Figure s. *J. Danglad-Flores* performed the AFM measurements and did the analysis/fitting of the meniscus data obtained by AFM and optical microscopy (presented in Figure 5.5, 5.6, and 5.7), and wrote the supplement material. *G. Chen* also performed some of the optical microscopy experiments (for Figure 5.3) and synthesized and characterized the nanoparticles. *M. Miettinen* help with the theoretical understanding of the meniscus shape which was wrote down by *J. Danglad-Flores* (presented in the Appendix A.2). The study was designed in close collaboration of *S. Eickelmann*, *J. Danglad-Flores*, and *G. Chen* and supervised by *H. Riegler*. The manuscript was revised by *H. Riegler*. All authors discussed the results and commented on the manuscript.

5.1 Abstract

Individual nanoparticles embedded in molecularly thin films at planar substrates and the resulting film surface distortion (meniscus) adjacent to the nanoparticles are investigated by conventional optical reflection microscopy. Even for nanoparticles much smaller than the Rayleigh diffraction limit the meniscus creates such a pronounced optical footprint that the location of the nanoparticles can be identified. This is because the decay length (lateral extension) of the meniscus exceeds the size of the nanoparticle by orders of magnitude. Therefore, for the first time, the exact shape of the meniscus of the liquid adjacent to a nano-size object could be measured and analyzed. The meniscus has a zero curvature shape (cosine hyperbolic). The

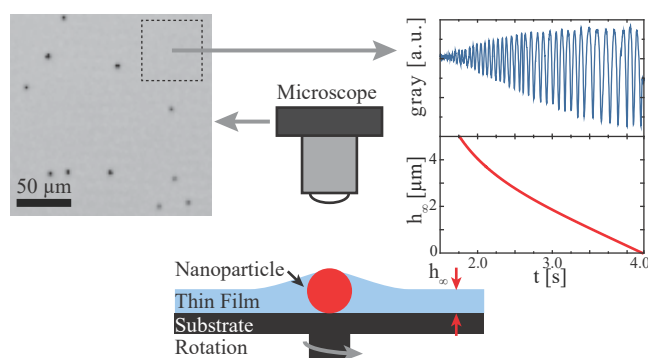


FIGURE 5.1

liquid in the meniscus is in pressure equilibrium with the far-field planar film. The decay length decreases with decreasing nanoparticle size. But it is independent from the far-field film thickness. Supposedly the decay length is determined by Van der Waals interactions (VdW) although it is unknown what determines its (unexpectedly large) absolute value. The presented technical approach may be used to investigate biological systems (for instance surface distortions in supported membranes caused by proteins or protein aggregates).

5.2 Introduction

Small objects embedded in thin films are ubiquitous in nature [90–95]. They are a topic in basic research [96–101] and proposed as well as used for applications [102–106]. If the particles are larger than the film thickness, they "stick out". Therefore they will distort the adjacent film surface (cause a "meniscus"). The geometry of this meniscus is of interest in applied and fundamental science, because it reflects the interactions between the particle and its environment and is a measure/cause for the interaction between neighboring particles. Therefore the meniscus geometry is an important system parameter.

For micrometer-sized and larger systems meniscus shapes have been investigated experimentally and theoretically [107–110]. For smaller i.e., truly nanometer-size systems, with particle diameters and really thin films (thicknesses $\ll 1 \mu\text{m}$), meniscus geometries have been studied experimentally up to now only for solid systems. For instance, systems with particles embedded in polymeric films were imaged by atomic force microscope (AFM)[111–114], scanning electron microscopy (SEM)[111, 115] or with confocal optical methods[116–122]. In these cases the meniscus geometries were affected by the solidification process. They may not reflect the equilibrium situation of the particles embedded in the mobile/liquid film. This case, meniscus shapes in the vicinity of nano-size particles embedded in very thin liquid (mobile) films, has not been investigated up to now. The shape of the meniscus of a liquid film adjacent to a nanoparticle (NP) is still unknown. It is still unknown how it depends on particle size, on film thickness, on film properties (surface tension), on substrate properties, etc.

If the size of NPs is well below the resolution limit for visible light (Rayleigh limit [123]), their *imaging* is impossible with conventional optical microscopy. It has been shown however, that it is possible to identify the *location* of nano size objects with conventional optical microscopy through their refraction/diffraction signature e.g., by the "caustics" caused by surface distortions [124]. The optical diffraction signature is usually weak but it can be enhanced by sophisticated image processing (oversampling, background subtraction, contrast enhancement, etc. [125]). Slight defocussing along the optical axis[126–129] may also enhance the diffraction signal in particular with particles embedded in thin films[124, 130].

In the following we present a new approach to determine the location of NPs embedded in a molecularly thin liquid film and to *quantitatively* measure the adjacent meniscus shape. We use a special setup of interference enhanced optical reflection microscopy. We determine the location of even very small NPs (diameters $\ll 100$ nm) embedded in liquid films. We measure the meniscus shape as well as the far-field liquid film thickness with *nm* precision. We find that in comparison to the vertical scale the lateral scale of distortion reaches out further by orders of magnitude more.

5.3 Optical footprints of NPs and their menisci in liquid films of various thicknesses

Figure 5.2(a) presents a sequence of interference microscopy snapshots, which were recorded during the evaporative thinning (see Methods section) of a toluene film on a planar silicon wafer substrate. Figure 5.2(b) shows the time-dependent variation of the "Brightness" (gray level) as it is measured from a surface area with a planar film of uniform thickness (i.e., an area without NP). This signal is translated into a momentary "far-field" toluene film thickness, h_∞ i.e., a film thickness undisturbed by NPs (see Methods section).

The samples were prepared by first depositing a mixture of Platinum-Nanoparticles (NPs) with diameters d_{NP} of $\approx 25, 50, 100$ and 200 nm onto a planar silicon wafer sample via spin casting from an aqueous solution. The process conditions and NP-concentrations were adjusted[8, 25, 34] such that the average distance between individual NPs was in the range of several tens of μm . The data presented in Figure 5.2 were obtained during the evaporative thinning of a film of pure toluene i.e., during the spin casting of pure toluene onto the substrates with the NPs already deposited.

The snapshots of Figure 5.2(a) reveal that at certain locations spots of locally different gray levels appear as soon as the film thickness has decreased to a certain value. The gray levels of the spots change as the film gets thinner. The spots remain and disappear only when the toluene has evaporated completely¹. AFM and optical investigations on the lateral arrangements and the surface coverage of the NPs on the dry samples prove that individual NPs are the origin of the spots i.e., the

¹Spots from the largest NPs with diameters of 200nm are still faintly visible even with completely dry substrates

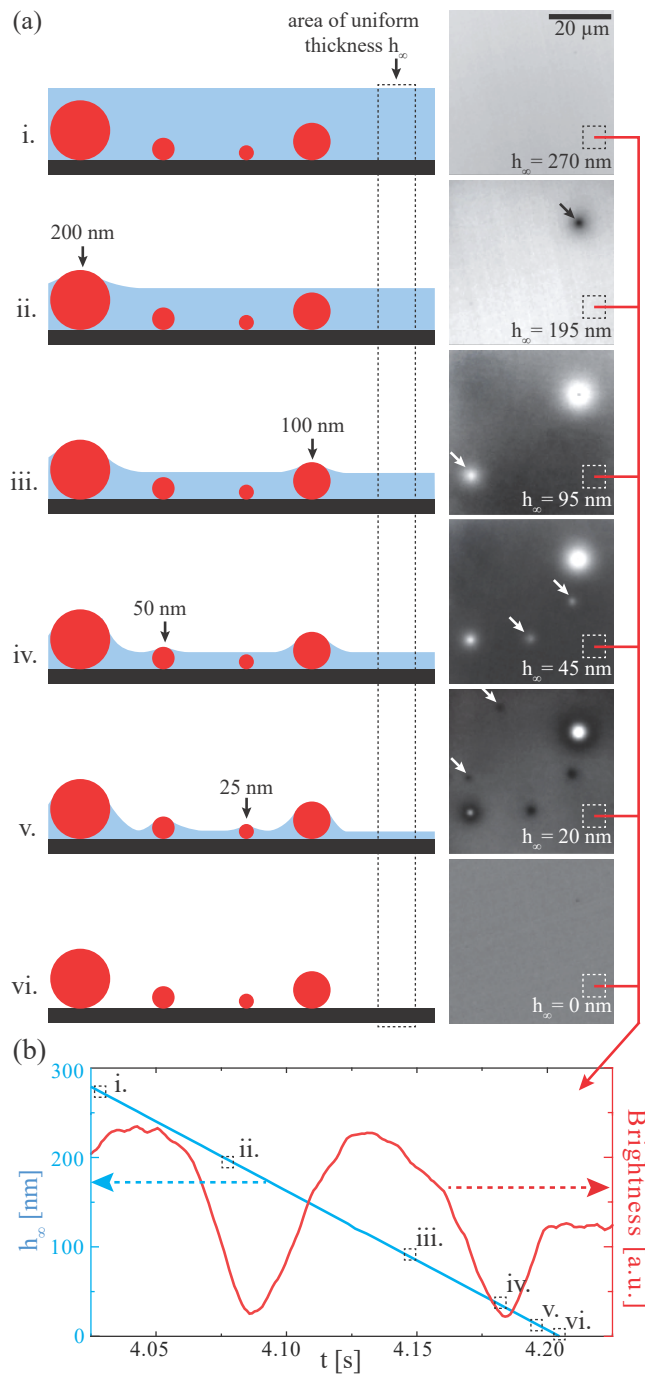


FIGURE 5.2: Snapshots of optical footprints of NPs embedded in a thinning toluene film. Attached to the substrate surface are individual NPs with diameters of $d_{NP} \approx 25, 50, 100$ and 200 nm . The NPs are randomly distributed and laterally several tens of μm apart. (a) Images recorded at various far-field toluene film thicknesses, h_∞ , and cartoons of the corresponding vertical film cross sections (not to scale laterally). (b) In red the brightness variation of far-field (planar) film sections with time (due to evaporation) and in blue their corresponding film thickness, h_∞ .

observed local gray level variations. The cartoons next to each microscopy image suggest the vertical cross-sections through the liquid films including the NPs².

5.4 Occurrence of optical footprints as a function of the far-field film thickness for different liquids

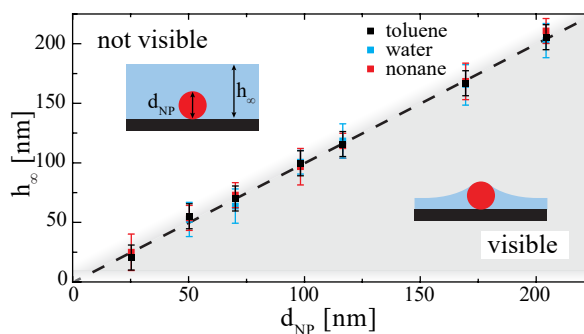


FIGURE 5.3: Region where NP footprints are not observed ("not visible") and where footprints are detected ("visible") as function of the NP size d_{NP} and of the far-field film thickness h_{∞} for various liquids (toluene, water and nonane). The dashed line marks $h_{\infty} = d_{NP}$. The Pt-NPs had diameters of 25, 50, 70, 100, 120, 170 and 200 nm.

Figure 5.3 presents results from optical imaging of substrates during the evaporative thinning of films of various liquids (toluene, water, and nonane) that were deposited on substrates with individual NPs of different diameters d_{NP} attached to them. The data are based on measurements analogous to those presented in Figure 5.2. The Figure shows the range where local optical footprints caused by NPs are observed as a function of the NP size, d_{NP} , and of the far-field film thickness, h_{∞} . The Figure shows that optical footprints of the NPs are only visible if there is a liquid film with $0 < h_{\infty} \leq d_{NP}$. For dry samples and for $h_{\infty} > d_{NP}$ optical footprints such as those presented in Figure 5.2 are not observed.

5.5 Meniscus profiles derived from the local gray levels

Figure 5.4 presents the translation of the optical footprint (locally varying gray levels) caused by a NP into the geometry of the surrounding meniscus. The NP with a diameter of 200 nm is embedded in toluene films with far-field thicknesses of $h_{\infty} = 150, 90, 50,$ and 20 nm. The column on the left shows the optical images. The column in the middle presents the gray level variations on a line through the center of the location of the NP. The right column depicts the meniscus geometry as it has been derived from the gray level variations. For the derivation of the meniscus profiles it is assumed that the imaged gray level can directly be translated into the local film thickness of the imaged spot (see Figure 5.2(b) and Methods section). Even though the diameter of the NP is much less than 1 μm , the meniscus profiles extend up to

²Please note that in the cartoons of Figure 5.2(a) the lateral and vertical scales are different by about a factor of 100 to enable a reasonable visualization of the NPs and their environment.

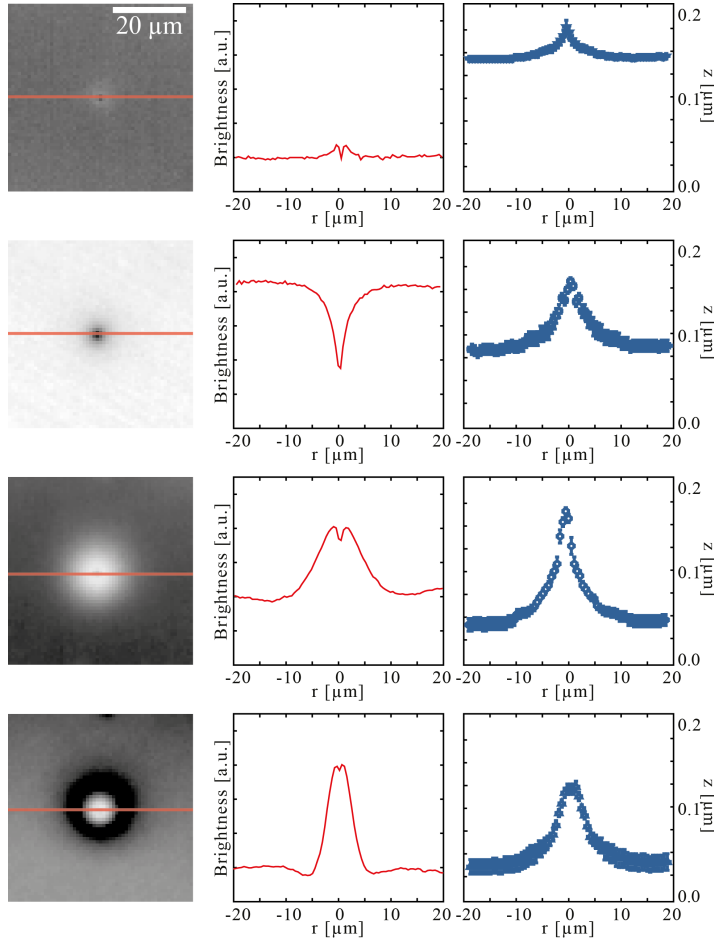


FIGURE 5.4: Translation of optical footprint data into meniscus geometries. Depicted is the case of an individual NP ($d_{NP} = 200$ nm) embedded in toluene films of different thicknesses. Left column: Optical reflection images at film thicknesses $h_{\infty} = 150, 90, 50,$ and 20 nm. Middle column: Gray level variations along lines through the center of the NP. Right column: Translation of the gray levels of individual camera pixels into the local film thickness. Assumed is the same relation between gray level and film thickness as for planar film sections.

$\approx 10 \mu\text{m}$ away from the location of the NP (the lateral and the vertical scales of the plots of Figure 5.4 are different by about two orders of magnitude). The plots show that the optically measured height in the center at $x = 0$ does not match the (known) height of the NP. It is different for different h_{∞} , decreasing from about 180 nm for $h_{\infty} = 150$ nm to about 120 nm for $h_{\infty} = 20$ nm. This is an optical artifact. The lateral extension of the NP is smaller than the diffraction limit. The data indicate that a one-to-one translation of the gray levels of individual pixels into a corresponding local film thickness is a crude approximation, which may be quantitatively wrong. Therefore the validity of such an analysis has to be investigated. This is done in the following section by a comparison between optical and AFM data.

5.6 NPs embedded in solid polymer films: Meniscus profiles derived from AFM and optical microscopy

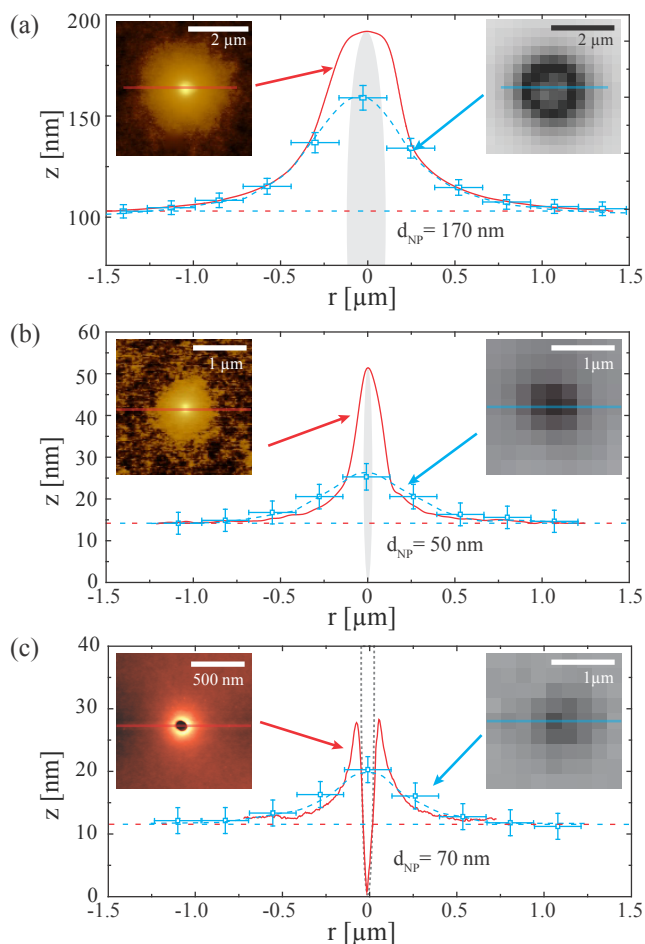


FIGURE 5.5: Comparison between the optical and the AFM signatures of NPs embedded in PS films with a) a NP of 170 nm in diameter ($h_\infty = 100$ nm) and b) of 50 nm diameter ($h_\infty = 15$ nm). c) the 70 nm NPs embedded in a PS film ($h_\infty = 12$ nm) were removed before AFM investigation. The gray ellipsoid represents the spherical NPs. The optical signatures (blue data points) were derived from the gray levels in a zero-order approach (see main text). The blue dashed line is a guide to the eye. The AFM signature (in red) was obtained by tapping mode.

Figure 5.5 presents a comparison between AFM and optical microscopy data of the same sample location with NPs embedded in solid polymer films. Individual NPs were first deposited on a planar silica/silicon substrate. Then thin polystyrene (PS) films were spin cast onto these samples from a polystyrene/toluene solution. The optical and the AFM investigations were performed after complete evaporation of the solvent. Cases (a) and (b) show NPs that are embedded in the PS film. In case (c) the NP embedded in a PS film was removed before the investigation. The Figure shows the AFM data (false colour images and height profiles) and optical imaging data (gray level images and interferometrically derived height profiles (see Figures 5.3 and 5.4)). The lateral scale is so small that individual camera pixels of uniform gray levels can be identified in the optical images. Nevertheless, the lateral scaling

is still much larger (μm) than the vertical one (10 nm), so that the spherical NPs (or their outline as in (c)) indicated in the Figure by the gray area appear strongly elliptically distorted.

The data show that by and large the meniscus profiles measured by AFM and by optical interferometry match. Significant differences between the "true" (expected) and the measured profiles appear only within 200 nm from the NP (or from the center of its former location, as in case (c)). Most likely these differences around $x = 0$ are due to diffraction effects in the case of the optical imaging. Very close to the NPs the AFM data may also not reflect the true shape of the surface topography due to the conical shape of the AFM tip (tip convolution effect). In the case of Figure 5.5(c) a NP of 70 nm diameter was removed after the polymer film formation. This can clearly be seen from the AFM data, whereas the optical data do not reveal the crater-like shape of the surface.

The data depicted in Figure 5.5 reveal two important features: 1.) For comparable NP sizes and far-field film thicknesses the lateral range of the meniscus distortion is significantly smaller for the solid polymer films than for liquid films of pure solvents (see Figure 5.4). This indicates that polymer enrichment in the course of the solvent evaporation during film formation affects the final meniscus shape. 2.) The geometrical meniscus profiles measured by AFM and by optical reflection microscopy are virtually identical within the measurement errors (except for the center region very close to the NP). This means meniscus geometries derived from optical reflection microscopy images are quantitatively correct except for a region of about $0.5 \mu\text{m}$ around the location of the NP.

5.7 Meniscus geometries

Figure 5.6(a) presents experimental data of the geometry of the meniscus profiles in the vicinity of a NP with a diameter of $d_{NP} = 120 \text{ nm}$. For a better visualization of the meniscus distortion the linear scalings of the horizontal and the vertical axes differ by a factor of 80 (the spherical NPs are plotted in scale and therefore appear distorted). The NP was embedded in toluene films with three different far-field liquid film heights, $h_\infty = 29, 42, \text{ and } 71 \text{ nm}$ (indicated by the dashed blue lines). The two data sets depicted represent the profiles from either sides of the NP. According to the data the meniscus reaches out as far as $\approx 5 \mu\text{m}$ away on both sides from the NP. Figure 5.6(b) shows the same data in a lin-log plot. The linear behaviour reveals a logarithmic meniscus profile within most of the meniscus range.

Figure 5.6(c) shows a schematic of the cross section through the NP and the film/meniscus in the vicinity of the NP. It presents the definitions of the various parameters that are used to fit the experimental data. It turns out that all meniscus shapes can be fitted quite well by a combination of a logarithmic (hyperbolic cosine)[131] and an exponential decay:³

$$z(r) = \left[h_0 - h_\infty - r_0 \cdot \ln \left(\frac{r}{r_0} + \sqrt{\left(\frac{r}{r_0} \right)^2 - 1} \right) \right] e^{-\frac{r-r_0}{L}} + h_\infty. \quad (5.1)$$

³detailed calculations are shown in the Appendix A.2

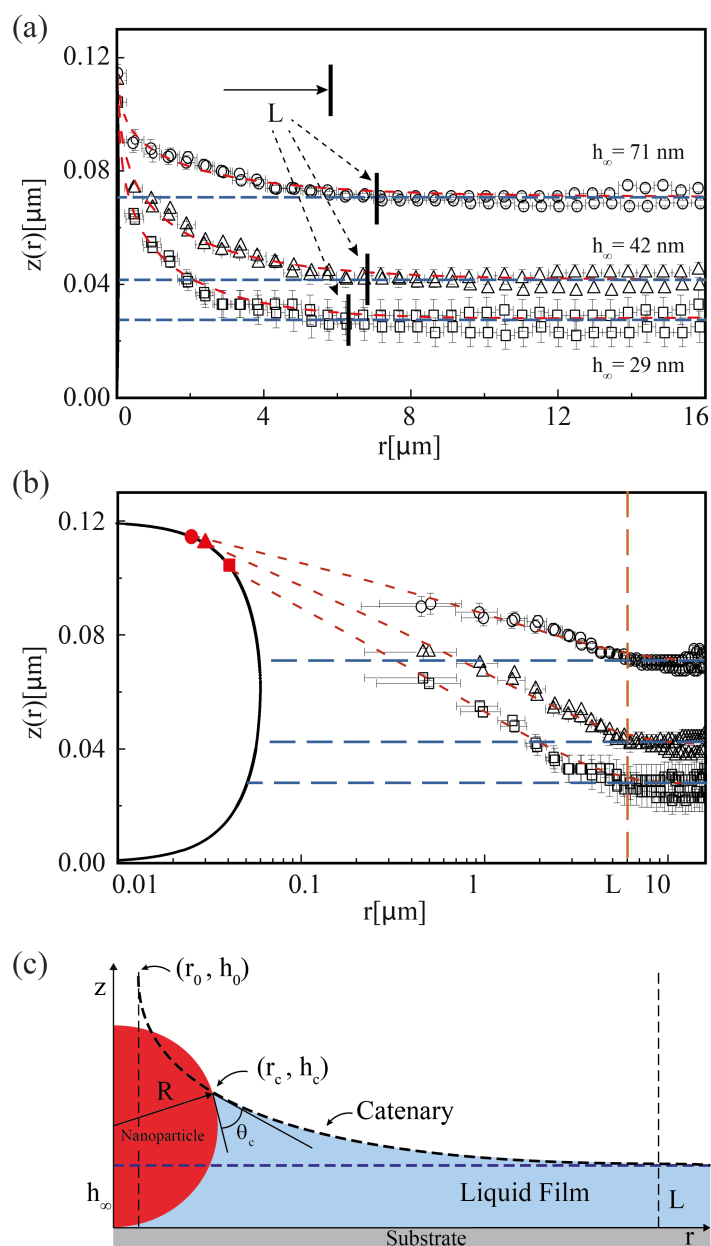


FIGURE 5.6: Meniscus geometries derived from optical reflection microscopy. (a) Lin-lin-plot of the meniscus profiles around a NP with $d_{NP} = 120\text{nm}$, embedded in toluene films of $h_\infty = 29$ nm, 42 nm, and 71 nm as indicated by the blue dashed lines. Each curve consists of two sets of data points (from both sides of the NP) The red dashed lines show a hyperbolic cosine fit of the data points. The vertical and horizontal scales are different by about a factor of 80. (b) Lin-log-plot of the data shown in (a). (c) Cartoon of the assumed meniscus profiles and definition of the various parameters.

According to this equation the logarithmic contribution dominates for $r < L$ i.e., in the meniscus region up to where the meniscus phases out into the planar film. In this transient region away from the NP, close to $r = L$, the exponential contribution provides a smooth transition between the essentially logarithmic meniscus shape and the flat film. It should be noted that the profile of Equation 5.1 formally describes a meniscus shape with its left vertex contacting an (imaginary) vertical

round cylinder of radius $r = r_0$ at a height $z = h_0$ with a contact angle of $\Theta_c^{cy} = 0$. Mathematically this profile is identical to a meniscus, which intersects a NP with radius R at $r = r_c$ and at a height $z = h_c$ with a contact angle Θ_c^{NP} between the liquid and the NP surface (for details see Appendix A.2).

Figures 5.6(a) and (b) demonstrate that the experimental data can nicely be fitted (red dashed curves) with the profile described by Equation 5.1. The linear-logarithmic plot Figure 5.6(b) shows a linear behaviour in virtually the entire meniscus range between the contact with the NP and the transition to the planar far field film surface. Practically, for fitting the experimental data, the exponential contribution of Equation 5.1 is rather negligible. It is only necessary to formally provide a smooth connection between the logarithmic meniscus profile and the planar far-field film surface. Figure 5.6 (b) also shows that fits of the experimental data with meniscus profiles according to Equation 5.1 yield rather well-defined distortion lengths L . Regarding interfacial physics, the logarithmic meniscus shape means that the liquid surface on the meniscus has nowhere a net local curvature. Hence there is no capillary pressure difference between the liquid in the meniscus section and the liquid within the surrounding planar film.

5.8 Universal meniscus profile and distortion length L

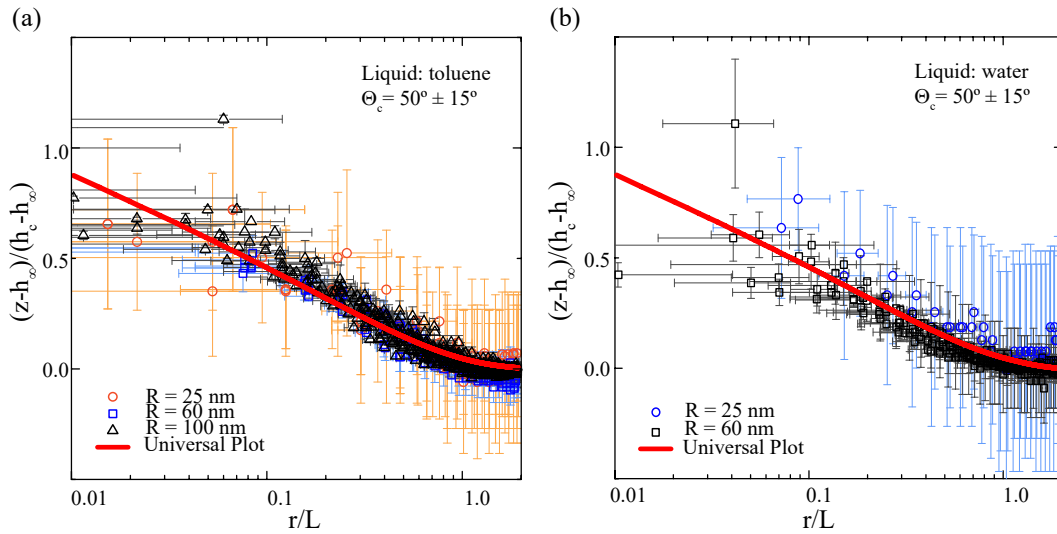


FIGURE 5.7: Meniscus geometries as measured for different NP radii, R , and film thicknesses, h_∞ . The data are fitted according to the profile presented in Figure A.1 and plotted in a universal way by rescaling the x-axis (lateral distance from the center of the NP, r) with the distortion length, L , and the y-axis (net vertical meniscus elevation, $z - h_\infty$) with the net distance between the film surface and the contact with the particle at $h_c - h_\infty$. Singled out by colour are those data points, where the interference conditions lead to a rather weak thickness contrast (orange data points in (a) and blue data points in (b)). Although technically this leads to rather large systematic error bars, the data still reflect the general behaviour quite well.

All the individually measured experimental meniscus profiles can be fitted quite well with the profile described by Equation 5.1, yielding different L , Θ_c , h_c , r_c , as

well as h_0 and r_0 for the different known/measurable R and h_∞ . Because all menisci can be universally described by Equation 5.1 they also can be plotted in a universal way with proper axis scaling. This is demonstrated by Figure 5.7 presenting a large number of experimental data from different sized NPs embedded in films of different thicknesses. The films consisted of (a) toluene and (b) water. All the fits indicate for both liquids the same contact angle with the NPs of $\Theta_c \approx 50 \pm 10^\circ$.

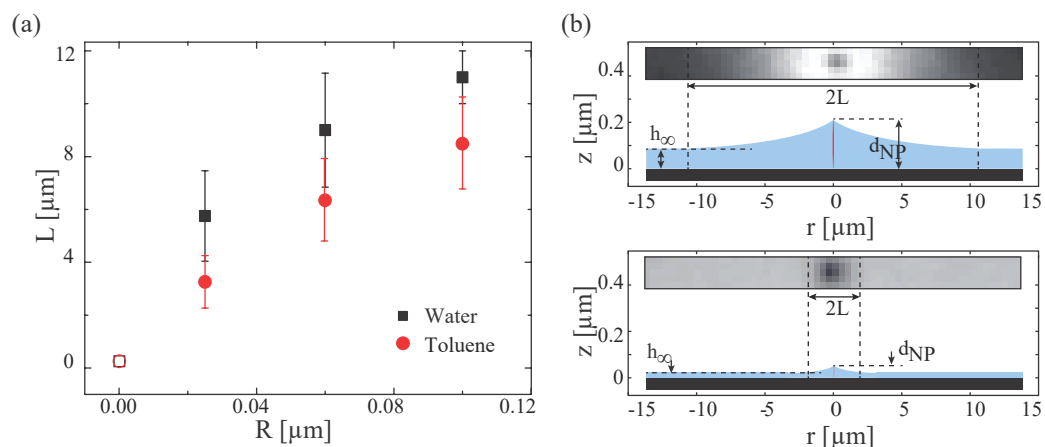


FIGURE 5.8: (a) Distortion length L vs NP radius R as derived from the fits of the experimental data. The open circles/squares at the origin indicate the data that are expected at this point. (b) Optical imaging raw data and corresponding cartoons of the derived meniscus shapes for the combination of $d_{NP} = 200$ nm, $h_\infty = 90$ nm (top) and $d_{NP} = 50$ nm, $h_\infty = 12$ nm (bottom). The lateral and the vertical scales are different by nearly two orders of magnitude (the NPs appear as very elongated red ellipses).

Figure 5.8(a) shows a plot of the distortion lengths L vs the NP radii R . L is derived from fits of the experimental measured meniscus profiles. It can be seen that L increases with R in a slightly non-linear fashion (assuming that the origin is a data point). It is also observed that L of water is always slightly larger than L of toluene. Quite remarkable, L is independent from h_∞ .

Figure 5.8(b) illustrates the findings presented in Figure 5.8 through a combination of raw imaging data from real experiments and schematics, which show the corresponding cross sections of the liquid film plus NP in the same lateral scale. Depicted are the cases of $d_{NP} = 200$ nm and $h_\infty = 90$ nm as well as the combination of $d_{NP} = 50$ nm and $h_\infty = 12$ nm. The lateral scales of all microscope images and cartoons are the same. The vertical scales in both cartoons are the same but different to the corresponding lateral scales (hence the strongly distorted shape of the spherical NPs).

5.9 Discussion

We demonstrate that it is relatively easy to locate with conventional optical reflection microscopy small, individual NPs, if they are embedded in films about as thick or thinner than their diameter. Their location can be detected by conventional optical microscopy although they are much smaller than the Rayleigh diffraction limit. This

is because NPs embedded in a film distort the adjacent film surface and it turns out that this surface distortion ("meniscus") reaches out laterally orders of magnitude further than the size/diameter of the NPs. This unexpectedly large meniscus region creates a rather pronounced optical "footprint" and thus enables the tracking of the NP location.

The configuration of individual NPs attached to a planar surface and embedded in a film of a thickness similar to the diameter of the NP or less is investigated in detail. To this end planar substrates with attached individual NPs are coated by evaporative spin casting with continuously thinning planar liquid films. During film thinning the substrate surface is investigated with reflection optical microscopy. A combination of interferometry and optical imaging provides the local film thickness with nanometer (vertically) and micrometer (laterally) resolution, respectively. Because the lateral extend of menisci caused by even rather small NPs exceeds micrometers, their geometry can be measured optically. This is tested and confirmed by calibration experiments with AFM for the case of solid polymer films.

The meniscus shapes are measured and analyzed as a function of 1.) the diameter of the NPs, 2.) the far-field thickness of the surrounding films, 3.) the composition (surface tension) of the films, and 4.) the state (solid vs liquid) of the films. It turns out that the decay length L of the menisci depends on the size of the NPs, d_{NP} [110]. L increases non-linearly with the NP size, from a few μm for NPs with 25 nm diameter to about 10 μm for NPs with 200 nm diameter. L is independent from the far field film thickness h_∞ . In general L is slightly higher for water films compared to toluene films. For solid polymer films L is substantially smaller than for the liquid films. This may be attributed to polymer enrichment processes in the late stages of film drying, because L of the liquid polymer/solvent solutions during solvent evaporation is similar to the one of the pure solvent (toluene). Even in the cases of the system with pure solvents evaporation may influence the meniscus shape (and vice versa) e.g., through a locally varying evaporative flux because of the meniscus shape ("coffee ring effect"[132]). However, this appears unlikely, because in real scale the menisci are nearly flat and the net meniscus curvature is zero.

All menisci can be fitted with a cosine hyperbolic profile (except for the region at the transition to the planar film, which can be fitted with a decaying exponential). The cosine hyperbolic profile means that there is no net curvature in the meniscus region. Therefore there is no capillary pressure i.e., the liquid in the meniscus region is in pressure equilibrium with the liquid of the far-field planar film.

An unexpected result is the magnitude of L . In macroscopic systems, where gravitation plays a role, the capillary length (typically millimeters) is a measure for L . On the other hand, if the size of the particle causing a surface distortion becomes vanishingly small, it can be assumed that L also becomes vanishingly small. For the intermediate range, with nanosize objects distorting the film surface, gravitation can safely be neglected. L has never been measured up to now in this range and it is not clear what governs its size [110]. It can be assumed that in cases with uncharged, organic liquids (toluene) VdW interactions (disjoining pressure) determine the meniscus shape. Yet the disjoining pressure changes non-linearly with film thickness. Therefore one would expect that the far-field thickness h_∞ has a significant influence on L . However, this is not the case. In addition, there is also no difference in L for substrates with thin silica layers (1.5 nm, natural oxide layer) and

those with artificially grown thick (50 nm) silica layers, although this should make a difference in the Hamaker constant. On the other hand, L is significantly different for water and toluene.

The shape of the meniscus and its decay length L is scientifically of great interest. It reflects and thus reveals the force (energy) conditions in the vicinity of the NPs. Beyond that, it is important because of the capillary interactions between neighboring NPs through the interference between neighboring menisci. For instance, if L is in the range of μm even for NPs as small as only several tens of nm , then neighboring NPs of this size will interact with each other over a distance orders of magnitude larger than their own size and far beyond the range of direct VdW interactions.

The investigated model system of individual spherical NPs attached to planar surfaces coated with liquid films of well defined thicknesses might at first sight appear quite irrelevant for "real" systems. However, it refers to configurations occurring very often in nature as well as in applications. Ubiquitous examples are (thinning) liquid films close to the perimeter of drying drops or at the perimeter of retreating (evaporating) flat films. Also, the investigations presented here bear some relevance for biological systems. Molecularly thin liquid films distorted by embedded NPs are similar to (supported) biological membranes that are locally "distorted" by embedded "particles" such as proteins or protein aggregates. Both, the sizes of the film/membrane thicknesses as well as the sizes of the causes of the distortion can be comparable. Thus it is conceivable, that based on the approach presented here, one might directly be able to measure the lateral extension of the membrane thickness distortions caused by individual proteins or protein aggregates.

5.10 Conclusion

In conclusion, we show how to image with optical reflection microscopy the location of individual NPs attached to planar substrates embedded in liquid films as thin or thinner than the size of the NPs. The NPs are much smaller than the Rayleigh diffraction limit. Nevertheless, they can be detected optically, because they create a distortion of the adjacent film surface (meniscus), which extends laterally over orders of magnitude further than the size of the NPs. Therefore the meniscus shape can even be measured by optical interferometry. The meniscus has cosine hyperbolic (zero net curvature) shape. There is no (capillary) pressure difference between the liquid of the far field planar film and the liquid in the meniscus region. It is unknown what determines the decay length of the meniscus. The decay length is independent from the thickness of the far field planar film. It decreases with decreasing size of the NP. The observation and measurement technique reveals the meniscus shapes of films of nanometer thickness caused by embedded nano size object. Therefore it might be useful for the investigation of biological (supported) membranes with proteins (protein aggregates) as distortion sources.

Chapter 6

Deposition of polymer films by spin casting: A quantitative analysis

The Chapter is reprinted and adapted from:

[34] Jose Danglad-Flores, Stephan Eickelmann, and Hans Riegler. "Deposition of polymer films by spin casting: A quantitative analysis". In: *Chemical Engineering Science* 179 (2018), pp. 257–264. ISSN: 0009-2509.

S. Eickelmann build the experimental setup for the on-line imaging of planar thinning films (Chapter 3.1.1), measured the thinning curves in collaboration with *J. Danglad-Flores* evaluated the thinning data, and wrote the first version of the experimental part of the manuscript. *J. Danglad-Flores* analyzed the data, developed the theoretical description, and wrote the first versions of the manuscript. *J. Danglad-Flores* designed the study under supervision from *H. Riegler*. The manuscript was then revised by *H. Riegler*. All authors provided critical feedback and helped shape the research, analysis and manuscript.

6.1 Abstract

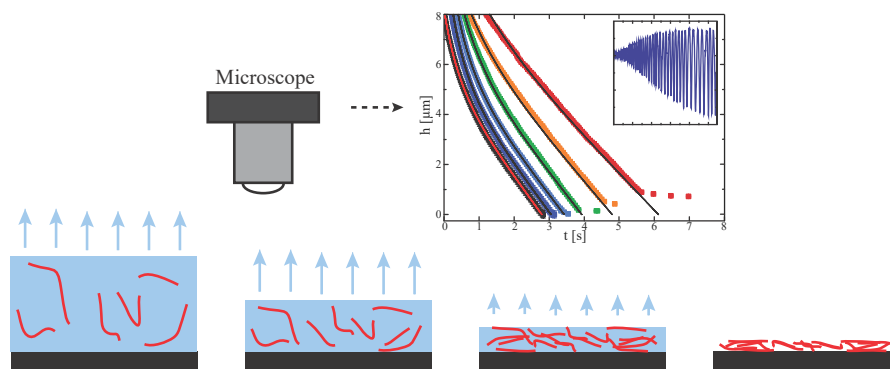


FIGURE 6.1

Spin casting of mixtures of nonvolatile polymeric solutes dissolved in volatile solvents is studied experimentally and theoretically. The final solute coverage, time-resolved film thinning, time-resolved solvent evaporation, and evolution of the solute concentration within the thinning film is investigated for various combinations of different polymers (PMMA, PS, PS-*b*-PMMA) and different solvents (toluene, ethyl-acetate) for a wide range of polymer concentrations and spin cast conditions. The comprehensive data unveil a clear picture of the spin cast process. The findings are translated into a concise theoretical description. Easily available bulk properties of the solvent/solute mixture plus a single "calibration" experiment are sufficient for a quantitative description of the spin cast process including a prediction of the final solute coverage. This and the well-specified boundary conditions render the approach useful for practical applications.

6.2 Introduction

Spin casting (spin coating) is a widely used technique to deposit films of uniform thickness on planar solid substrates [133–135]. In this process a liquid melt or solution is deposited on a rotating substrate. During a transient period the combination of radial and hydrodynamic (viscous) forces will flatten the deposited liquid bulk into a planar film. With on-going rotation this planar film will continuously become thinner [35, 37]. If the liquid film consists of a nonvolatile solute and a volatile solvent, film thinning also occurs due to solvent evaporation in addition to the hydrodynamic thinning. In the beginning, with thicker films, film thinning will be dominated by hydrodynamics. With thin films evaporation will dominate the film thinning process. Hence, to a first approximation spin casting of volatile liquids can be considered as a sequence of hydrodynamic planar film formation and thinning followed by evaporative thinning/drying of this film [36]. If the liquid consists of a mixture of a nonvolatile solute and a volatile solvent, the solvent evaporation causes a continuous enrichment of the nonvolatile solution components. In the end, the solute will be deposited as a dry film.

Even when assuming an idealized hydrodynamic and evaporative behavior film thinning and simultaneously solute enrichment is rather complicated. As a result of the solute enrichment, hydrodynamic and evaporative properties of the film change. This means that viscosity and evaporation behavior change continuously during film thinning. Additionally, since evaporation occurs on the liquid/vapor interface the vertical solute distribution profile changes with time as well, possibly leading to a higher solute enrichment close to the surface ("skin formation" [136], "crust" effect [137]). There are a number of theoretical and experimental studies investigating the combined process of hydrodynamic and evaporative film thinning [36, 38–40, 43, 45, 138–142].

The requirement for a practically useful theoretical description of the hydrodynamic-evaporative spin cast process is that it is describing quantitatively how the film thickness and its composition is evolving with time, under the initial process parameters (rotation, evaporation rate, liquid viscosity, etc.). In particular, it has to predict the final solute coverage. This has been done by Karpitschka et al. [25] in a "zero-order" approach (described in Chapter 2.3). In this approach assumes that

the viscosity and the evaporation rate of the solution remains constant throughout the entire process of hydrodynamic-evaporative thinning. Meaning that viscosity and evaporation rate are assumed identical to those of the pure solvent. Based on easily measurable quantities this rather simple approach predicts the final solute coverage (solute film thickness) with remarkable quantitative precision for low solute concentrations (i.e., for final solute film thicknesses of up to several tens of nanometers).

The following chapter is investigating at which solute concentration this "zero-order" approach starts to fail quantitatively, as well as it can be extended in a simple and practically feasible way into a "first-order" approach for higher solute concentrations i.e., higher final film thickness. In order to investigate this, the hydrodynamic-evaporative thinning of solution films and the final solute coverages is measured and analyzed in detail as a function of the solute concentrations for various solutes and solvents. The limits of the "zero-order" approach is revealed with respect to the significant deviation of the final coverage, solute concentrations, and the thinning behavior. Based on these results a "first-order" description of the spin cast process is presented. The findings offer a rather simple and practically applicable recipe to quantitatively predict final solute film thickness of up to micrometer film thicknesses.

Polymers (PS, PMMA and PS-PMMA Block) dissolved in typical organic solvents toluene (tol) and ethyl-acetate (EA)

6.3 "Zero-order" approach

The "zero-order" approach is described in detail in chapter 2.3. For better readability the important key aspects are summarized in the following.

The thinning of a Newtonian, volatile liquid film of thickness h on a rotating support is described by [36]:

$$\frac{dh}{dt} = -2Kh^3 - E \quad (2.25)$$

E and K also determine the "transition height" h_{tr} , which identifies the film thickness of the transition from film thinning dominated by hydrodynamics to thinning dominated by evaporation:

$$h_{tr} = (E/2K)^{\frac{1}{3}}. \quad (2.27)$$

Because at thicknesses of less than h_{tr} film thinning is mostly due to evaporation, most of the solute, which is contained in the film of thickness h_{tr} (with a solute concentration approximately equal to the weighing in concentration x_0), is finally

deposited on the substrate. This leads to the final film thickness of the solute ¹:

$$h_f = x_0 \frac{\rho_L}{\rho_S} h_{tr} = x_0 \left(\frac{3Ev}{2\omega^2} \right)^{1/3} \approx 0.8 x_0 (K/E)^{-1/3}. \quad (6.1)$$

6.4 Shortcomings of the zero-order approach

For Equations 2.27 and 6.1 it is assumed that K and E are constant up to a film thickness of h_{tr} . For Equation 2.28 it is assumed that K and E are constant during the whole spin cast process. These assumptions are never perfectly correct, because K and E depend on the solute concentration x (which increases continuously due to the solvent evaporation). But for small initial x_0 the absolute increase of solute during film thinning is small even for films much thinner than h_{tr} . Thus Equations 2.27 and 6.1 are pretty accurate and even Equation 2.28 is quite exact.

In the following we will explore what means "small" initial x_0 with respect to Equations 2.28, 2.27 and 6.1 i.e., for which x_0 and at which film thicknesses do film thinning behavior $h(t)$ and final thickness h_f significantly deviate from the "zero-order" scenario [25]. We will also explore the reason of the deviation from the "zero-order" scenario and show how it can be modified in a most simple and practical way, so that quantitative predictions on h_f , on the film thinning behavior $h(t)$, and on the behavior of the solute concentration can be made with a minimum of practical effort based on easily measurable system parameters.

It should be noted that for the zero-order analysis as well as for the first-order approach discussed in the following it is assumed that during the spin cast process the deposited liquid forms a film of uniform thickness, whose thinning is dominated by hydrodynamic flattening in the beginning of the process. The analysis will not be applicable if evaporation changes the solution composition markedly already during the initial transient process when the solution is deposited on the rotating substrate, flattening and forming a planar film. In view of the properties of the solution this means that evaporation rate and viscosity have to be sufficiently low. In view of the spin cast process this means that the deposited amount of liquid has to be sufficiently large, because the evaporative losses of the initially deposited liquid drop scale approximately with its linear dimension i.e., with radius r [132, 143, 144], whereas the time for the liquid flattening scales approximately with the inverse of the linear dimension i.e., with $1/r^2$ (see Emslie [35]). It turns out that typical liquids applied in spin casting, such as toluene or water, deposited in typical quantities (drops of 100 μl and more) on samples of typically a few cm^2 easily meet these conditions as can easily be estimated ².

¹The change in the total volume from the h_{tr} to the dry film is proportional to the solute volume fraction; because the area is constant this proportionality can be translated to the film height; it is practical in most of the cases assume that the volume fraction is equal to the mass (x_0) when solution and solute density are approximately the same $\rho_L \approx \rho_S$

²A rather crude estimation (derived from Fig. 2 of the paper of Emslie [35]) shows that 200 μl of toluene deposited as a sessile drop with a Gaussian contour on a substrate rotating at 1000 rpm (i.e., $K \approx 6 \cdot 10^9 \text{ s/m}^2$) will theoretically become a flat pancake of uniform thickness within $t = 1/(Kr^2) \approx 10 \mu\text{s}$. On a planar substrate of about 1 cm^2 area this planar film is about 100 μm thick. The evaporation rate of toluene for a planar film rotating at 1000 rpm is about 1 $\mu\text{m/s}$. In this case the evaporative

6.5 Thinning Behavior of Concentrate Polymer Solutions

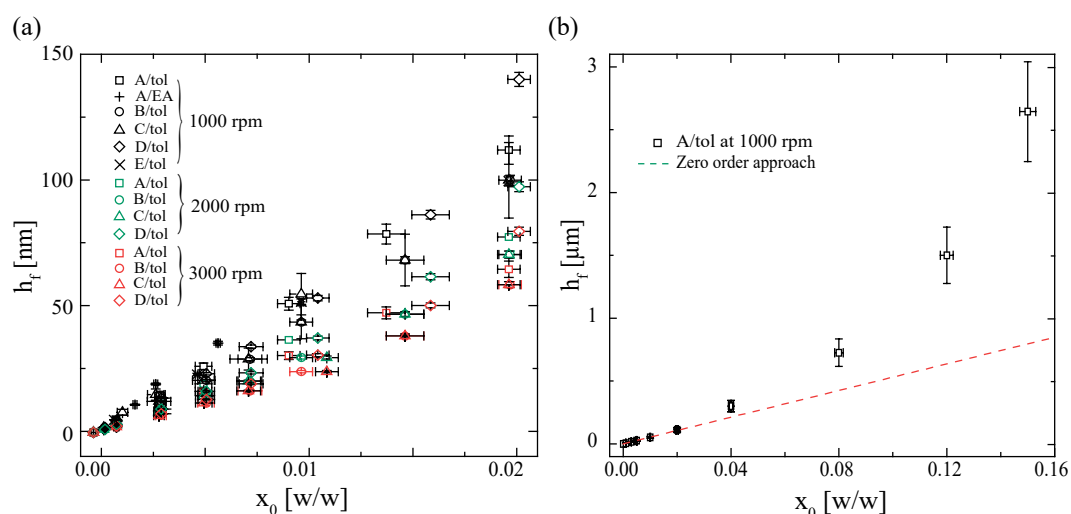


FIGURE 6.2: h_f as Final film thicknesses was measured by ellipsometry and AFM for System A: PS-b-PMMA ($M_n \times 10^3 = 55$ -b-22, B: PS ($M_n \times 10^3 = 25$), C: PS ($M_n \times 10^3 = 50$), D: PS ($M_n \times 10^3 = 195$), and E: PMMA ($M_n \times 10^3 = 996$) deposited from solutions in toluene (tol) and ethylacetate (EA) with various concentrations x_0 (a) shows that for low polymer concentrations up to $x_0 \approx 0.02$ film thickness and x_0 are linearly proportional in agreement with the "zero-order" model (Eq. 6.1). (b) For $x_0 > 0.02$ (i.e., $h > 50$ nm) h_f is increasingly much thicker than predicted in the zero-order calculation.

Fig. 6.2 shows the thicknesses h_f of various polymer films deposited from polymer/solvent solutions with various different initial (in weight polymer concentrations x_0 and different solvents (toluene and EA)). For low concentrations up to about $x_0 \approx 0.02$ film thicknesses h and the initial polymer concentrations x_0 are linearly proportional in agreement with Eq. 6.1 (left panel (a)). For higher polymer concentrations the final film thickness is much higher than predicted (for $x_0 = 0.15$ by more than a factor of 3) as depicted in the right panel (b). The dashed line in panel (b) shows the predicted coverage according to Eq. 6.1 of the "zero order" approximation. Measurements with other solute/solvent combinations yield similar results (see below). Fig. 6.3 depicts the experimentally measured thinning curves (Method description in 3.1.1) for pure toluene and various solutions of PS-b-PMMA in toluene the inset shows separately a measurement with a rather high polymer concentration of 0.15 (w/w). The thinning curves presented in this figure originate from the same experiments that lead to the film thicknesses depicted in Fig. 6.2. The various curves are plotted with different offsets in time (shifted laterally) to enable their presentation within the same figure without overlapping. The solid (fitting) lines are the theoretically predicted thinning curves based on the first-order spin cast scenario presented below. In all cases the thinning occurs in the beginning

losses within the flattening time of $10 \mu\text{m}$ will lead to a loss of about 1 nm toluene film, which will reduce the film thickness by a factor of only 10^{-5} ($=1\text{nm}/100\mu\text{m}$). In reality the time from a round drop touching the rotating substrate to a planar film through a sessile drop will last longer than only $10 \mu\text{m}$. But by and large this crude estimation shows that for the given conditions (toluene, drop volume, sample size) evaporation can be neglected during the initial flattening process and the zero-order approximation of the spin cast process can be applied (which is confirmed by experiments[25]).

³final coverage = final thickness, $\rho = \rho$

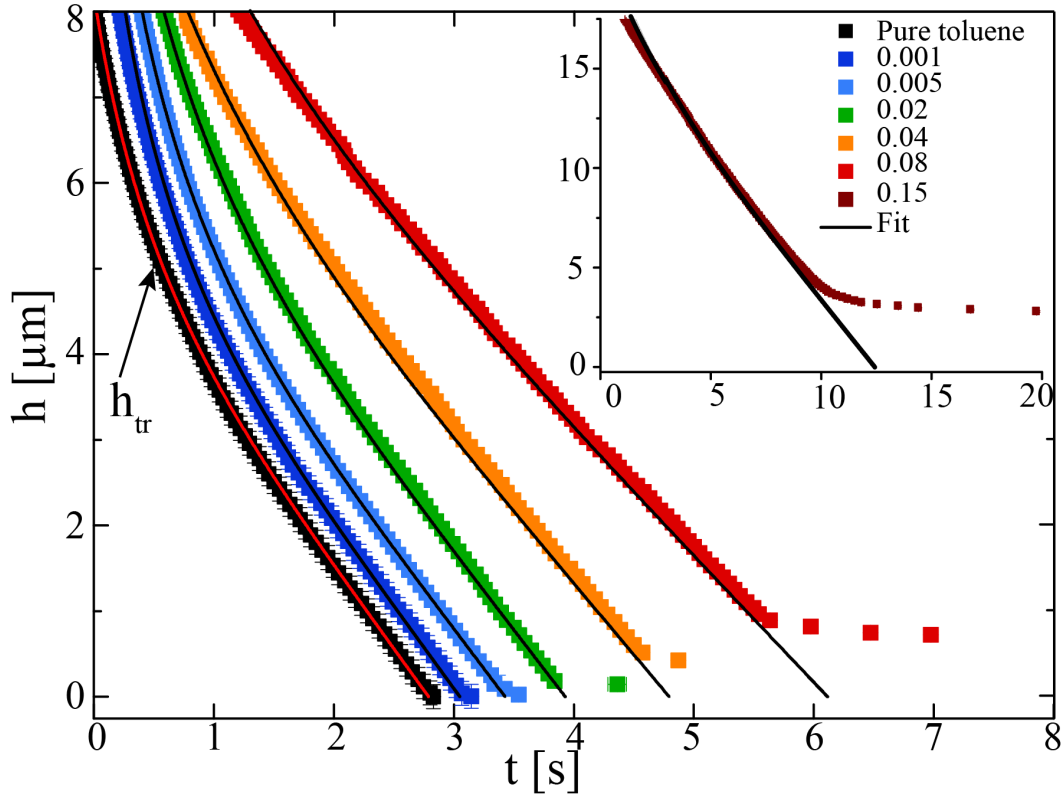


FIGURE 6.3: Experimentally measured thinning curves of pure toluene and various solutions of PS-b-PMMA (MW:55k-b-22k) in toluene. For better visualization the curves are shifted laterally to each other on the time axis. Indicated for the pure toluene is also the transition height as they can be derived from fitting the thinning curve. The solid lines are the theoretical thinning curves according to the first-order model (see main text).

rather rapidly, slows down, proceeds then linearly for some time until it slows down rather rapidly to end upon reaching the final height of the deposited polymer layer. For the lowest polymer concentrations the final thickness of the deposited film is barely visible with the scaling applied in Fig. 6.3. With the weighing in polymer concentrations exceeding about 1% the finally deposited polymer film clearly shows up in the curves. For $x_0 = 0.15$ initial polymer concentration the deposited polymer film is about $2.5 \mu\text{m}$ thick (see inset).

For polymer concentrations of up to about $x_0 = 0.02$ the crossover between the regime of steep and nonlinear hydrodynamic thinning and the linear regime of evaporative film thinning is clearly discernible. This transition range reveals h_{tr} (the h_{tr} indicated in the figure is the result of a fit of the thinning curve based on the first-order spin cast theory as presented below). With pure toluene h_{tr} is about $5.2 \mu\text{m}$. The transition height increases with increasing polymer concentration. With sufficient precision h_{tr} can be derived quantitatively from fitting the experimentally measured thinning curves only for small x_0 . With larger x_0 the crossover between hydrodynamic and evaporative thinning is getting too close to the early transient film formation process when the liquid undergoes the transition from a drop to a film. Therefore, in this case h_{tr} cannot be derived with reasonable accuracy

from the experimentally measured thinning curves. On the other hand, all thinning curves presented in Fig. 6.3 display a rather wide range of a rather linear thickness decrease before the film thinning decreases rapidly due to the final polymer deposition/drying process. Presumably this linear range reflects film thinning dominated by evaporation.

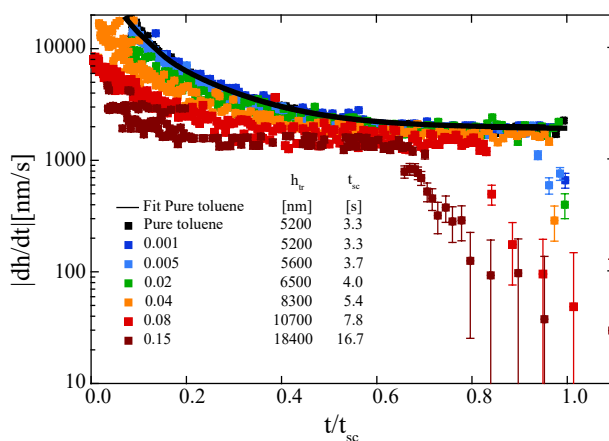


FIGURE 6.4: Slopes of the thinning curves as function of the time. The time is rescaled by the total process time t_{sc} . The polymer concentrations, x_0 , are the initial weighing in values. The solvent is toluene, the polymer is PS-b-PMMA (MW:55k-b-22k)

Figure 6.4 presents the slopes, dh/dt , of the experimentally measured film thinning curves (Fig. 6.3) as a function of the time and the polymer concentrations. The indicated polymer concentrations, x_0 , are the original weighing in values. The time is scaled with the process time, t_{sc} (which is derived/defined with the first-order approach as discussed below). Scaling the time with t_{sc} allows for a convenient presentation of all data in a single plot without too much stretching of the time axis (with increasing x_0 film thinning takes increasingly longer, as demonstrated in particular by the data presented in the inset of Fig. 6.3). Figure 6.4 reveals for all thinning curves a regime of film thinning with a constant slope, intermediate between the early nonlinear hydrodynamic film thinning and the nonlinear drying behaviour at the end of the spin cast process. Except for the experiments with the highest initial polymer concentration ($x_0 = 0.15$), the range of constant slope as well as the slopes therein are nearly identical for all polymer concentrations. For $x_0 = 0.15$ the range of constant slope is shifted to relatively earlier times, but the slope therein is still quite similar to the cases of lower polymer concentration. According to the film thinning scenario (Eq. 2.22) this (constant) slope identifies the evaporation rate E of the liquid film after the film thinning ceases to be dominated by hydrodynamic forces.

At the end of a range with approximately constant slope dh/dt (i.e., constant E), dh/dt abruptly decreases. This sudden decrease of E is quite pronounced for the higher polymer concentrations. For low x_0 the sudden decrease occurs at rather thin films and only within a rather short time. Supposedly this late and rather slowly proceeding film thinning after the range with dh/dt can be attributed to the final drying of a thin, polymer-rich film.

6.6 Evaporation and Spin-Off

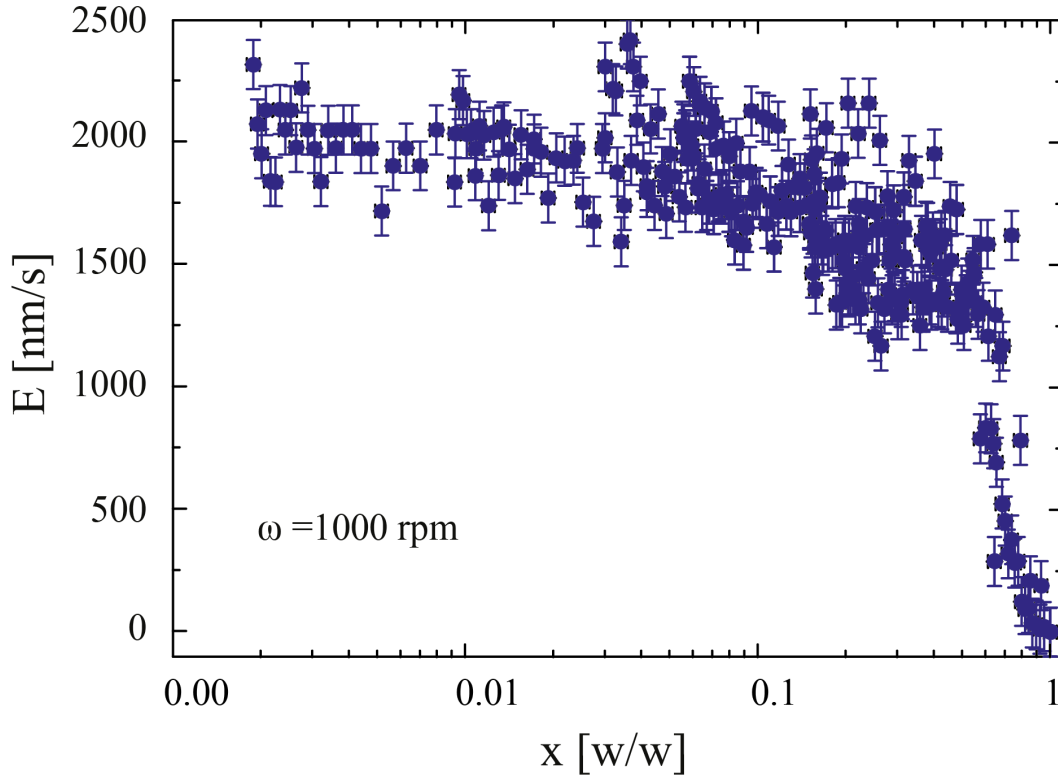


FIGURE 6.5: Evaporation rates E derived from the slopes dh/dt of the experimentally measured thinning curves of film thicknesses below h_{tr} as function of the polymer concentration. Because $h < h_{tr}$ evaporative thinning dominates and $dh/dt = E \cdot x$ is the polymer concentration within the film corresponding to the measured E . It is derived from the original weighing in value, x_0 , by taking into account the loss of solvent due to evaporation. The data were recorded at $\omega = 1000$ rpm.

Figure 6.5 depicts the experimentally derived evaporation rates, E , as function of the actual polymer concentration x (for PS-*b*-PMMA, MW=55k-*b*-22k, dissolved in toluene). The data are extracted from the results depicted in Figure 6.4. To this end it is assumed that film thinning at thicknesses below h_{tr} is dominated by evaporation and accordingly the polymer concentration is given by:

$$x(h) = \frac{h_{tr}}{h} x_0. \quad (6.2)$$

Figure 6.5 reveals that up to a polymer concentration of about $x = 0.05$ the evaporation rate remains identical to the one of pure toluene. Furthermore, even up to about $x = 0.5$ the evaporation rate decreases only by about 25%.

Figure 6.6 presents the spin cast parameters, K , as function of x_0 . The inset presents the bulk viscosities of the polymer solutions as function of x_0 measured by a rheometer. The "Experimental K " values are calculated from the experimentally measured viscosities via Equation 2.23. The "Fitted K " values are derived from best fits of the experimentally measured thinning curves assuming that they are following Equation 2.22. For the fits/simulations it is assumed that the evaporation rate is

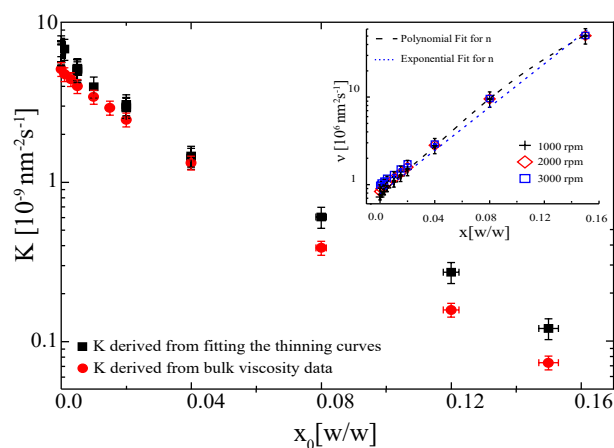


FIGURE 6.6: Spin cast parameters K plotted as a function of x_0 , the weighing in polymer concentration (MW:55k-b-22k, dissolved in toluene). The full black squares present K derived from best fits of the experimentally measured thinning curves according to Equation 2.22 and assuming (constant) evaporation rates E as derived from the intermediate, constant slope of the thinning curve (For the fits the thinning behavior (Fig. 6.5) during the initial transient transformation from a drop to a film of uniform thickness as well as the thinning during the final film draying is neglected). The full red circles in the main frame depict K calculated with Equation 2.23 from the viscosities obtained by the bulk measurements (see inset). The inset shows the dynamic bulk viscosities from bulk solutions at different concentrations and shear speeds (measured with a rheometer Anton Paar MCR 301). Also shown are fits of the bulk viscosity data (dashed: polynomial; dotted: exponential; see also main text).

constant and identical to the value revealed by the intermediate, constant slope of the corresponding thinning curve as depicted in Figure 6.5 (i.e., essentially assuming in all cases the same E of $\approx 1.8\mu\text{m}/\text{s}$ except for $x_0 = 0.15$ with $E = 1.5\mu\text{m}/\text{s}$). Figure 6.3 shows some examples of such fits together with the corresponding experimental data ⁴.

The inset of Figure 6.6 shows that the viscosities of the polymer solution changes by about 2 orders of magnitude if the polymer concentration increases from $x = 0$ to $x = 0.15$. The solutions were investigated at three different speeds. As can be seen they behave like a Newtonian fluid. The experimental data could be fitted quite nicely with a polynomial of third order ($\nu = 10^6\rho^{-1}(13.3x^3 - 0.29x^2 + 0.035x + 0.0006)$) following ref. [145] as well as exponentially ($\nu = 700\rho^{-1}\exp(28.5x)$) according to refs. [146, 147]; the density of the solution was taken as mass fraction proportionality from the density of each component (see Material and Method).

The change of two orders of magnitude in ν is reflected in the decrease of K , which decreases by nearly two orders of magnitude when the polymer concentration increases from $x_0 = 0$ to $x_0 = 0.15$. Figure 6.6 reveals that K derived from fitting

⁴The fits assume that the thinning curves start at infinite thickness and end at zero thickness without any polymer/solute deposition i.e., a pure solvent with the E and K of the real polymer solution. It therefore focuses only on the experimental data in the range (1) after the transient film formation at the beginning of the spin cast process and (2) before the thinning curve shows the deposition of a polymer film at the end of the process. The deviations of the real thinning curve from an idealized thinning curve at the beginning and at the end of the real spin cast process are quite obvious so that the upper and lower cutoff for the fitting range is quite unambiguous.

the thinning curves and K derived from bulk viscosity data agree quite well within the entire range of polymer concentrations. This means that the experimentally measured thinning curves up to $x_0 = 0.1$ can be described by Equation 2.22 with a constant E identical to the one of the pure solvent and K values based on the viscosity of the bulk solutions with the weighing polymer concentrations x_0 .

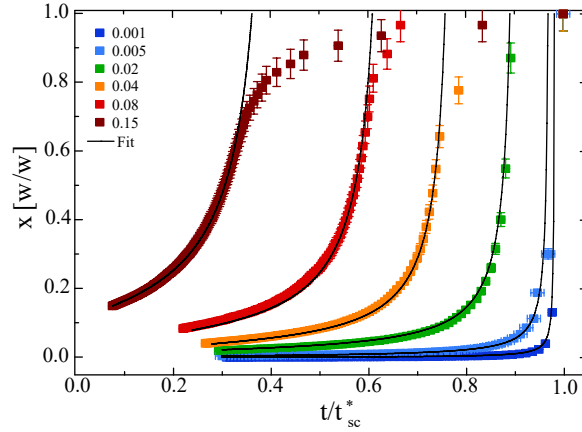


FIGURE 6.7: Time evolution of the polymer concentration x during film thinning for different initial x_0 . The time is scaled with an empirical process time t_{sc}^* ($t_{sc}^* = t_{sc} + a$ with $a =$ an additional time taking into account complete solute drying as derived from the empirical thinning curves (i.e., when $dh/dt = 0$)). The concentration evolution is derived from the empirical thinning curves with $x = x_0 * h_{tr}/h$. The black solid lines are derived from fits to the experimentally observed thinning curves assuming ideal thinning behavior according to Eq. 2.22 with a fixed E of the pure solvent and a fixed K based on the bulk viscosities of the initial solution as shown in Figure 6.9.

Fig. 6.7 supports this assumption by presenting the time evolution of the polymer concentration x as derived according to Equation 6.2 as a function of time. The time is scaled with an empirical process time t_{sc}^* , which is a combination of the t_{sc} plus the additional time for complete solute drying (i.e., when $dh/dt = 0$) as derived from the empirical thinning curves. The black solid lines are derived from fits to the experimentally observed thinning behavior assuming the thinning behavior according to Eq. 2.23 with a constant E (of the pure solvent) and constant K based on the bulk viscosities of the initial solution as shown in Figure 6.6. The experimental data agree with the theoretical curves up to concentrations of about $x \approx 0.65$ or even higher (for the lower initial x_0). At concentrations higher than $x \approx 0.65$ the polymer enrichment slows down (as can also be seen in Figure 6.5).

6.7 Speed depended Evaporation

Figure 6.8 presents the evaporation rates as function of the square root of the sample angular speed, $\omega^{1/2}$ [36, 136, 148]. For $\omega = 0$ the evaporation rates were derived from the loss of weight per time for a petri dish (5 cm diameter, about 0.5 cm deep) filled

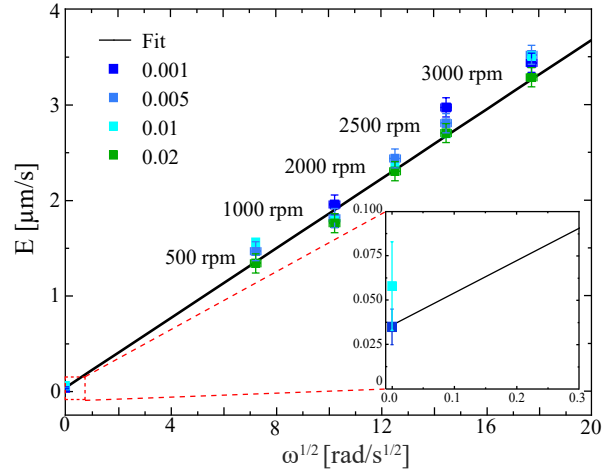


FIGURE 6.8: Experimentally measured evaporation rates, E , for various polymer concentrations x_0 as function of the sample rotation rates ω (PS-PMMA, MW:55k-b-22k, dissolved in toluene). The inset shows the static evaporation rate ($\omega = 0$) as measured from the evaporative weight loss of the solution in a petri dish in still air.

with solutions in an non-convective ambient air environment⁵. The evaporation rates for the range of $500rpm < \omega < 4000rpm$ were derived from the linear sections of the thinning curves. Figure 6.8 shows that the data can empirically be described by:

$$E(\omega) = e_0 + e\sqrt{\omega} \quad (6.3)$$

An excellent approximation for Equation 6.8 for the case of spin casting (i.e. $\omega > 1rps$) is:

$$E(\omega) \approx e\sqrt{\omega} \quad (6.4)$$

Figure 6.9 presents the experimentally measured final polymer film thicknesses, h_f , as function of the initial weighing in polymer concentrations x_0 . The final film thicknesses are scaled by the transition heights, h_{tr} , of the corresponding systems. The data are from different polymers, different solvents, and different speeds of rotation. They agree very well with a linear behavior between the final film thickness of the deposited non-volatile solute, h_f , and the initial (weighing in) concentration, x_0 , of the solute according to Eq 6.1, where $E (=E(\omega))$ has been replaced by e according to Eq 6.3:

$$h_f = x_0 \left(\frac{3ev_0}{2\omega^{3/2}} \right)^{1/3} = x_0 \left(\frac{3e\eta_0}{2\rho_0} \right)^{1/3} \omega^{-1/2}, \quad (6.5)$$

⁵Surface curvature, convection and side walls influence the static evaporation rate and have to be minimized for its experimental determination. Petri dishes with several centimeters in diameter filled to the rim and placed in the nearly completely closed compartment of a precision scale are a reasonably optimized compromise of an experimental setup. Convection is suppressed, the surface is mostly planar, the liquid volume is relatively small and the loss of weight can be measured with high sensitivity/precision.

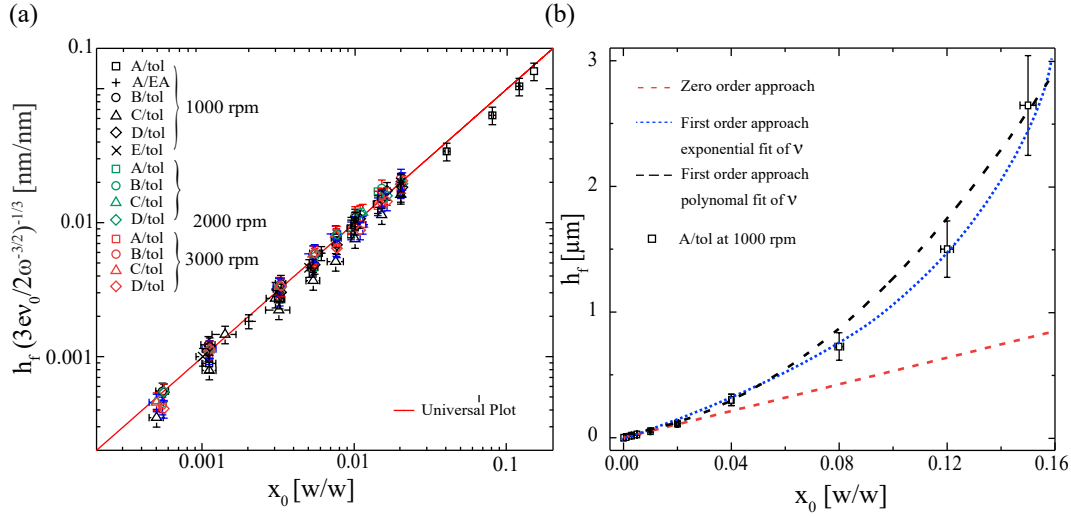


FIGURE 6.9: (a) Final film thicknesses, h_f , as function of the initial weighing in polymer concentrations x_0 . Data are shown for various combinations of polymers, solvents and rotational speeds. h_f is scaled by $((3e\nu_0)/(2\omega^{3/2}))^{1/3}$ assuming constant evaporation rates e of the corresponding solvent ($180 \text{ nm/s}^{1/2}$ for tol and $610 \text{ nm/s}^{1/2}$ for EA) and the bulk kinematic viscosities ν_0 of the solutions with concentration x_0 . (b) shows h_f for polymer A dissolved in TO as function of the initial weighing in polymer concentration x_0 . The dotted line shows h_f predicted according to the zero order approach (see Fig. 6.2). The solid line shows h_f according to the first order approach resulting from Eq. 6.5 with constant e and bulk viscosity properties ν_0 . The red dashed line shows h_f predicted according to the zero order approach (see also Fig. 6.2). The black dashed line shows h_f according to the first order approach from Eq. 6.5 with constant e and bulk viscosity properties ν_0 as presented in Fig. 6.6 and fitted by an polynomial rheological behaviour. The blue dotted line shows the exponential fit of the bulk rheological behaviour

or, assuming that the (weighing in) density of the solution, ρ_0 is independent for the polymer concentration:

$$h_f = c \cdot x_0 \left(\frac{\eta_0}{\rho_0} \right)^{1/3} \omega^{-1/2}, \quad (6.6)$$

with

$$c = \left(\frac{3e}{2} \right)^{1/3}, \quad (6.7)$$

as an instrument and solvent-specific constant, c , reflecting the evaporative conditions of the used solvent in the applied spin cast setup⁶. We developed Equations 6.5, 6.6 and 6.7 to predict the final solute film thickness, h_f , as a function of the four main process parameters, x_0 , ω , η_0/ρ_0 and e for a given instrument. All parameters (instrument- or process-specific) are easily measurable. They are either (1) weighing-in properties (η_0 , ρ_0), easily accessible by bulk measurements, (2) at hand, adjustable process parameters (x_0 , ω), or (3) parameters accessible with one single experiment (e from the measurement of h_f for a given set of η_0 , ρ_0 , x_0 , and ω).

⁶the evaporative conditions are quite similar for different spin cast instruments, as long as the ambient vapor phase is not coming close to becoming saturated with the solvent vapor. The main parameter affecting the evaporation is the rotation.

6.8 Discussion

In this chapter we analyze the deposition of polymer films onto planar substrates by spin casting polymer solutions with volatile solvents. Our focus is on measuring and understanding in detail how the hydrodynamically flattened solution film gets thinner due to hydrodynamics and evaporation, and finally forms a dry polymer film. We are interested in particular on the behavior of solutions with a relatively high polymer concentration, which lead to final dry polymer film thicknesses of up to several micrometers. In this case the simple zero-order approach that was presented earlier[25], which essentially neglects the impact of the dissolved solute on the spin cast process, is quantitatively not correct any more. Figure 6.2 reveals experimentally above which weighing in solute concentrations, x_0 , the zero order approach fails quantitatively with respect of the predicted final film thickness. Details on the film thinning behavior for different polymer concentrations are presented in Figure 6.3. Its analysis (Figure 6.4) reveals the "real" evaporation rates during film thinning (Figure 6.5) i.e., the evaporation rates for films of an actual polymer concentration x that results from the polymer enrichment due to the solvent evaporation. It is found that the evaporation rates are barely affected by the polymer concentration up to $x \approx 0.5$. This can be understood because 1.) of the relatively low *molar* solute concentration even for large x and 2.) there is barely any relative enrichment of polymer close to the film surface. The solute enrichment close to the surface can be estimated as follows: The vertical solute distribution is determined by the competition between the solute enrichment close to the film/air interface due to the solvent evaporation and the solute dilution due to diffusion away from the film/air interface. The relative strength of these antagonistic effects is characterized by the Sherwood number[25] (Peclet number, mass transfer Nusselt number). With diffusion coefficients D of typically $\geq 10^{-11} \text{ m}^2/\text{s}$ for the polymers used, $Sh_{h_{tr}}$, the Sherwood number at h_{tr} , is smaller than 1. This small Sherwood number means that the vertical solute distribution within the thinning film is rather uniform at h_{tr} . It also means, to a first approximation, that the solute composition is even more uniform as the film is getting thinner than h_{tr} due to evaporation⁷.

The data of Figure 6.4 show that the evaporation rates are essentially those of the pure solvent for up to $x \approx 0.5$. E decreases only significantly for $x > 0.5$, indicating a drying process of the polymer-rich solution at these polymer concentrations [149]. Still, even with $x > 0.5$ a pronounced polymer enrichment at the film surface ("crust" or "skin" formation) is not likely, because in this case the evaporation rate would decrease much steeper than observed [150]. Due to the rather constant evaporation rates (Figure 6.5) for films much thinner than h_{tr} even for $x > 0.02$, E can be excluded as main reason for the deviation between the measured final film thicknesses and the ones predicted by the zero order analysis. Instead, as main cause for this discrepancy we identify the substantial increase in viscosity with increasing polymer concentration as depicted in Figure 6.6. Most remarkable, K_0 i.e., the *weighing in* kinematic viscosity ν_0 is the key parameter, which determines the final film thickness h_f . Its impact on the final film thickness results from its impact on the transition

⁷ $Sh = (Eh)/D$ with E = evaporation rate, h = characteristic length (in this case the film thickness), and D = diffusion coefficient. Sh is largest for the largest h i.e., for $h = h_{tr}$

height, h_{tr} . With decreasing K the transition between hydrodynamic and evaporative thinning is shifted to larger film thicknesses, resulting in thicker final solute film thicknesses, h_f . The variation of K respectively ν during film thinning has no influence on h_f , because this variation occurs essentially during evaporative film thinning. In this case the amount of solute per film area i.e., h_f , remains constant. Figure 6.8 presents experimental data on the evaporation rates as function of the rotation speed including the case of $\omega = 0$. The findings confirm the square root dependency that has been discussed already in the literature [36, 136, 148].

Figure 6.9 presents in a universal plot the relation between the final thicknesses, h_f , and the initial polymer concentration, x_0 , for different polymers, solvents and rotation speeds. The final film thickness is normalized with the transition heights of each experiment based on solvent-specific and instrument-specific evaporation rates e , as well as ν_0 , the measured weighing in kinematic viscosity of the solutions. The excellent agreement between the measured data and the data calculated with Equation 6.6 demonstrates the validity of the first-order approach leading to Equation 6.6. It is an astonishingly simple correction to the zero-order approach. One has just to replace the viscosity of the pure solvent by the viscosity of the solution. Equation 6.6 is very useful for practical spin cast applications because η_0 and ρ_0 are easily measurable bulk properties. Also accessible right away is ω . And the solvent- and instrument-specific value for e can be determined with just one experimental measurement of h_f through Equation 6.6.

We are fully aware that there can be found in the literature quite a number of experimental and theoretical studies addressing similar topics as analyzed in this chapter [134]. However, what has been published before is often patchwork, presenting bits and pieces of different aspects of spin casting. The experimental findings are often confusing, presenting a plethora of data without clear dependencies on parameters and without well-defined boundary conditions.

In particular the relation between the final solute film thickness and whatever is considered as relevant spin cast parameters is addressed in several previous publications. Indeed data similar to Figure 6.2 can be found in the literature [36, 151, 152]. On-line thinning curves similar to those of Figure 6.3 have also been published before [153–158]. However, these data were never analyzed in detail theoretically in respect to a simple, transparent spin cast scenario without a guesswork of adjustable parameters. For instance, experimental findings have been explained with evaporation rates and/or viscosities, which (supposedly) continuously vary during the spin cast process due to the solute enrichment. Thus, based on suitably selected adjustable parameters these models *explain* the experimental findings. But these earlier models fail to *predict* the result of a spin cast process quantitatively, in particular on a more general, universal scope, because the models are based only partially on solid experimental data. Up to now nobody has actually measured *in vivo* the evaporation rates during the film thinning and solute enrichment. Data as presented in Figures 6.4, 6.5 and 6.7 are not available in the literature. The result of these new experimental insights is a rather universal, concise theory, which (1.) accurately predicts the final film thickness for a wide range of thicknesses (Figure 6.9), (2.) is based on only a few measurable (bulk) quantities (Equation 6.6), (3.) is supported by experimental data (in particular Figure 6.4) and, (4.) is based on a simple, transparent physics approach.

6.9 Conclusion

In conclusion, we present here for those who want to apply evaporative spin casting (a solution of a nonvolatile solute and a volatile solvent) a lucid and well-defined "recipe" to achieve a specific solute coverage. In particular, based on detailed experimental investigations, we reveal and discuss in a transparent approach how we extract our final "master" formula (Eq. 6.6). Step-by-step we explicitly relate the theoretical description to the experimental observations and specify the boundary conditions of its validity. It turns out that the spin cast process is rather straightforward even for relatively high solute concentrations. Only a few easily measurable bulk system parameters (η_0, ρ_0, ω) and one "calibration" experiment (determination of "e") are sufficient to describe the process and to predict its main result, the final solute coverage. Beyond that, the data and analysis presented in this chapter disclose a transparent picture on the physics occurring during evaporative spin casting, such as the thinning behavior, the evaporation behavior, and the evolution of the solute concentration.

Chapter 7

Thin Films with Lateral Surface Tension Gradients

The following deals with the evolution of the surface topography of films of binary mixtures of volatile liquids during evaporative thinning. What is the film topography during thinning? Remain the films flat or becomes the surface undulated? Does the film even rupture, and if it does so, at which film thickness? It will be shown that even with liquids, which mix ideally and completely wet the substrate surface, the answers to these questions are not obvious and the findings are unexpected.

7.1 Materials and Methods

The film thinning of mixtures of two volatile liquids is investigated. The liquids are completely miscible. Individually the liquids wet the substrate (silica) completely. In the applied spin cast configuration the pure liquids individually are thinning continuously by evaporation and retain a continuous planar film until complete evaporation (dry surface). The liquids have different evaporation rates E and different surface tensions γ . Liquid A is the one with the higher evaporation rate E_f ("f" for faster). Liquid B has the lower evaporation rate E_s ("s" for slower). The corresponding surface tensions are γ^A and γ^B . This defines a surface tension difference:

$$\Delta\gamma^{A,B} = \gamma^A - \gamma^B \quad (7.1)$$

For instance, toluene has a surface tension of $\gamma_{tol} = 28.5$ mN/m and nonane of $\gamma_{non} = 22.8$ mN/m. Thus $\Delta\gamma^{tol,non} = +5.7$ mN/m. The combination of heptane ($\gamma_{hep} = 20.1$ mN/m) and nonane yields $\Delta\gamma^{hep,non} = -2.7$ mN/m. Toluene has an evaporation rate of $E_{tol} = 1800$ nm/s, heptane $E_{hep} = 3000$ nm/s and nonane $E_{non} = 600$ nm/s (all at $\omega = 1000$ rpm). All these liquids are miscible without a miscibility gap and combinations with various ratios of E as well as positive and negative $\Delta\gamma^{A,B}$ can be investigated. The mixing ratios x_0 are the initial ratios (weighing in) prior to liquid deposition and film formation.

7.2 Results

Figure 7.1(a) shows a sequence of microscopy images recorded during the film thinning of a mixture of 10% nonane and 90% toluene. Under each frame cartoons of the suggested film topography are presented. In the beginning at $t=0.604$ s the liquid mixture is virtually planar (the gray level variations indicate a vertical roughness variation of only ≈ 100 nm on a lateral distance of mm). At 1.257 s the film starts to become wavy. This feature becomes more pronounced (1.648 s) and eventually pronounced undulations are formed (1.950 s). At this stage the vertical roughness is in the range of micrometers, comparable to the (average) film thickness. The holes of the undulations finally come into contact with the substrate. The film ruptures and splits into individual drops (2.003 s). These drops continuously become smaller through evaporation and after some time the substrate is completely dry (5.132 s).

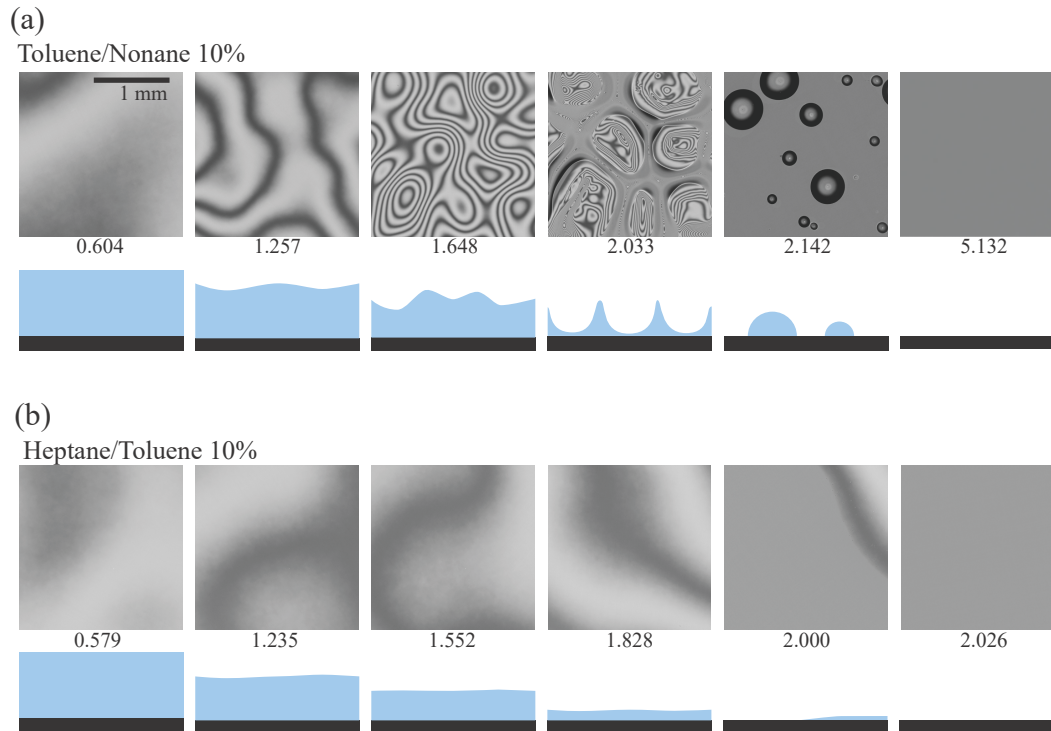


FIGURE 7.1: (a) Time sequence of optical microscopy imaging of a binary mixture of 10% nonane and 90% toluene ($\Delta\gamma^{\text{Tol, Non}} = +5.7\text{mN/m}$). Below each frame, a proposed cross section of the film topography is shown. (b) ditto with 10% toluene in 90% heptane ($\Delta\gamma^{\text{Non, Hepp}} = -8.4\text{mN/m}$).

Figure 7.1(b) shows the evaporative film thinning behaviour of a mixture of 10% toluene and 90% heptane. In contrast to the nonane/toluene mixture the film remains rather flat during its evaporation/thinning (it is not perfectly flat as in particular the image taken at time 2.000 s reveals. But it is flat in comparison to the case (a)).

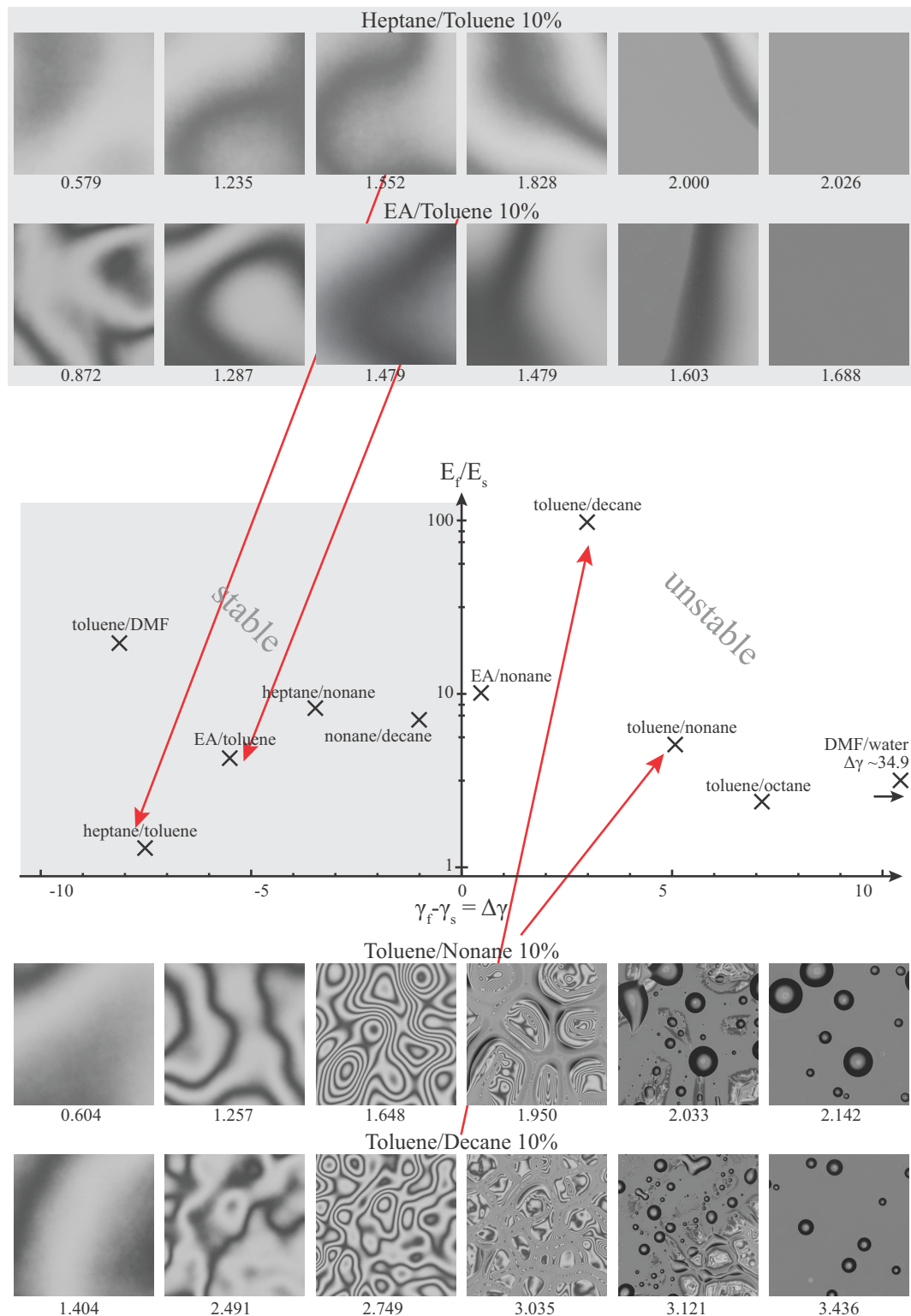


FIGURE 7.2: Overview with many mixtures. These remain either flat during the entire film thinning process ("stable") or develop an undulated surface topography and even rupture ("unstable") during the evaporative film thinning.

7.2.1 Film topography evolution of many different binary mixtures with component ratios of 90% to 10%

Figure 7.2 shows at the top as example two different liquid combinations, were the films remain planar (10% toluene and 90% heptane as well as 10% toluene and 90% ethylacetate (EA)). With the two mixtures on the bottom (10% nonane and 90% toluene, 10% decane and 90% toluene) the film is planar in the beginning, then it starts to become wavy, forms undulations, and finally ruptures and forms drops. The center shows an overview over all the liquid combinations (with 10% slow evaporation component and 90% fast evaporating component) that were investigated. The vertical axis of this "phase diagram" denotes the ratio of the evaporation rates E_f/E_s . The horizontal axis denotes the surface tension difference $\Delta\gamma^{A,B}$. The plot reveals that 10/90 mixtures with $\Delta\gamma > 0$ result in unstable films, whereas mixtures with $\Delta\gamma < 0$ remain stable and planar during the entire evaporative film thinning.

7.2.2 Film topography of mixtures with $\Delta\gamma > 0$ as a function of the mixing ratio

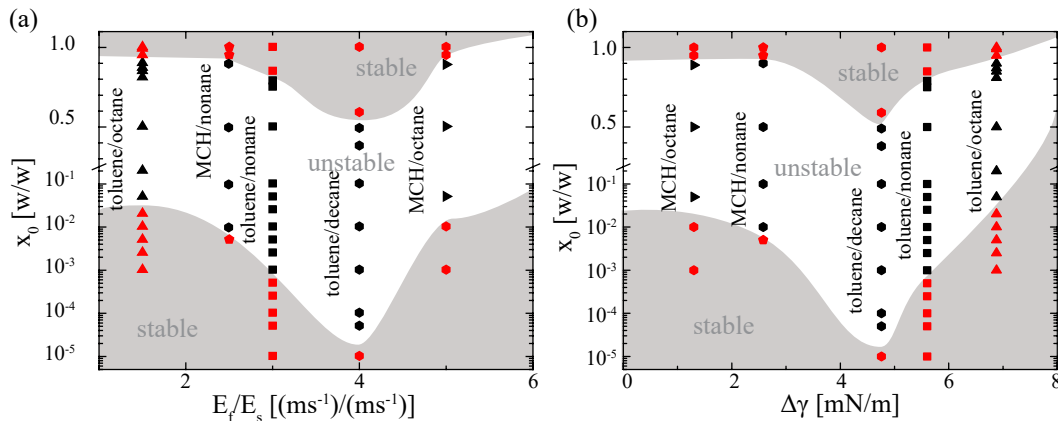


FIGURE 7.3: a) Stable (red data points) and unstable (black data points) regions as function of the composition and of the ratio of the evaporation rates. (b) ditto as function of the surface tension differences $\Delta\gamma$.

Figure 7.3(a) shows a phase diagram (stability diagram) for various mixing ratios x_0 as function of the ratio of the evaporation rates E_f/E_s . Figure 7.3 (b) shows the same data with x_0 vs. $\Delta\gamma$.

Figure 7.4 shows yet another plot of the experimental data with x_0 as a function of $\Delta\gamma \cdot E_f/E_s$. This plot organizes the data in a more simple way. It shows that if x_0 and $\Delta\gamma$ are very small, the films are stable. On the other hand, if x_0 is larger than 80%, then the films also remain planar.

7.2.3 Evolution of the undulation wavelength as function of the ratio x_0

Figure 7.5 presents the time evolution of the undulation topographies for three different weighing in ratios of mixtures of nonane/toluene (10/90, 1.00/99.0, and

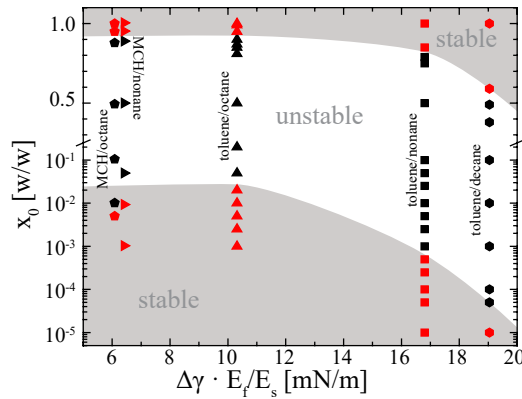


FIGURE 7.4: Stable (red data points) and unstable (black data points) regions as function of the composition and of the ratio of the evaporation rates times the surface tension difference.

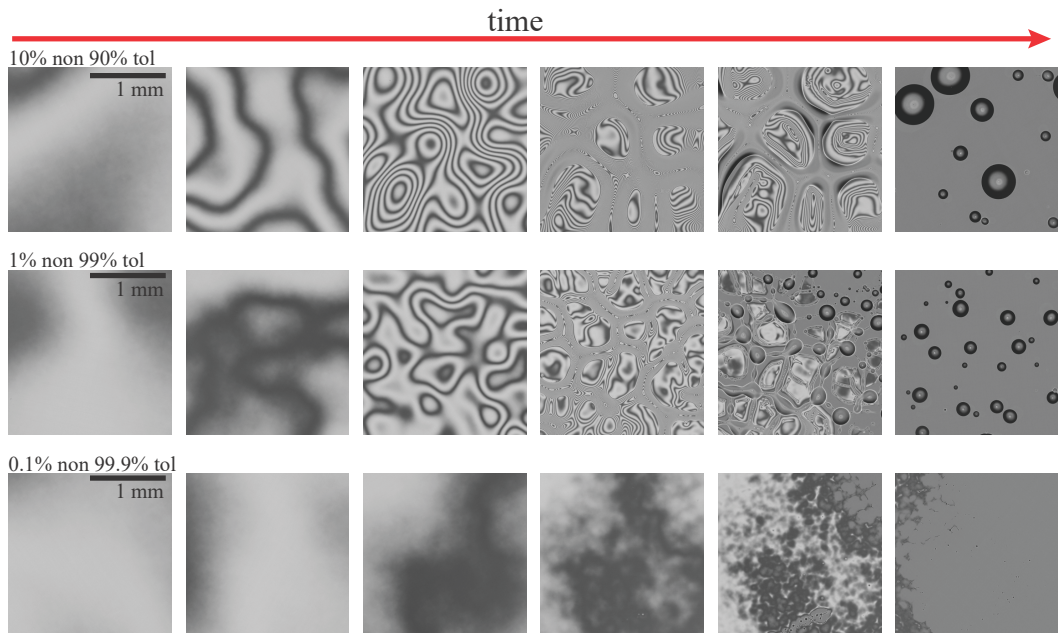


FIGURE 7.5: Evolution of the undulations with film thinning (proceeding time) for different nonane/toluene mixtures (10%, 1%, and 0.1%).

0.10/99.1). One can see how the wavelengths and their time evolution is different for different inweight mixing ratios. With the higher toluene concentrations the undulations appear earlier and the wavelength is larger.

Figure 7.6 presents the initial wavelengths of the undulations as function of the square root of the inweight ratios $\sqrt{x_0}$ for toluene/nonane mixtures.

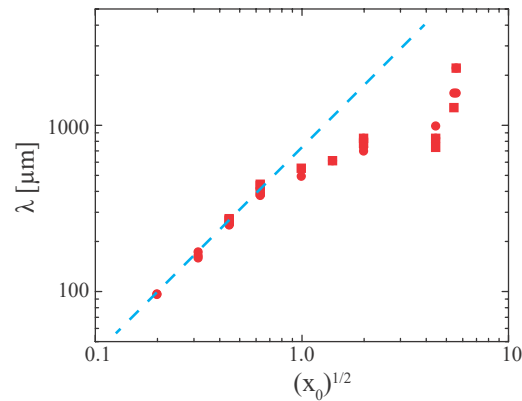


FIGURE 7.6: Initial undulation wavelengths λ as function of the square root of the initial mixing ratio $\sqrt{x_0}$ for toluene/nonane mixtures

7.2.4 Evolution of undulation wavelength during film thinning as a function of time (thickness)

Figure 7.7 presents (a) an image (time) sequence of a thinning film of a 1.00/99.0 nonane/toluene mixture with (b) the corresponding cartoons indicating the topography (and the definition of the wavelength). In the beginning (i.) the film is planar. At (ii.) the surface starts to undulate. With time the undulations become more pronounced, but also the wavelength gets shorter (iii.-iv.) as presented in Figure 7.7(c).

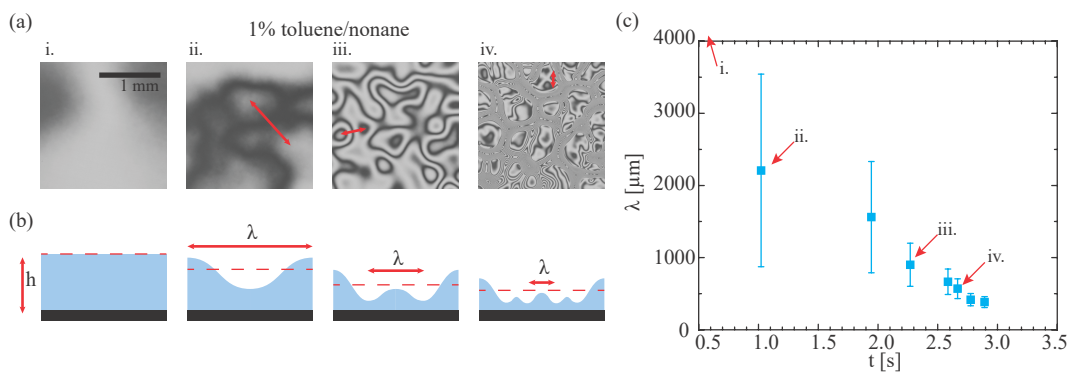


FIGURE 7.7: (a) Frame sequence of the film thinning of a 1.00/99.0 nonane/toluene mixture with corresponding cartoons(b). (c) Plots of the wavelength of the undulations as a function of time.

7.3 Discussion

7.3.1 Destabilization mechanism

The results from Figure 7.2 show that in general mixtures with a negative surface tension difference ($\Delta\gamma > 0$) form stable films (planar film surface), whereas mixtures with $\Delta\gamma < 0$ tend to destabilize during evaporative film thinning. It can be assumed

that the surface tension difference plays an important role in the stability behaviour of evaporative thinning films.

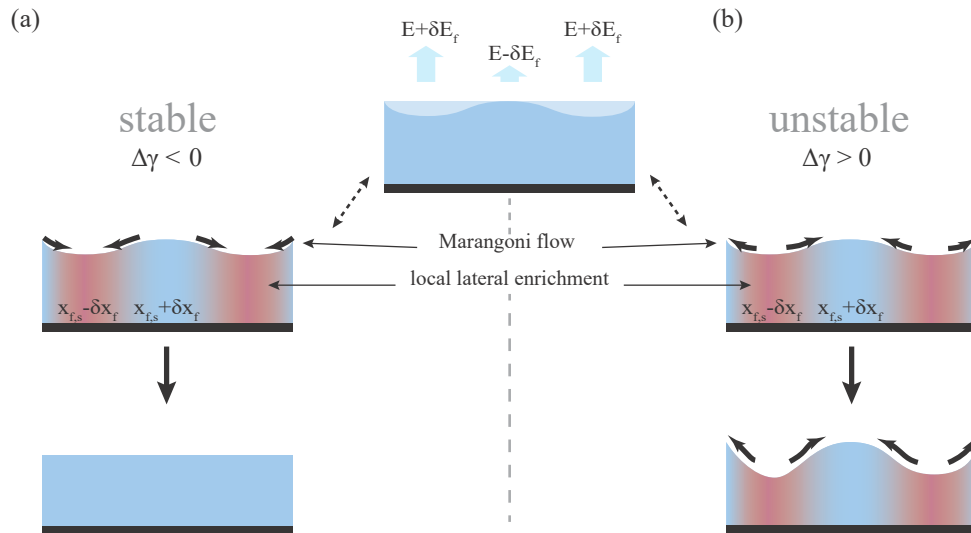


FIGURE 7.8: Proposed mechanism for the stabilization/destabilization of evaporative thinning films.

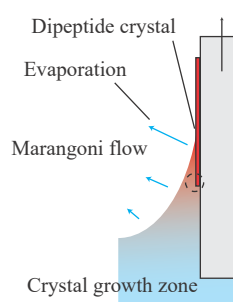
Figure 7.8 presents a possible mechanism for the destabilization of evaporative thinning films of binary mixtures of volatile components with different evaporation rates and surface tensions. It can be assumed that occasionally small local inhomogeneities in the local evaporation behaviour may occur. These will result in a small local enrichment of one component. If the result of this local enrichment is a surface tension gradient, it may cause a Marangoni flow. If this flow acts against the local enrichment both, the enrichment and thus the flow will disappear. The film remains stable. If the surface tension gradient leads to a Marangoni flow, which increases the local enrichment, this enrichment may get enhanced. In this case the film surface becomes wavy, undulated and eventually may even rupture. This mechanism explains at least qualitatively the main experimental findings. A more detailed analysis is currently in progress.

7.4 Conclusion

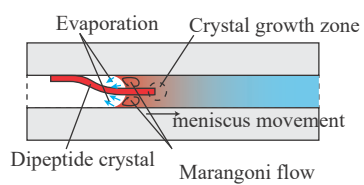
It is found that 1.) Films of binary mixtures of volatile liquids with a $\Delta\gamma < 0$ remain flat and stable during evaporative thinning. 2.) With $\Delta\gamma > 0$, the thinning films may or may not remain flat/stable. This depends on the composition x_0 . The ratio of the evaporation rates E_f/E_s also plays a role. 3.) For very small or big x_0 thinning films may remain stable, even if $\Delta\gamma > 0$. 4.) In the case of destabilizing films, the undulation wavelength λ depends on x_0 . λ decreases with decreasing x_0 . 5.) The appearance of undulations and their wavelength depends on time (and thus also on the film thickness). In general, λ decreases with time (with decreasing film thickness). 6.) A lateral Marangoni flow originating from small local fluctuations of the liquid composition as a result of a small fluctuation of the local evaporation may be the main cause of the film destabilisation.

Part III

**Partially wetting mixtures of
volatile and non volatile liquids:
Enrichment, crystal growth and
Marangoni flows near the three
phase line**



Self-assembly of ultralong aligned dipeptid single crystals



Directed self-assembly of dipeptide single crystal in a capillary

Chapter 8

Self-assembly of ultralong aligned dipeptid single crystals

Reprinted and adapted with permission from:

[159] Bingbing Sun, Qi Li, Hans Riegler, Stephan Eickelmann, Luru Dai, Yang Yang, Rodrigo Perez-Garcia, Yi Jia, Guoxiang Chen, Jinbo Fei, Krister Holmberg, and Junbai Li. "Self-Assembly of Ultralong Aligned Dipeptide Single Crystals". In: *ACS nano* 11.10 (2017), pp. 10489–10494. Copyright 2017 American Chemical Society.

S. Eickelmann build the experimental setup used for the dip casting (see Chapter 3.1.2), supervised and performed dip cast experiments in collaboration with *B. Sun* (leading to Figure 8.3, 8.9, and A.3), conducted the polarization measurements (shown in 8.7), and analyzed the solubility behavior (Fig. 8.8) together with *B. Sun*. *S. Eickelmann* developed the proposed mechanism together with *H. Riegler* depicted in Figure 8.10 and 8.11. *G. Chen* provided the SEM measurements (Fig. 8.5). *R. Perez-Gracia* conducted AFM measurements leading to Fig. 8.4. *B. Sun* wrote the first version of the manuscript and provided experimental data and results from a complementary approach. The study was designed and supervised by *H. Riegler* in collaboration with *J. Li*. The manuscript was then revised by *H. Riegler* and *J. Li*.

8.1 Abstract

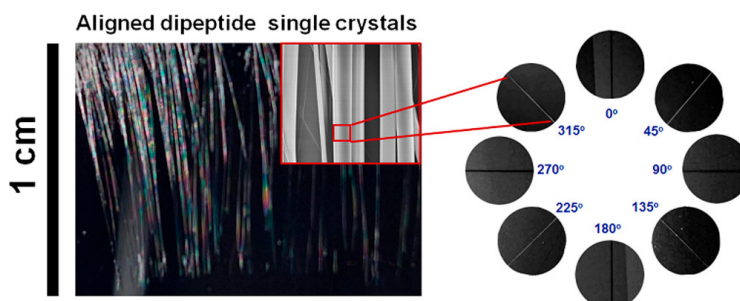


FIGURE 8.1: (left) white light microscopic image inset: SEM image (right) microscopic polarization images

Oriented arrangement of single crystals plays a key role in improving the performance of their functional devices. Herein we describe a method for the exceptionally

fast fabrication (mm/min) of ultralong aligned dipeptide single crystals (several centimeters). It combines an induced nucleation step with a continuous withdrawal of substrate, leading to specific evaporation/composition conditions at a three-phase contact line, which makes the growth process controllable. These aligned dipeptide fibers possess a uniform cross section with active optical waveguiding properties that can be used as waveguiding materials. The approach provides guidance for the controlled arrangement of organic single crystals, a family of materials with considerable potential applications in large-scale functional devices.

8.2 Introduction

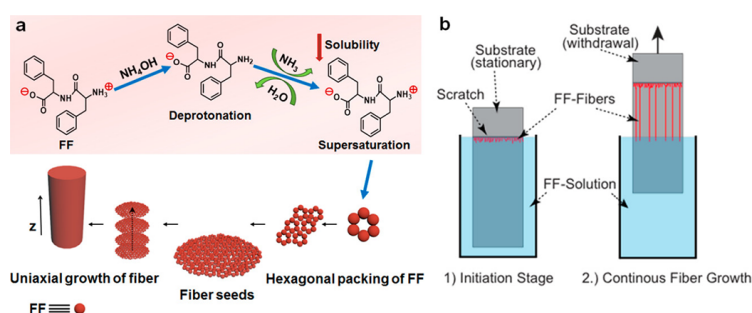


FIGURE 8.2: (a) Schematic of the self-assembly of FF crystals from molecules in NH_4OH solution. FF is negatively charged due to deprotonation of the ammonium group in NH_4OH solution. With the evaporation of solvent, the pH of the solution changes and the solubility of FF decreases, leading to supersaturation of FF in solution. Six dipeptide molecules constitute the circumference of a hydrophilic region and create each channel, which further spontaneously organize into fiber seeds. The seeds are uniaxially oriented along the longitudinal z axis and form fibers. (b) Schematic of the aligned growth of FF single crystals. The initiation stage (left plot) with the substrate stationary creates a band of fibers. In the following continuous fiber growth process (right plot), the substrate is withdrawn.

Formation of single crystals is ubiquitous in nature, and the crystals may be either organic or inorganic.[160–163] The crystallization processes are usually slow and extremely reproducible, endowing materials with a very high degree of precision.[164, 165] There are numerous examples of how highly organized crystalline structures form spontaneously.[166, 167] Especially, single crystals of organic materials have received widespread attention for extensive applications, due to their advantages over inorganic counterparts.[168] The oriented arrangement of organic single crystals is crucial in their applications.[169, 170] For instance, the patterning of organic single crystals is essential for high-performance large-area field-effect transistors.

Self-assembly of small building blocks is an attractive way to fabricate highly ordered architectural materials.[171–181] The intermolecular interactions are non-covalent, and the crystallization process usually occurs from a dilute solution of the building block, which is initiated by a specific nucleation process.[182, 183] One example of such a process is the crystallization of dipeptides.[184, 185] As a dipeptide building block, diphenylalanine (FF) has been widely reported, partly because the fibrous materials of FF are of interest as functional materials and for applications in the biomedical field, partly because networks of FF are associated with the

pathogenic process that leads to Alzheimer's disease.[186] FF single crystals possess several properties that might be used as optical waveguiding or semiconducting materials.[187, 188] At present, aligned FF nanotubes can be fabricated by a vapor deposition approach.[189] However, because of the strong self-organizing tendency of the deposited materials, the production of a highly controllable arrangement of FF single crystals still faces many challenges, which surely limit their applications.

Here, we describe a procedure for the fast growth of ultralong aligned FF single crystals (Figure 8.2). A binary solvent system is introduced in the self-assembly process. The evaporation/composition of solution conditions lead to controllable nucleation, and a substrate withdrawal system allows the continuously oriented growth of uniform single crystals. This up-scaling of the procedure is controllable, reproducible, and relatively straightforward, which might be scaled up into an industrial process for large-scale devices of organic single crystals.

8.3 Results and discussion

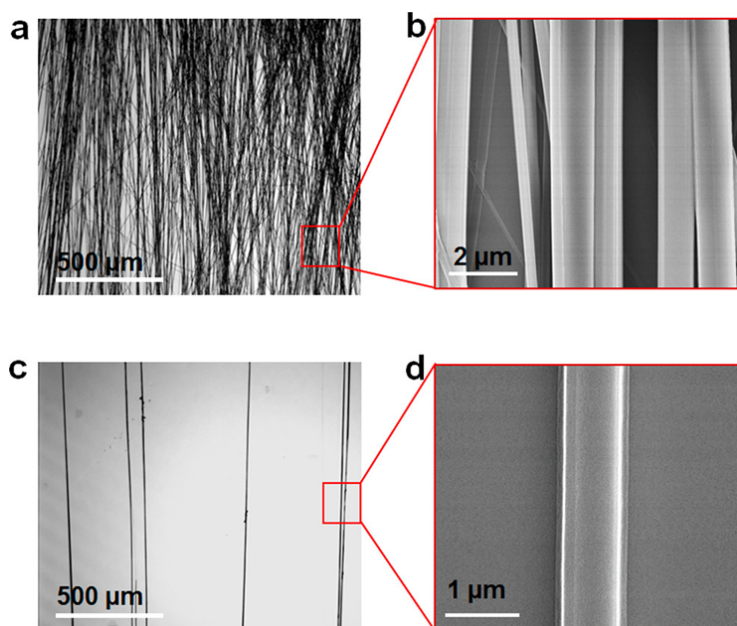


FIGURE 8.3: FF single crystals formed at different withdrawal speeds. (a), Bright field image and (b) SEM image of FF single crystals at a low withdrawal speed of 2.0 $\mu\text{m}/\text{sec}$. (c) Bright field image and (d) SEM image of FF single crystals at a low withdrawal speed of 4.6 $\mu\text{m}/\text{sec}$. $c_0 = 0.026 \text{ mol/L}$, 0.059 mol/L NH_4OH , 38 $^\circ\text{C}$.

As shown in Figure 8.3, a horizontally aligned array of FF crystals was fabricated. These aligned crystals with different structures can be obtained by our controlled fabrication approach. A large number of crystals (Figure 8.3a,c) and fewer individual crystals were formed on the substrate (Figure 8.3b,d).

In Figure 8.4a, it can be observed that the obtained FF fibers are ultralong and can grow up to several centimeters. The SEM images show that aligned FF fibers are approximately 1.5 μm in width with cross sections typically in the range of a few hundred nm to a few μm (Figure 8.3 and Figure 8.5). They are not strongly

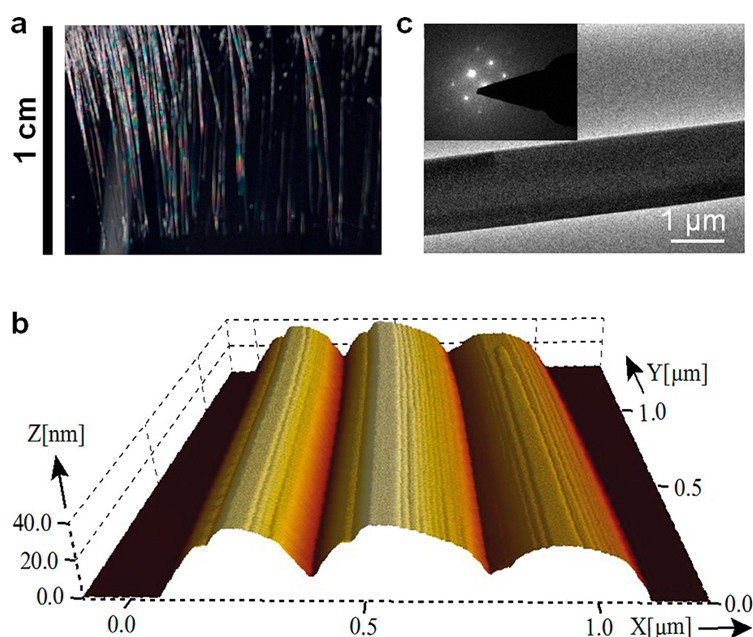


FIGURE 8.4: Characterization of the FF fibers. (a) Image of FF single crystals on a silicon wafer. (b) 3D-AFM image of FF single crystals deposited on a silica surface. The step heights of the terraces are 2 – 3 nm. (c) SAED pattern of a FF single crystal.

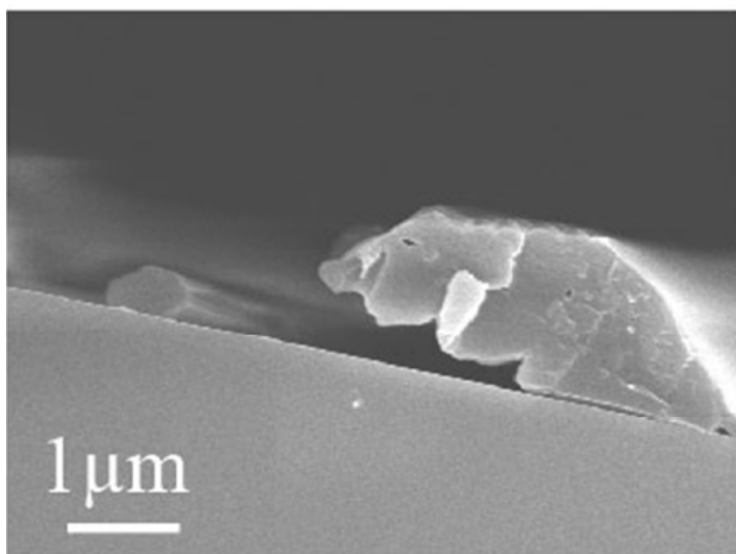


FIGURE 8.5: SEM image of a broken end of FF fibers.

attached to the substrate surface, inferring that the fibers should be deposited onto the substrate after growth (Movie S1). The 3D-AFM image shows that the composed fiber is about 1 μm wide and only at most 40 nm high, which is consistent with the cross sections observed by SEM (Figure 8.4b). The image also reveals the surface of the fibers is smooth down to the nm scale with a pronounced terrace topology, with a height of the terrace steps of about 2 – 3 nm. The regular spot pattern of a representative single FF fiber in the SAED pattern indicates that the fiber possesses a single-crystal structure (Figure 8.4c). The XRD and FTIR analyses, depicted in Figure

8.6, confirm the highly crystalline structure and β -sheet secondary structure of the FF fibers. The fiber is also illuminated with linearly polarized light and imaged

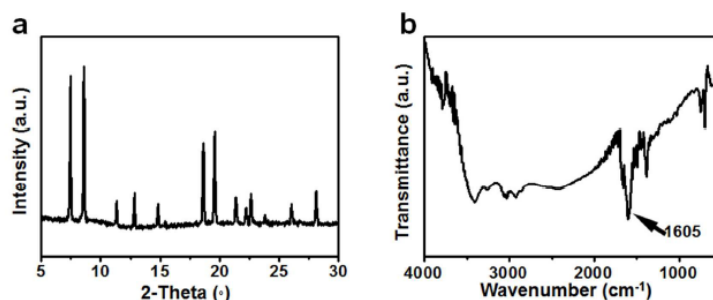


FIGURE 8.6: a) XRD and b) FTIR of powder of FF fibers.

in reflection with an analyzer rotated at 90 deg. Rotation around the optical axis

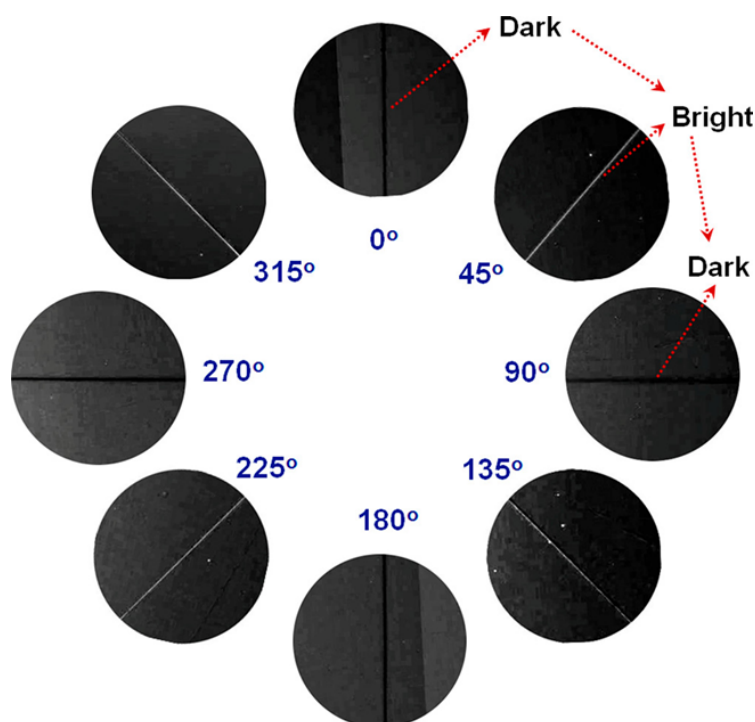


FIGURE 8.7: FF single crystal imaged in reflection with crossed polarizers. Consecutive frames are rotated around the microscopy axis in steps of 46 deg as indicated in the frames.

reveals four bright/extinction positions, rotated at 90 deg to each other (Figure 8.7), indicating FF molecules are uniaxially oriented along their long axis in the fiber, leading to strong anisotropy of the refractive index. To achieve the controlled formation of aligned FF single crystals, two stages of a so-called “free-meniscus coating” process, a vertical withdrawal of a planar solid substrate from a solution, are applied (Figure 8.2).[190] In the first stage (“initiation stage”), we provide the silicon wafer with a long horizontal scratch to overcome the nucleation barrier to initiate the crystallization at a certain substrate location (left plot in Figure 8.2b).[191] The silicon wafer is submerged into the FF solution and kept stationary to let the

scratch in close proximity to the three-phase contact line and in contact with the solution. As the solvent evaporates, the FF concentration will eventually exceed its solubility limit and induce nucleation on the scratch in the vicinity of the three-phase contact line. Some small FF fibers will start to grow from the region of the scratch preferentially in the direction toward the bulk liquid reservoir. In the second process stage, the substrate is withdrawn continuously at constant velocity (right plot in Figure 8.2b). A few fibers out of the rather large number that have grown in the initiation step would serve as “seeds” for further growth.[192] Subsequently, ultralong aligned FF fibers would form on the silicon wafer and grow linearly with the withdrawal of the substrate (Movie A.3 in the Appendix A.3).

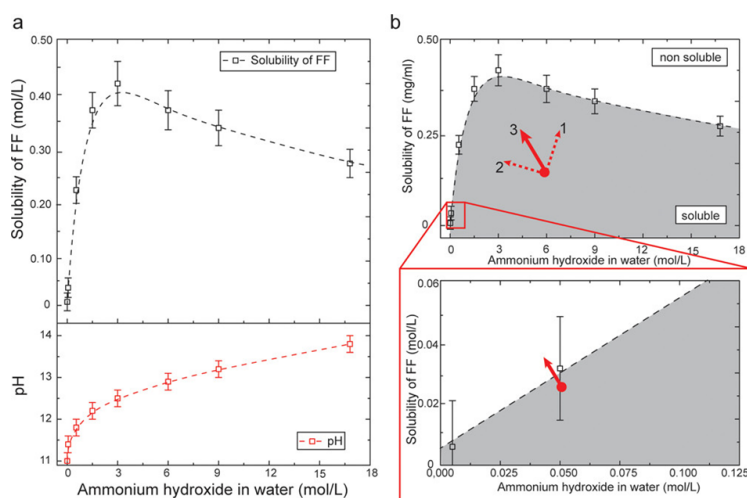


FIGURE 8.8: Induced fast growth of aligned FF single crystals. (a) Solubility of FF (upper plot) and pH (lower plot) as a function of concentration of NH_4OH . (b) Change of concentration of FF (c_{FF}) in the NH_4OH solution as NH_3 and H_2O evaporate.

A special solvent system was introduced in this self-assembly process, making the system controllable. FF possesses one terminal amino group and one terminal carboxyl group (Figure 8.2a). It forms an inner salt around its isoelectric point ($pI = 5.3$), where its solubility is very low. The solubility can be greatly enhanced in either acidic or basic environment. We use ammonium hydroxide (NH_4OH), an alkaline environment, to vary the charge and thus the solubility of FF. Figure 8.8a shows the solubility of FF in NH_4OH with different concentrations of ammonia (the curve is the critical concentration of FF). The solubility increases steeply with increasing hydroxide concentration up to 2.89 mol/L ($pH \approx 12.4$), as a result of increasing degree of deprotonation of the ammonium group. Then it reaches a peak at about 2.89 mol/L NH_4OH because of the fully charged of FF and decreases with increasing concentration of NH_4OH , due to the common salt effect.

As a binary solvent system, H_2O and NH_3 are volatile compounds in NH_4OH solution, determining the solvent condition for the FF as a nonvolatile compound. As displayed in Figure 8.8b, we suppose if only H_2O evaporates from solution, both the concentration of FF (c_{FF}) and the pH would increase (arrow 1). If only NH_3 evaporates, the c_{FF} would be approximately constant and the pH would decrease (arrow 2). Indeed, with both H_2O and NH_3 evaporating, the net effect will be that the pH decreases and c_{FF} increases (arrow 3), while the change of FF solubility mainly

depends on the initial pH of solution (the initial NH_4OH concentration). With high NH_4OH concentration, the solubility would increase first and then decrease with the evaporation of the solvent, while when the NH_4OH concentration is lower than 2.89 mol/L, the solubility of FF decreases in the whole evaporation process, which is conducive to the supersaturation of FF (Figure 8.2a). When the solution is supersaturated, six FF molecules constitute the circumference of a hydrophilic region and create each channel, which further spontaneously organize into FF fiber seeds. The seeds would be uniaxially oriented along the longitudinal axis and form FF fibers.^{37,38} To facilitate the nucleation for crystals, we select a low initial NH_4OH concentration (0.059 mol/L), around the “linear part”, and a c_{FF} (2.89 g/L) a little below the solubility limit (Figure 8.8b) for the experiments.

The structure of these growing fibers (separation, thickness, orientation, etc.) can be controlled by the process parameters of the second stage (such as the concentration of initial NH_4OH and temperature) (Figure A.2), which is discussed in the Supporting Information. Interestingly, the structures of aligned FF fibers on a substrate can also be controlled precisely by the withdrawal speed of the substrate (Figure 8.3). After nucleation, the fibers grow with a constant withdrawal speed in the withdrawal direction and with constant thickness (Figure 8.3a,b). Even with the rather crude control of the process parameters applied in our test setup, very long and individual fiber crystals can be grown. When we increase the withdrawal speed, fewer individual fibers form on the substrate (Figure 8.3c,d). This might be attributed to the difference between the withdrawal speed of the substrate and the enrichment rate of FF. When the withdrawal speed is faster, the enrichment of FF at the growth zone can not support enough required molecules for further growth for all crystal seeds; as a result, fewer fibers grow continuously. Furthermore, at sufficiently high withdrawal speed, the continuous growth of long fibers will cease completely, which is attributed to the crystallization and liquid drainage process becoming unstable; that is, regimes of rapid crystallization and movement of the three-phase line alternate with regimes of barely any fiber crystallization.

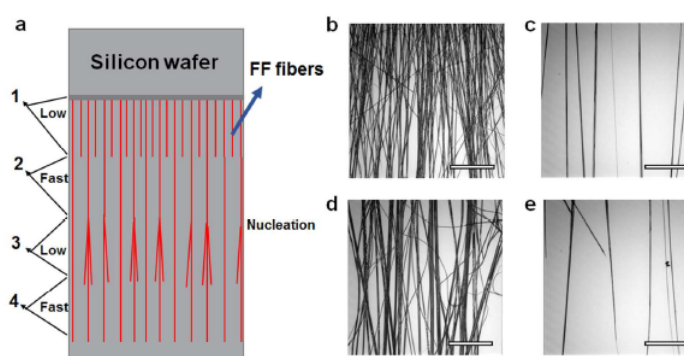


FIGURE 8.9: The “gradient single crystals” at a silicon wafer (positions 1,2,3,4) obtained by four steps with different withdrawal speeds. a) The schematic of the formation. The withdrawal speed at step 1,2,3,4 is b) 2.0 $\mu\text{m}/\text{sec}$, c) 4.6 $\mu\text{m}/\text{sec}$, d) 2.0 $\mu\text{m}/\text{sec}$, e) 4.6 $\mu\text{m}/\text{sec}$, respectively. The scale bar is 100 μm .

Based on this principle, the “gradient-aligned single crystals”, which possess “more-less-more-less” numbers of aligned fibers on different positions of one substrate, can be achieved by just varying the withdrawal speed during the growth

process (Figure 8.9). When the silicon wafer was initially withdrawn at a low speed (step 1 shown in Figure 8.9), the FF solution was supersaturated. As the withdrawal speed was increased (step 2), fewer single crystals grow at the silicon wafer. When the withdrawal speed was reduced (step 3), more molecules in this supersaturated solution would be deposited in this region to create new crystal nuclei. As a consequence, the number of FF fibers increases again in this area without a horizontal scratch. When the withdrawal speed was increased again (step 4), fewer fibers formed. Such a precisely controllable arrangement of ultralong single crystals by this method makes it promising in the fabrication of large arrays of high-performance devices for further applications.[169]

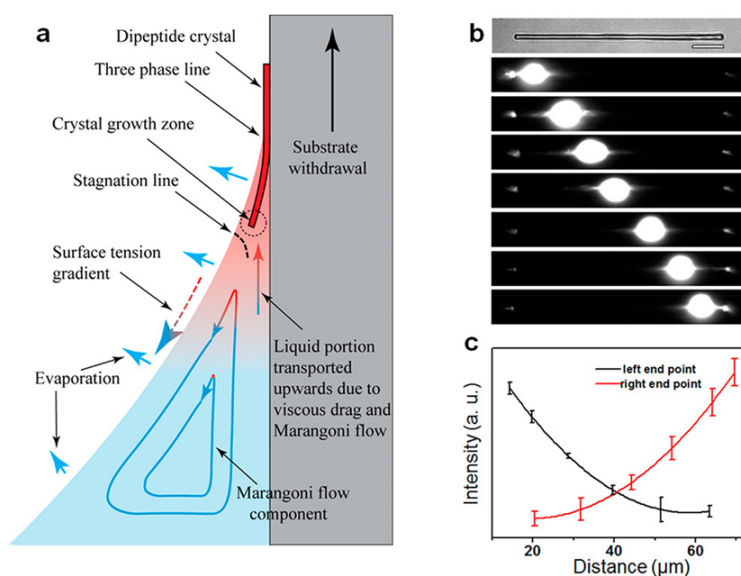


FIGURE 8.10: Proposed mechanism and optical waveguide properties of aligned FF single crystals. (a) Proposed mechanism of aligned FF single crystals. Enrichment of FF at the end of the meniscus due to evaporation of water leads to a surface tension gradient. This gradient induces a Marangoni flow. (b) Field image and PL images of a single FF-RhB fiber when the excitation spot was translated along the fiber. The excitation wavenumber is 488 nm; scale bar, 10 μm . (c) Excitation distance-dependent PL intensity at each end point; the distance denotes the length between left end point and excitation spot.

Based on the above results, the growth scenario and the underlying mechanisms regarding flows and component distribution are proposed and depicted in Figure 8.10a. Because of the singularity of the diffusion-controlled evaporation (environment: ambient air) in this region, the evaporation is strongest in the vicinity of the three-phase line (the contact angle is about 10°).[193] The closer the location to the three-phase line, the higher the FF concentration (H_2O evaporation) and the lower its solubility (NH_3 evaporation). In the case of a stationary substrate, these gradients will increase with time due to the ongoing evaporation. The local change in pH and FF concentration due to the local evaporation will to some degree, but not completely, be balanced by diffusive transport of FF and protons toward the bulk liquid reservoir. Eventually, the FF concentration will sufficiently exceed the saturation limit to start nucleation at the scratch and subsequent growth of FF crystals (Figure 8.11).

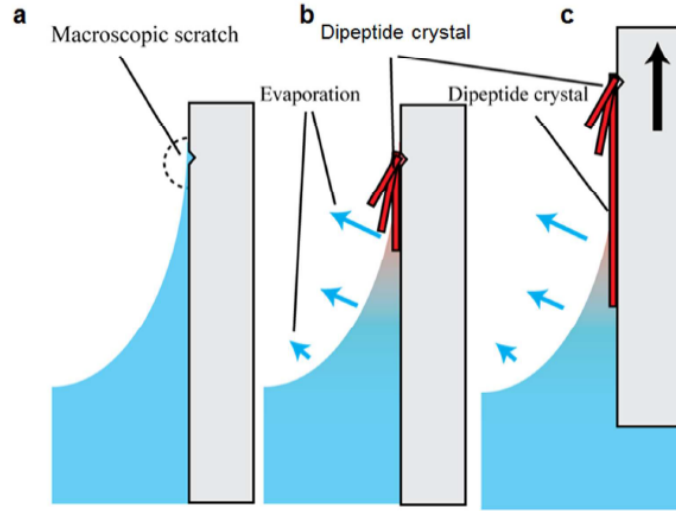


FIGURE 8.11: Schematic of proposed assembly mechanism of the aligned FF single crystal growth process. a) Macroscopic scratch provides a nucleation side. b) FF fibers (coffee-stain) act as “crystal seed”. c) Dip-coating starts to withdraw FF fibers.

When the substrate is withdrawn, the drainage of the liquid from the meniscus, the evaporation, and the incorporation of the solubilized FF into the growing crystals will establish a quasi-stationary concentration profile, which favors the growth in the liquid phase in the vicinity of the three-phase line. The growth direction will preferentially be normal to the three-phase contact line, toward the bulk solution bath. The substrate is much wider than the capillary length; thus, edge effects at the substrate ends can be neglected to a first approximation.

As discussed above, the number of fibers per area can be controlled by the withdrawal speed. Faster speed means a lower number of fibers. At first, a simplified scenario is applied as a first approximation, ignoring the impact of the local FF enrichment on the hydrodynamics and on the evaporation rates. It is assumed that the amount of deposited FF (the number of fibers per area) is determined by the net amount of solution, which is continuously taken out of the bulk reservoir and evaporating during the course of the substrate withdrawal, leaving behind dry FF. The withdrawal of the substrate leads to a viscous boundary layer, which is divided at a stagnation line. The liquid section close to the substrate is on its way to be deposited on the substrate, and the liquid flowing on the opposite side of the stagnation line returns to the bath. For low capillary numbers (our case) the thickness H of the deposited film is

$$H \approx \frac{(\mu v)^{2/3} (\rho g)^{1/2}}{\gamma^{1/6}} \quad (8.1)$$

with μ being dynamic viscosity, ρ liquid density, γ surface tension, g the gravitational constant, and v withdrawal speed.[194] According to this approach H should increase with speed ($v^{2/3}$). Hence, the amount of deposited liquid solution and the number of crystals per area should increase with the increased withdrawal speed.

However, we observe the opposite: that higher withdrawal speed leads to fewer crystals per area. So, an additional process, modifying the proton and FF concentration profiles in the vicinity of the three-phase line, is taken into account. The

contribution is proposed to be a Marangoni flow, which can be caused by the local enrichment of FF close to the three-phase line as a result of water evaporation.[132] With the substrate moving upward at constant speed, the system will establish a stationary state in the frame of the three-phase line and the substrate coordinates after a transient time. There will be a certain stationary profile of the pH and FF concentrations as well as a stationary flow profile. The flow profile consists of a Marangoni component and a component originating from viscous drag balanced by gravitation. Both components induce a downward flow close to the liquid/air interface and an upward flow close to the substrate surface, i.e., effectively a convective transport of “fresh” solution from the bath into the meniscus region, where the insoluble component is enriched due to the solvent evaporation. The viscous flow depends mainly on the withdrawal speed. It is independent of the local composition of the solution, but has an influence on the composition through the convective transport. On the other hand, the Marangoni depends mainly on the local composition of the solution. There may well be a feedback between all these contributions such that upon increasing the withdrawal speed the amount of solute that finally is deposited after solvent evaporation is decreasing with increasing withdrawal speed, as it is observed experimentally.

These FF single crystals were confirmed to possess active optical waveguiding properties. Rhodamine B (RhB) was doped into the self-assembly of the FF fibers. The XRD pattern after doping implies that the addition of RhB does not change the molecular arrangement of the FF fibers (Figure 8.12). As shown in Figure 8.10b, when

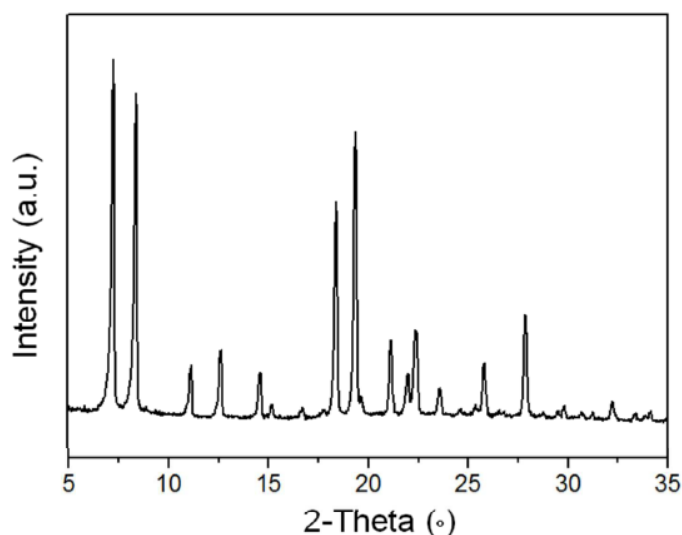


FIGURE 8.12: XRD pattern of the FF-RhB fibers. 0.006 mol/L NH_4OH at 38 °C, withdrawal speed, 2 $\mu\text{m}/\text{sec}$.

the excitation light is focused on the body of the fiber, bright photoluminescence (PL) spots are obtained at both ends, with the body emitting nearly no PL. The outcoupling of light at the end is a typical waveguide behavior. In Figure 8.10c, the distance-dependent PL intensity at each end of the FF-RhB fiber shows that the light of the out-coupled spot decreases almost exponentially with the increase in propagation distance with an attenuation length of about 40 μm , confirming the FF fiber can act as an optical waveguiding material for further applications.[195]

8.4 Conclusion

In conclusion, we have developed a controllable approach for the aligned arrangement of dipeptide single crystals. The induced nucleation and a substrate withdrawal system allow the continuously oriented growth of uniform size crystals from solution with a technically unlimited length. Structures of growing crystals can be controlled by the process parameters. These aligned ultralong single crystals with active optical waveguiding property might have a bright prospect in optical applications, and these findings will be useful for the controlled arrangement of aligned materials, which are essential for largescale functional devices.

Chapter 9

Directed self-assembly of dipeptide single crystal in a capillary

Reprinted and adapted with permission from: [196] Bingbing Sun, Hans Riegler, Luru Dai, Stephan Eickelmann, Yue Li, Guangle Li, Yang Yang, Qi Li, Meifang Fu, Jinbo Fei, and Junbai Li. "Directed Self-Assembly of Dipeptide Single Crystal in A Capillary". In: *ACS nano* (2018). Copyright 2018 American Chemical Society.

B. Sun conducted the experiments wrote the first version of the manuscript. *S. Eickelmann* conducted and analyzed some experiments providing Figure 9.2 and A.5. The study was designed and supervised by *J. Li*. The manuscript was revised by *H. Riegler* and *J. Li*. All authors discussed the results and commented on the manuscript.

9.1 Abstract

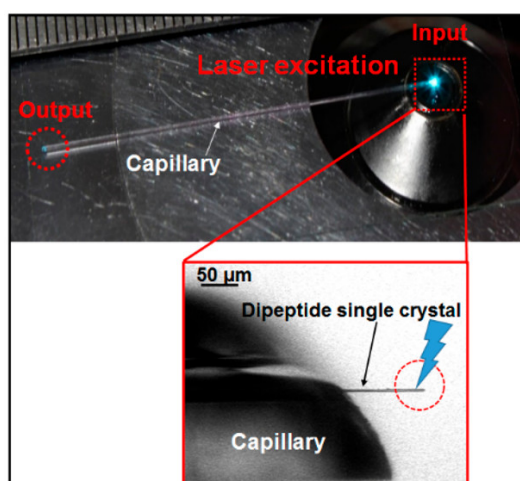


FIGURE 9.1: Photograph of a single FF crystal waveguide eigenschaften bla bla

Controlled growth of one-dimensional nanostructures is playing a key role in creating types of materials for functional devices. Here, we report procedures for

controlled assembly of the dipeptide diphenylalanine (FF) into aligned and ultralong single crystals in a capillary. With the evaporation of solvent, nucleation of the crystal occurred in the confined region, and the crystal grew continuously with a supply of molecules from the concentration gradient system inside the capillary. Based on the “Knudsen regime”, an ultralong aligned individual FF single crystal possessing an active optical waveguide property at macroscopic length scale could be obtained. Moreover, capillary is also an effective microdevice to investigate the disassembly process of the FF single crystals. This strategy has potentials to broaden the range of applications of aligned organic nanomaterials.

9.2 Introduction

One-dimensional (1D) micro- and nanostructures of organic materials have attracted extensive attention due to their promising applications in high-performance functional devices.[197–200] This is especially true for 1D organic single-crystal nanomaterials because they have no defects, which is essential for the manufacture of this type of advanced material.[160, 161, 201, 202] Controlling the growth and assembly of organic single crystals is important for improving and optimizing the performance of functional devices.

Self-assembled organic crystalline nanomaterials are flexible building blocks employable in functional optical and electronic nanoscale circuits.[203–206] Much attention has been directed toward diphenylalanine (FF), a dipeptide which is the core recognition motif of the Alzheimer’s β -amyloid polypeptide.[186, 188, 207] FF is attractive as a molecular building block because of its biocompatibility, biodegradability, and functional flexibility.[208–210] Different routes have been published for fabrication of FF single crystals. Our group has obtained the FF single-crystalline dipeptide structure by introducing an aldehyde into the fibrous networks.[195]

As a small molecule with two aromatic rings, FF easily self-assembles to single-crystal nanostructures either from solution or by vapor deposition methods. However, these crystals generally have a disordered manner, giving macroscopic assemblies with random position and orientation.[166, 211] Such an uncontrolled self-assembly process limits the usefulness of the FF single crystals because many applications require unidirectional single crystals. Recently, a time-programmed control of the self-assembly and subsequent growth of nanostructures has been developed.[212, 213] The crystal growth mechanism consists of three steps: nucleation, adsorption, and diffusion and growth.[214] Both thermodynamic and kinetic factors have been found to be essential in the self-assembly process.[215–217] Based on this mechanism, we propose that a confined nucleation and a continuous supply of molecules are prerequisites for a controlled fabrication of FF single crystals.

In this work, we report a method for a controlled directed growth of ultralong FF single crystals in capillaries (Figure 9.2). Capillaries have been used to control evaporation of nanotube aqueous dispersion to prepare a patterned surface.[218] We used a capillary to provide a confined space, controlling the growth direction of the single crystals. The evaporation of solvent from capillary gives the concentration gradient of FF that is required to limit the number of nucleation sites. The loss of

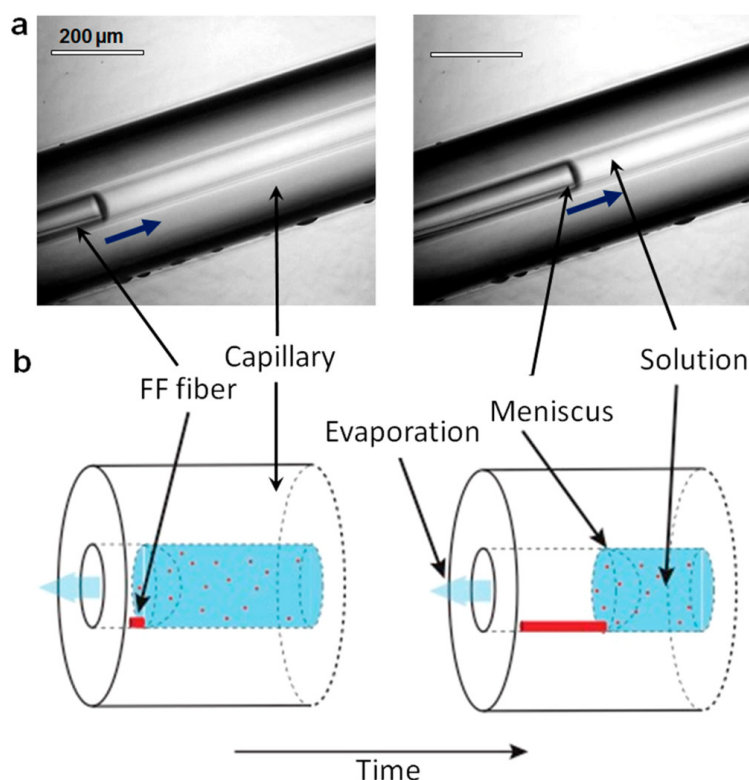


FIGURE 9.2: Growth of an individual FF fiber inside a capillary starts within a few minutes after the beginning of the evaporation at room temperature. (a) Bright-field images of a single FF fiber at different times. The inner diameter of the capillary is 50 μm . (b) Schematic of the FF fiber growth process in a capillary.

solvent triggers the growth of the FF crystals inside the capillary, resulting in a theoretically unlimited length of the single crystal.

9.3 Results and Discussion

FF was dissolved in a mixture of HFP (1,1,1,3,3,3-hexafluor-2-propanol) and water, and this solution was soaked into a capillary by capillary pressure. Then, one end of the capillary was sealed and the other end kept open. Bright-field microscopy images of this process at two different times are shown in Figure 9.2, together with a schematic of the process. As the solvent evaporates, the meniscus recedes further into the capillary. At one point, FF crystals start to form inside the capillary. With the continuous evaporation of the solvent, a long FF fiber is generated (Movie A.5 in the Appendix A.4). The crystallization of FF was significantly influenced by the diameter of the capillary. Figure 9.3c,f,i shows that only one individual FF microwire was formed inside a capillary with an inner diameter of 50 μm . For a capillary with an inner diameter of 100 μm , several microwires were obtained (Figure 9.3b,e,h). For the 200 μm capillary, the number of microwires was even larger (Figure 9.3a,d,g). The SEM images reveal that the microwires have a kind of trapezoid cross-sectional shape with lateral dimensions of about 5 μm , corresponding to cross-sectional areas of about 20 μm^2 (Figure 9.3d–f). The uniform brightness in the polarized optical

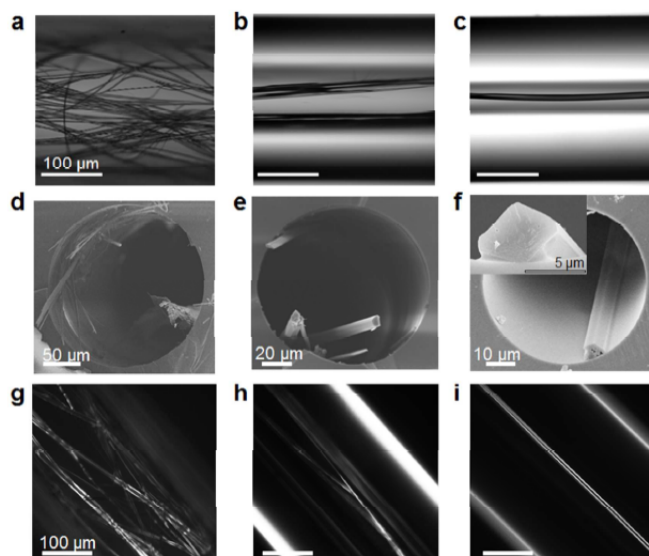


FIGURE 9.3: Morphological characterization of FF single crystals inside capillaries with different inner diameter. Capillary with a diameter of a,d,g) 200 μm ; b,e,h) 100 μm , and c,f,i) 50 μm . Upper row: optical microscopy images ; middle row: SEM; lower row: polarized microscopy.

microscopy (Figure 9.3g–i) indicates that the single fiber in the case of the smallest capillary (inner diameter of 50 μm) is a single crystal. The microwire bundles that form in the case of the capillaries with larger diameters seem to consist of sections of single crystals.

The following scenario is proposed for formation of FF fibers in capillaries with different diameters. It is assumed that the density of the dipeptide is approximately the same as that of the solution in weight (c_0 , in relative volume content of FF per solvent volume). With a single fiber with a fixed cross section of a_f , material conservation for each capillary cross section, a_c , all the FF in solution per capillary inner diameter, $c_0 \cdot a_c$, becomes crystalline with a total FF crystal cross section of $a_f \cdot n$, with n being the number of fibers:

$$c_0 \cdot a_c = a_f \cdot n, \text{ or } n = \frac{c_0 \cdot a_c}{a_f} \quad (9.1)$$

Based on this scenario, when c_0 is constant, n mainly depends on the cross section of the capillary. If only one fiber forms inside a capillary of 50 μm inner diameter, the number of fibers formed inside capillaries of 100 and 200 μm inner diameter should be 4 and 16, respectively. The number of fibers seen in Figure 9.3 corresponds closely to these theoretical values, demonstrating that the number of fibers obtained with our procedure is controllable.

The obtained FF fiber was analyzed with X-ray diffraction (XRD) to investigate the crystal pattern. Figure 9.4a shows the results of three different positions on the FF fiber formed inside a long capillary (Figure 9.5). These three XRD patterns are similar and show hexagonal structures, as has been determined for FF single crystals. The results indicate that the degree of crystallinity is high and uniform along the long FF

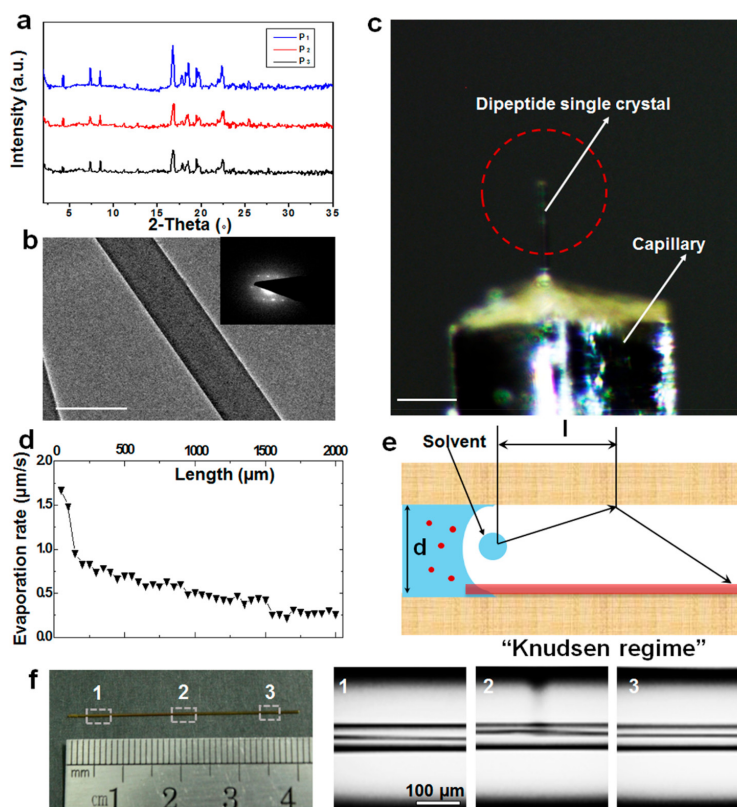


FIGURE 9.4: Characterization of the FF single crystals and the growth process. (a) XRD patterns at three positions (P1, P2, P3) of a FF single crystal residing inside a long capillary. The three positions are shown in Figure S1. (b) Electron diffraction pattern of a FF single crystal. The scale bar is 1 μm . (c) Analysis of the FF fiber by single-crystal X-ray diffractometry. The red circle shows the region at which the X-ray focused. The scale bar is 100 μm . (d) Evaporation rate of solvent vs length of the capillary. (e) "Knudsen regime" in capillary. (f) Ultralong FF single crystal in a capillary. Rectangles 1, 2, and 3 represent three positions on the capillary, and optical images are shown at these positions. The vapor pressure is 85 kPa

fiber.[187] The FFF fiber was also investigated by single-crystal X-ray diffractometry.

As shown in Figure 9.4c, the X-ray was focused on the fiber and not on the whole capillary to avoid interference from the capillary walls. The experimental conditions and the structural XRD parameters are shown in Table S1. The experiment confirmed a hexagonal lattice of the FF single crystal.[219] Selected area electron diffraction pattern (Figure 9.4b, inset) also suggests a single-crystalline structure of the FF fiber.

Movie A.5 shows the growth of the FF fibers in the smallest capillary (50 μm) at different times. At the beginning, the meniscus inside capillary recedes rather fast ($> 1 \mu\text{m}/\text{sec}$). The generated FF fiber remains as a deposit at the dry capillary side wall, while the meniscus recedes. At this early stage, no growth of the FF fiber within the solution can be detected within the resolution of the microscope (μm). At later stages, the meniscus recedes much slower than in the beginning due to the reduced evaporation rate. Then the FF fiber grows in the solution at some distance ($> 100 \mu\text{m}$) "ahead" of the meniscus.

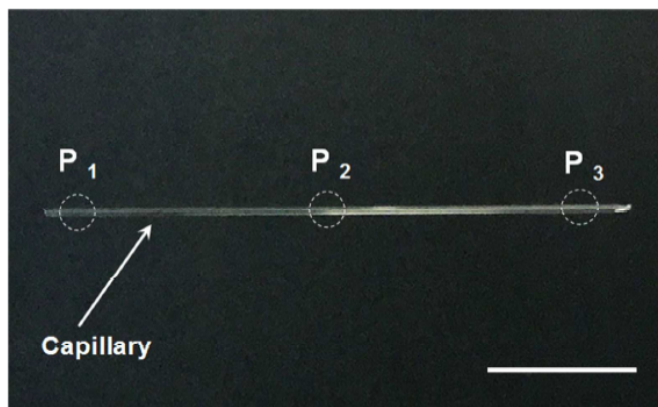


FIGURE 9.5: Three positions (P1, P2, P3) on a capillary measured by XRD. The diameter of the capillary is 50 μm . The scale bar is 1 cm.

We assume a typical nucleation and growth scenario for this system. The fiber starts to grow when FF concentration exceeds the (equilibrium) saturation concentration. The growth rate and direction are determined by the supply of FF from the surrounding solution. We neglect that the evaporation and solubility properties of the solution depend on the solvent composition (i.e., on the relative amounts of water and HFP). It is simply assumed that the evaporation drives the concentration of FF closer to the saturation limit. We also neglect gravity effects (the bond number $\ll 1$) and convective flows (Marangoni flows) due to the locally changing composition of the solvent.[132] Then the only transport mechanism for FF in solution is diffusion. Typically, the diffusion-controlled evaporation rate will dominate when the meniscus has receded further than the diameter of the capillary. The evaporation process driven by diffusion is quasistatic.

If the solvent vapor behaves as an ideal gas, the length of the dry capillary (distance to the opening), x , increases with time, t , according to $x \propto t^{0.5}$. The speed at which the meniscus recedes, v , decreases continuously as $v \propto t^{-0.5}$. Because the initial concentration of FF is substantially lower than the concentration at supersaturation (which is required for the nucleation of FF crystals), the crystallization and growth of the fiber occur when the solvent evaporation is diffusion-limited. With the meniscus continuously receding in the capillary, the evaporation rate of the solvent decreases (Figure 9.4d). This leads to a slower increase of the length of the FF fiber (Figure 9.5). Higher temperatures (60 and 100 $^{\circ}\text{C}$) were tried to increase the evaporation speed. However, continuous fibers were then not obtained (Figure 9.7). The solvent evaporation rate can also be increased through a transition from diffusion-controlled evaporation to the “Knudsen regime” when the meniscus is deeper inside the capillary.[220, 221] In this situation, the mean free path (l) is the average distance traveled by a moving particle between successive collisions. When gas molecules diffuse through capillary pores with a diameter (d) smaller than the mean free path of the diffusing gas molecule and when the density of the gas is low, the gas molecules collide with the pore walls more frequently than with each other. In the Knudsen diffusion regime, the molecules move in straight lines between points on the pore channel surface. This phenomenon would favor evaporation of solvent vapor from a capillary (Figure 9.4e). A longer mean free path can be achieved by lowering the

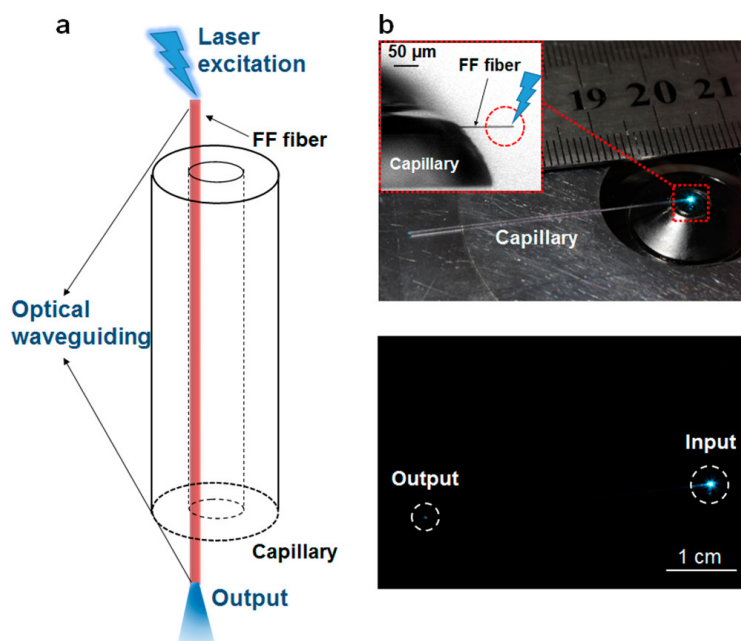


FIGURE 9.6: Optical waveguiding of the ultralong FF single crystal inside a capillary. (a) Schematic of the optical waveguiding. A laser microscope provides an exciting light for the RhB-doped FF single crystal. (b) Optical field image of the excited end of the FF single crystal. The circle represents the region of exciting light with a wavelength of 488 nm. Pictures of the capillary were taken in white light and in the dark.

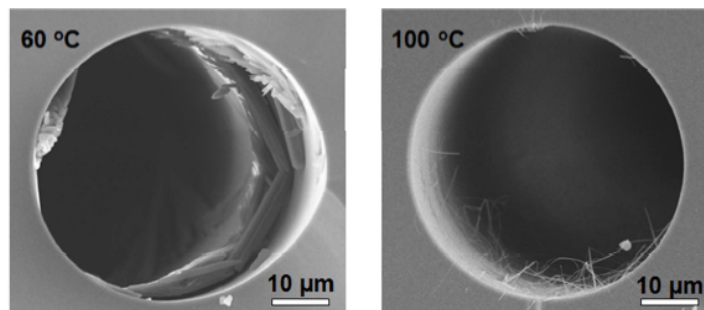


FIGURE 9.7: SEM images of a FF fiber inside a capillary at 60 °C and 100 °C. The inner diameter of the capillary is 50 μm.

vapor pressure.[222] We performed the crystal growth experiments in a low vapor pressure environment, and one ultralong FF fiber formed inside the capillary (Figure 9.4f). The length of the FF fiber was up to 4 cm. The polarizing microscope images of three parts of the fiber in the capillary showed a uniformly aligned single-crystalline structure of the fiber (Figure 9.8).

The optical waveguiding properties of the ultralong FF single crystal were confirmed by a confocal laser scanning microscopy. The self-assembly of the dipeptide was doped with a dye Rhodamine B (RhB), giving the fiber outstanding photonic properties. Two ends of the capillary were broken, allowing release of the fiber from capillary (Figure 9.6a). As noted in Figure 9.6a,b, when one end of the fiber was excited by a laser (488 nm), a weak light was observed at the other end of the fiber. This outcoupling effect is typical for waveguiding, indicating that the FF fiber allows

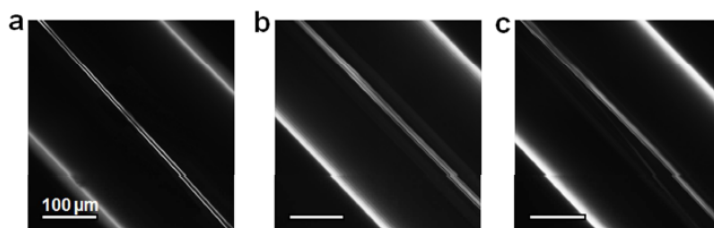


FIGURE 9.8: Polarized microscopy images of the ultralong FF single crystal at three positions of the capillary, a-c). The three positions on the capillary are shown in Figure 9.4f.

for propagation of light emission along the long axis.[159, 223] It is noteworthy that the FF fiber is very long, up to several centimeters (4 cm). This microscale dipeptide single crystal is proved to have the optical waveguiding properties at a macroscopic length scale, indicating that the long single crystal can be used as an optical fiber.

It has been reported that FF is the core molecular recognition motif of β -amyloid polypeptide and the smallest unit that undergoes self-assembly into ordered structures.[187, 209, 224] FF fibers are similar to native amyloids with respect to the assembly mechanism as well as to the chemical, physical, and biological characteristics. The disassembly of FF fibers could be considered as a model for inhibition of the amyloid systems. We investigated the disassembly of the FF single crystal inside the capillary by adding a solvent. An optical microscope was used to visualize the apex of the crystal inside the capillary in real time. A HFP/water (5 : 1, v/v) solution was injected into the capillary, and the two ends of the capillary were then sealed. The disassembly process started at around 3 min after injection of the solvent into the capillary. As shown in Figure 9.9, the shape of the apex became sharper and narrower and the crystal length decreased, indicating that the disassembly of the structure starts from the apex of the crystal and progresses toward its body (as shown in Figure 9.10 and Movie A.6(in the Appendix A.4)). The crystal disappeared within 2 min.

9.4 Conclusion

In conclusion, the directed self-assembly of FF single crystals was well-controlled in capillaries. Ultralong individual FF single crystals could be obtained under the provided conditions such as capillary diameter, solvent composition, and solvent evaporation rate. The number of crystals formed in one capillary and the evaporation of the solvent in the capillary proceeded theoretically, which makes the formation of crystals controllable. The possibility to prepare very long single crystals of FF implies that the procedure is of interest for fabrication of optical fibers for biomedical applications. Moreover, the disassembly of the FF single crystal is also controllable in the capillary. These findings should be useful in the future development of controlled self-assembly of building blocks to form ultralong single crystals and also to provide a platform for investigating the disassembly of β -amyloid polypeptides.

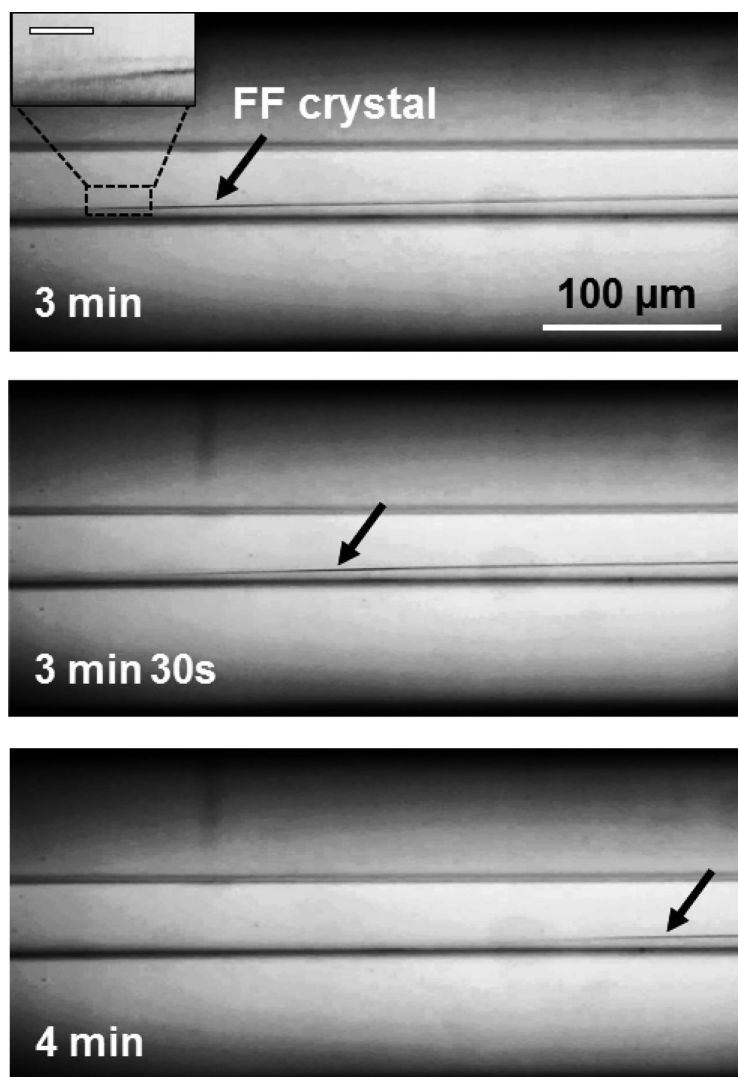


FIGURE 9.9: Disassembly of a FF single crystal in a capillary through addition of a solvent. Bright-field images of a FF fiber in contact with a 5 : 1 HFP/water solution in a sealed capillary with a diameter of 50 μm , taken at 3 min, 3 min 30 sec, and 4 min. The scale bar of the inset image is 10 μm .

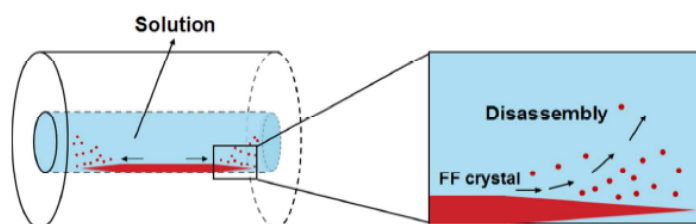


FIGURE 9.10: Schematic of the disassembly process of a FF single crystal in a capillary.

Part IV

Conclusion, Outlook and Ongoing Work

Chapter 10

Outlook

10.1 Film rupture for (less-)ideal mixtures

10.1.1 Behavior for very high concentrations $0.1c_{sat} < c_0 < 0.9c_{sat}$

As in Chapter 4 discussion, the precipitation of solute from diluted solutions is a self-induced change in wettability (Fig. 10.2). Surface modifications are pre-defined modulations of the wettability. The air/liquid interface communicates via vdW-interactions. At a maximum thickness of 30 – 50 nm. However, with high initial alkane concentrations the liquid film surface becomes undulated, and felled out of the scope of this chapter, but is now show here.

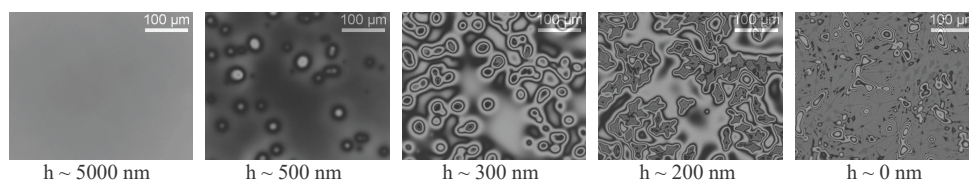


FIGURE 10.1: shows an example measurement of a high initial concentration. The „tick“ film starts to be inhomogeneous in morphology (undulations), and opens earlier, at a global film thickness of around 300 nm, "snap-in" events are visible.

Figure 10.1 follows the thinning and drying of a high concentration alkane solution. The film is planar around its transition height. Thinning further, localized undulations start to appear. Around a thickness of approx 300 nm, "snap-in" events appear inside of the undulations. For both cases, the rheology and the spin-off hydrodynamics of the solvent film do not induce the rupture because the observed processes occur on a very small length scale (far below the transition height). However, in high concentration experiments, the film opens earlier. vdW is not efficient on this length scale anymore. Due to a gradient in surface tension a Marangoni flow is induced. This flow destabilizes the "thick" film (inset Fig. 10.2). The cartoon shows a proposed mechanism, similar to the one in Chapter 7 discussed Marangoni effect destabilizing the liquid.

Defining a global rupture thickness $h_{rupture}$ starts to become obsolete, since the behavior becomes more and more heterogeneous. A high concentrated solution film is more sensitive. Undulations driven by solute Marangoni flows caused by a lateral inhomogeneity in evaporation, dominate the topology of the liquid film.

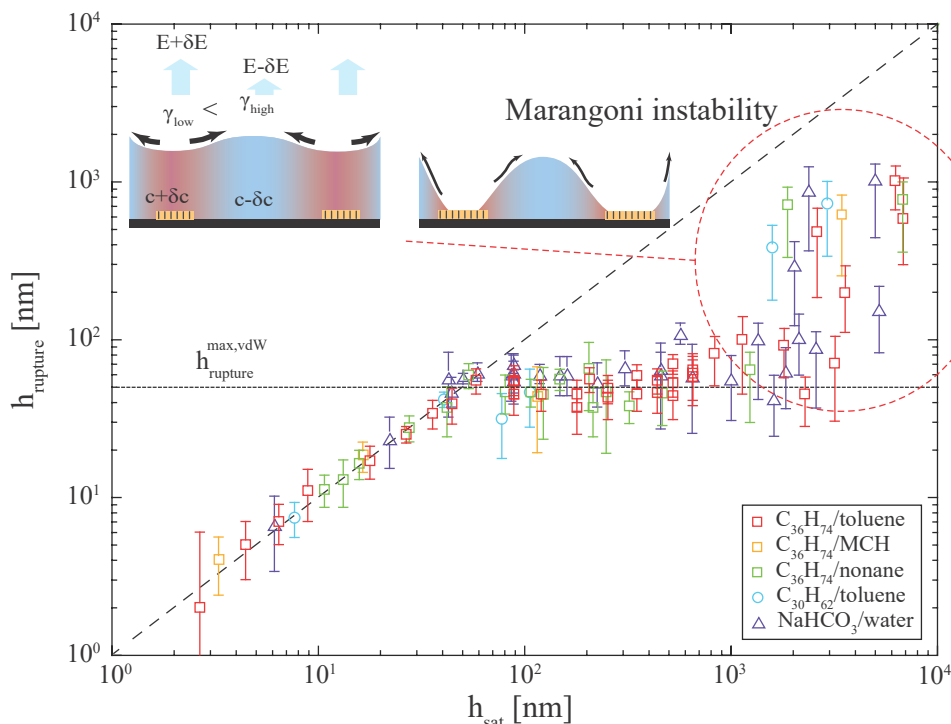


FIGURE 10.2: (a) an expanded plot of $h_{rupture}$ as function of h_{sat} . The dashed line shows $h_{rupture} = h_{sat}$. For concentrations h_{sat} smaller than μm , the behavior follows the in Chapter 4 presented mechanism. The dashed circle indicates even higher concentrations, which don't flow the vdW-rupture scenario anymore.

These films are not planar anymore. Nevertheless, films with very high initial alkane concentrations ($0.1c_{sat} < c_0 < 0.9c_{sat}$) show the following relevant behavior:

Occasionally alkane multi-layer domains are observed, which are attached to the substrate and underneath (i.e., covered by) a rather thick ($\gg 100$ nm), whole (unruptured) alkane/solvent film. As soon as the film on top of the multilayer domains becomes sufficiently thin (≈ 50 nm), it ruptures at the location of these domains. Shown in Figure 10.3.

Repeatedly alkane domains are observed, which are attached to the film/air interface of a rather thick ($\gg 100$ nm) alkane/solvent film. The location of these domains can be identified, because a) they are moving laterally relative to the substrate surface (floating) and b) they visibly distort the film surface in their vicinity. Again, the film ruptures preferentially at the location of these floating domain as soon as it is thin enough (≈ 50 nm). Shown in Figure 10.4.

Very rarely alkane domains are observed, which float within a thick ($\gg 100$ nm) film. These domains move laterally relative to the substrate surface without causing a film surface distortion. This case is so rare that we do not have conclusive experimental data on how these domains influence film rupture. It appears as if these floating domains attach to one of the interfaces during film thinning and eventually the film ruptures as described in the two cases with the domains attached to the interfaces. Shown in Figure 10.5.

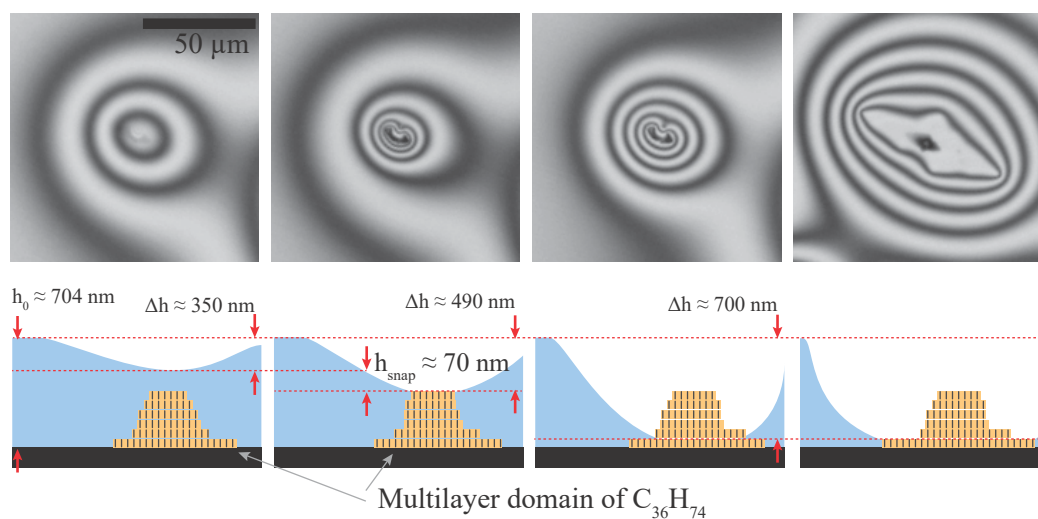


FIGURE 10.3: The top row shows images only 1 ms apart with the corresponding cartoons underneath. 1. An alkane multilayer domain is visible through a solution film. The liquid film is slightly indented. Using the interference fringes, the film has an indent of $\Delta h \approx 350$ nm. 2. The liquid film comes into contact with the underlying domain, visible due to the sharper interference fringes. The thickness difference to the planar film is now $\Delta h \approx 490$ nm. 3. The liquid film slips down on the sides of the multilayer domain. The thickness difference is now $\Delta h \approx 700$ nm. 4. On the level of the solid substrate, the film continues to dewet on presumably a last mono-layer of the alkane.

Compared to the picture before, the Δh does not seem to change anymore.

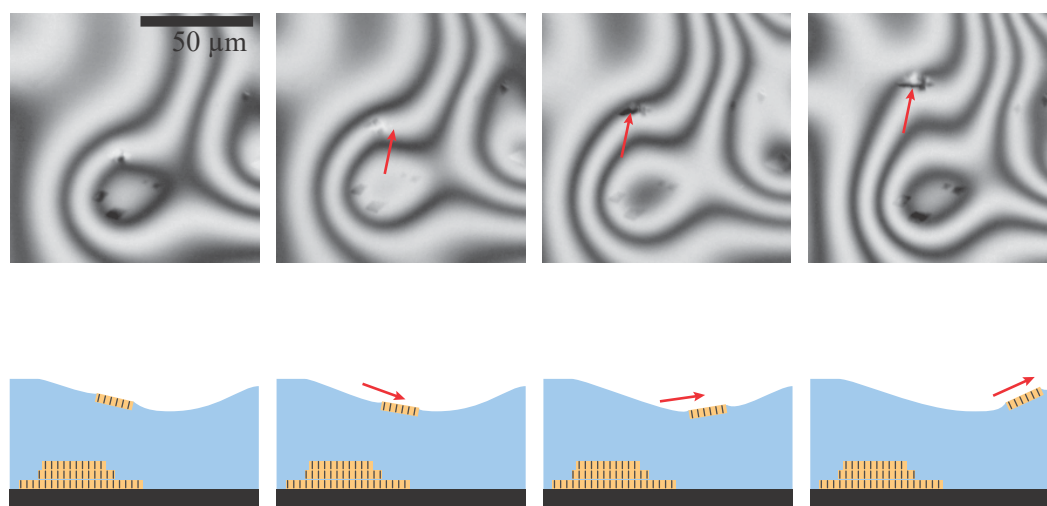


FIGURE 10.4: Alkane Domain swimming on the surface of a liquid film

10.2 Meniscus shape around nanoparticle

10.2.1 Reversible switching between different menisci

The NPs are embedded in this film and they distort the film surface in their vicinity just as show in Chapter 5 in the case of the thinning liquid film (Figure 5.3) or in the case of the solid PS-film (Figure 5.5). This meniscus formation in the case of

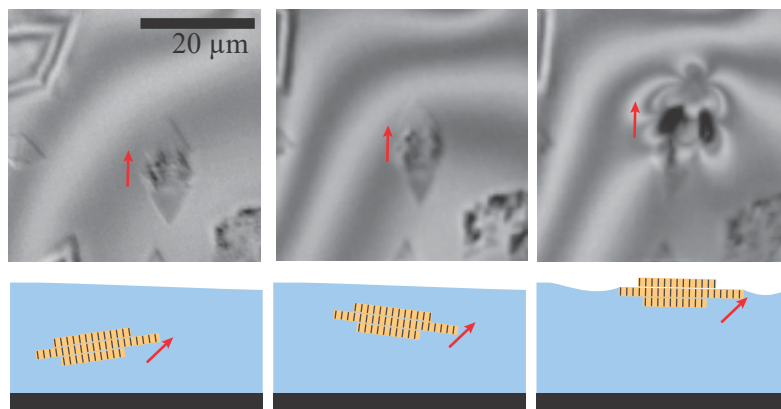


FIGURE 10.5: Image sequence of an alkane domain float within a thick film and eventually snapping to the vapor interface. (As a point of reference, an multilayer domain on the solid is also depicted in the cartoon.)

the co-deposited n-alkane film can be inferred from the strongly enhanced optical visualization of the NP locations.

Figure 10.6 demonstrates how the imaging contrast can be switched on and off by changing the distortion of the surface adjacent to the NP. This has been achieved by switching between the solid and the liquid state of a thin film of a long chain n-alkane ($C_{30}H_{62}$) that is deposited on the substrate surface in addition to the NPs. Below their melting temperature ($T_m = 67^\circ C$) the alkanes form areas with solid planar mono- and multilayers of uniform thickness (each layer is as thick as the length of one molecule [82, 85–87, 225]). In the solid state the planar alkane film morphology is not affected by the NPs. This is verified by the AFM imaging and the corresponding height profile. Above their melting point the alkanes form a closed liquid film on the substrate.

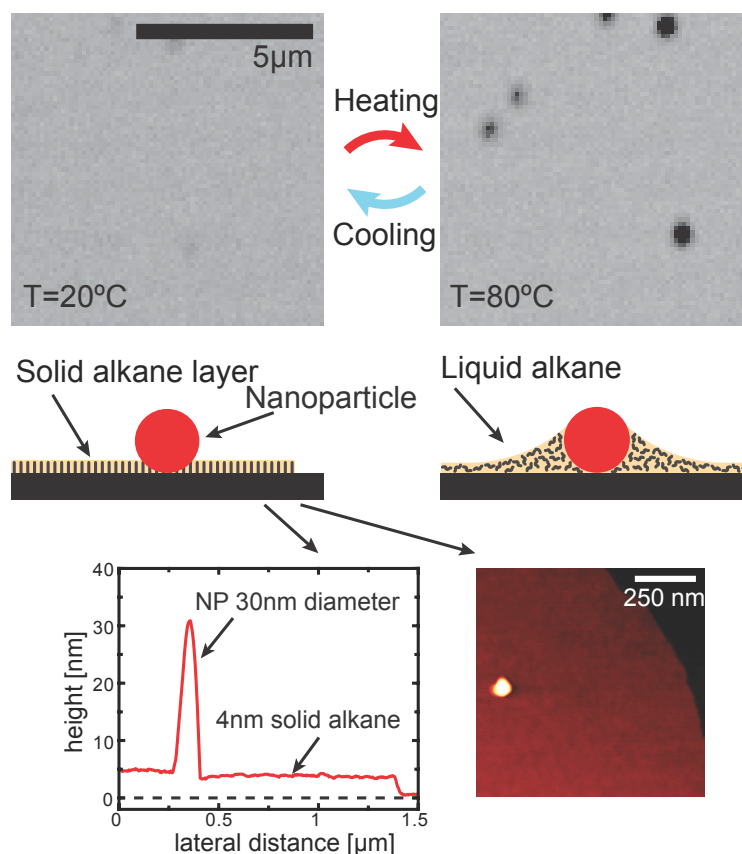


FIGURE 10.6: Optical microscopy imaging (top row), schematics (middle row), and AFM imaging (lower row) of NPs deposited on a planar silica surface together with a thin layer of a long chain n-alkane ($\text{C}_{30}\text{H}_{62}$). At temperatures below its melting point ($T_m = 67^{\circ}\text{C}$) the alkane forms areas with planar films consisting of mono- and/or multilayers with layers of uniform thickness (= the length of the alkane molecules). The NPs do not deform these solid alkane films. At temperatures above its melting point, the molten alkane forms a liquid film. This film completely wets the substrate surface and (presumably) forms a liquid meniscus around the NPs. This can be inferred from the strongly enhanced optical visibility of the location of the NPs in this case.

Chapter 11

Conclusion

The first part of the experimental results presented in this thesis deal with the evolution of planar evaporating liquid films of mixtures on planar solid substrates. If pure liquids, or (*near-*) *ideal solutions*, are continuously thinning, 1) they eventually become thin enough to notice even small changes in surface topology (defects, dust, or intended structures) or surface chemistry (wettability). 2) And for binary mixtures on the other hand, will in case of two volatile components eventually dry completely, but their dynamics will differ substantially. Their composition is changing continuously, drastically changing the physical properties of these mixtures. During film thinning, hydrodynamic effects like Marangoni flow will dominate the surface topology, and destabilize the planar film thinning.

Chapter 4 deals with the evaporative film thinning behaviour of a mixture of a volatile solvent and a nonvolatile (precipitating/crystallizing) solute. The experimental results and their analysis reveal three significant and important findings: 1.) the films rupture if a.) the solute concentration reaches its saturation value and b.) the film is as thick or thinner than a certain film thickness, $h_{rupture}^{max}$. 2.) The rupture behavior is universal in view of the really very large variation of initial solute concentrations and different combinations of solute/solvent, 3.) In all cases $h_{rupture}^{max}$ has a value somewhere between more than 10 nm and less than 100 nm. It is suggested that the crystallization of the solute at the film/substrate interface alters locally the wetting properties. This leads to the film rupture at this location. The value of $h_{rupture}^{max}$ is an indication and consistent with VdW-interactions as the main reason for the film rupture. It can be assumed that such a film rupture mechanism is rather widespread. For instance, most natural aqueous solutions contain non-volatile, precipitating/crystallizing components such as salts.

Chapter 5 presents how to localize and analyze the environment of individual NPs attached to planar substrates embedded in liquid films as thin or thinner than the nanoparticle size. Although the NPs are much smaller than the Rayleigh diffraction limit they can be investigated with optical reflection microscopy. This can be done, because the NPs create a distortion of the surrounding film surface (meniscus), which expands laterally over orders of magnitude further than the size of the NPs. Therefore the meniscus shape can even be measured by optical interferometry. The meniscus has a cosine hyperbolic (zero net curvature) shape. Therefore there is no (capillary) pressure difference between the liquid of the far field planar film and the liquid in the meniscus region. It is unknown what determines the decay length of

the meniscus. The decay length is independent from the thickness of the far field planar film. It decreases with smaller sizes of the NP.

Chapter 6 presents a "recipe" for those who want to apply evaporative spin casting to achieve a specific solute coverage, more specifically, a polymer coating with a certain pre-determined thickness. Based on detailed experimental investigations, it is discussed in a transparent approach how a final "master" formula is extracted to predict the final polymer coverage from the process parameters (Eq. 6.6). Only a few easily measurable bulk system parameters (η_0, ρ_0, ω) and one "calibration" experiment (determination of "e") are necessary and sufficient to describe the process and to predict the final solute coverage. Beyond that, the data and analysis presented disclose a transparent picture on the physics occurring during evaporative spin casting, such as the thinning behavior, the evaporation behavior, and the evolution of the solute concentration.

Chapter 7 investigates the temporal and spacial evolution of binary mixtures of volatile liquids. Both liquids individually wet the substrate completely and form planar continuous films during their evaporative film thinning. The experimental and their analysis reveal the following: 1) binary mixtures of volatile liquids with a $\Delta\gamma < 0$ build planar, continuous (stable) films during their evaporative thinning. 2) thinnign films from mixtures with $\Delta\gamma > 0$ can be stable or may form undulating or even rupturing (unstable) films. The stability in the case of $\Delta\gamma > 0$ depends on the composition x_0 , and/or on the ratio of evaporation rates E_f/E_s . For very small or very big x_0 films remain stable, despite $\Delta\gamma > 0$. 3) unstable mixtures show undulation with wavelengths λ , which depend on x_0 . 4) during film thinning of unstable films the wavelength decreases with time (respectively film thickness). A basic mechanism is proposed assuming that a Marangoni flow initiated by random fluctuations of the local evaporation rate can enhance or suppress a further destabilization of the film surface.

The second part of this thesis studies the sequential film formation/deposition with a (moving) three phase line and crystallization processes in the vicinity of the contact line. One aim of these investigations was the controlled growth of diphenylalanine crystals/fibers. *Chapter 8* presents dip casting as a new controllable approach for the aligned arrangement of dipeptide single crystals. The induced nucleation and a substrate withdrawal system allow the continuously oriented growth of uniform size crystals from solution with a technically unlimited length. Structures of growing crystals can be controlled by the process parameters. *Chapter 9* presents an additional methode to direct the self-assembly of FF single crystals under well-controlled conditions in small capillaries. This approach makes it possible to obtain ultra long individual FF single crystals under the provided conditions such as capillary diameter, solvent composition, and solvent evaporation rate. Because it is possible to prepare very long single crystals of FF the procedure is of interest for the fabrication of optical fibers for (biomedical) applications. Moreover, the disassembly of the FF single crystal is also controllable in the capillary.

Part V
Appendix

Appendix A

Appendix A

A.1 Gray to Thickness

A.1.1 Fresnel Equations

Following code was used to calculate the reflective response of toluene and water, using the Mathematica version of the program code by Steve Byrnes[59]:

```
dList1[dinnm_] = {∞, dinnm nm, 48 nm, ∞};
nList1 = {1.0003, 1.3334, 1.4656, 4.7302};
dList2[dinnm_] = {∞, dinnm nm, 48 nm, ∞};
nList2 = {1.0003, 1.5057, 1.4656, 4.7302};
```

The reflectivity as function of the thickness d for toluene and water:

$$R_{toluene}(d) = 1 + \frac{3.56438 + 1.11022 \cdot 10^{-16} \cdot \cos[0.0425195 \cdot d]}{-5.23357 + 0.477467 \cdot \cos[0.0425195 \cdot d] + \sin[0.0425195 \cdot d]}$$

$$R_{water}(d) = 1 + \frac{16.1709}{-22.5775 + \cos[0.0376539 \cdot d] + 3.14435 \cdot \sin[0.0376539 \cdot d]}$$

A.2 Supporting information for Chapter 5

A.2.1 Analytical Expression of the Film Distortion

Figure A.1 shows the theoretically assumed meniscus profile, parameters and boundary conditions that were used to fit the experimentally measured profiles. For the fits we assume a given size of the NP with a radius $R = (0.5 \cdot d_{NP})$. This NP is attached to the substrate and embedded in the liquid film. The film has a given (interferometric measured) far-field thickness, h_{∞} . Near to the particle, it is assumed that the meniscus has a hyperbolic cosine profile. It is assumed further that the meniscus contacts the NP at a circle at height relative to the substrate surface of $z = h_c$ and a distance from the z -axis of $r = r_c$. The contact angle of the liquid with the NP surface is Θ_c . At a distance of $r = L$ from the z -axis the hyperbolic cosine curve reaches the liquid film surface plane. The angle of intersection is rather small (with $L < \infty$ it cannot be

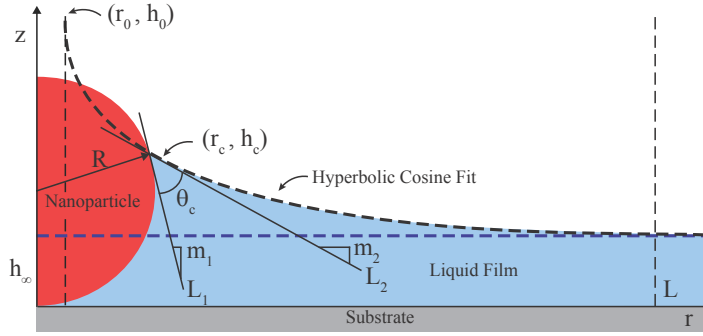


FIGURE A.1: Meniscus geometry and definition of the parameters.

zero). Hyperbolic cosine curves with these specifications are equivalent to meniscus profiles, which contact a vertical round cylinder (e.g. a fiber) of radius $r = r_0$ at a height $z = h_0$ with $\Theta_c = 0$.

A.2.2 Surface Shape

The meniscus shape of the liquid film distorted by a cylinder is described by the following catenary curve.

$$r(z) = r_0 \cdot \cosh\left(\frac{z - h_0}{r_0}\right). \quad (\text{A.1})$$

The Eq.A.1 in its exponential form (Eq. A.2) can be solve as an expression for $z(r)$:

$$u = \frac{e^w + e^{-w}}{2}. \quad (\text{A.2})$$

Where

$$u = \frac{r(z)}{r_0}. \quad (\text{A.3})$$

$$w = \frac{z - h_0}{r_0}. \quad (\text{A.4})$$

The domain of the Eq A.2 is restricted as $[0, +\infty) \rightarrow [1, +\infty)$. After algebraic arrangements the function is inverted to the hyperbolic arc cosine by solving the quadratic Equation A.5.

$$0 = e^{2w} - 2ue^w + 1 \quad (\text{A.5})$$

The solutions are:

$$e^w = u \pm \sqrt{u^2 - 1} \quad (\text{A.6})$$

Both are positive so by substitution of u and w in Eq. A.6 the meniscus shape can be written as.

$$z(r) = h_0 \pm r_0 \cdot \ln\left(\frac{r}{r_0} + \sqrt{\left(\frac{r}{r_0}\right)^2 - 1}\right). \quad (\text{A.7})$$

The Eq. A.7 has two solution the positive (growing) and the negative (decaying) branch. The meniscus is described by the negative branch. In order to introduce a complete description of the surface profile we introduced the length L as an exponential decay factor, to describe the transition from the hyperbolic cosine behaviour (Eq. A.7) to the planar far-field surface.

$$z(r) = \left[h_0 - r_0 \cdot \ln \left(\frac{r}{r_0} + \sqrt{\left(\frac{r}{r_0} \right)^2 - 1} \right) \right] e^{-\frac{r}{L}} + h_\infty. \quad (\text{A.8})$$

A.2.3 Contact to the particle

It is known The angle of interception ($r_c; h_c$) above two curves correspond to the angle form between the two tangents with the instantaneous slope at meeting point; which is given by the corollary formula:

$$\Theta_c = \arctan \left(\frac{m_1 - m_2}{1 + m_1 \cdot m_2} \right); \quad (\text{A.9})$$

Where the slopes m_1 and m_2 are given as:

$$m_1 = \pm \frac{R - h_c}{\sqrt{R^2 - (h_c - R)^2}}. \quad (\text{A.10})$$

$$m_2 = \sinh \left[\operatorname{arcosh} \left(\frac{\sqrt{R^2 - (h_c - R)^2}}{r_0} \right) \right]. \quad (\text{A.11})$$

A.2.4 Numerical Data Analysis

The meniscus profiles where fitted with the Software OriginPro. Equation A.8 was used from the contact to the particle to the far-field surface; the distance where the Eq A.1 transits to the h_∞ is the length L , which is given by the fit (Eq.A.8); the contact point with the particle (r_c, h_c) was iterated with three digits until the R-Square was at least 0.99. From the fit the contact to the imaginary/ideal fiber (r_0, h_0) was taken, allowing to estimate the contact angle by Eq. A.9.

A.3 Supporting Information for Chapter 8

A.3.1 The influence of initial concentration of NH_4OH and temperature on the structures of FF fibers.

The concentration of NH_4OH , solvent evaporation rate show great influence on the formation of FF fibers. We have made crystallization experiments over a broad range of concentrations of NH_4OH , from 0.006 to 14.80 mol/L. The obtained horizontally aligned fibers with the diameter of about 1 – 2 μm are obtained on the silicon wafer from 0.006 and 2.89 mol/L NH_4OH , however masses formed from 14.80 mol/L NH_4OH (Figure A.2b-d). The different morphology of FF fibers may attribute to the

different FF concentration when the fibers start to grow. It takes different time for nucleation with different NH_4OH concentration of 10 min (0.006 mol/L), 30 min (2.89 mol/L) and 60min (14.80 mol/L). In 0.006 and 2.89 mol/L NH_4OH , the solubility of FF reduces in the whole process with evaporation of solvent (Figure A.2a). Nevertheless, in 14.80 mol/L NH_4OH , the solubility increases firstly and decrease, leading to long time for supersaturation. The FF concentration is pretty high and more FF fibers formed on the silicon wafer, which make the fibers amorphous (Figure A.2d). Temperature can influence the evaporation speed. In 0.006 mol/L NH_4OH solution, when temperature is decreased to be 38 °C, the nucleation time of FF fibers on the scratch becomes longer (40 min) than that of at 75 °C (10 min) and less aligned FF fibers with the larger diameter of 2 – 3 μm form on the silicon wafer (Figure A.2a). The FTIR and XRD analyses confirm the β -sheet secondary structure and highly crystalline character of all the FF fibers (Figure A.2e, f). This Figure A.2 results indicate that our process makes the growth of aligned crystals with different structure controllable, which is great importance for their functional device.

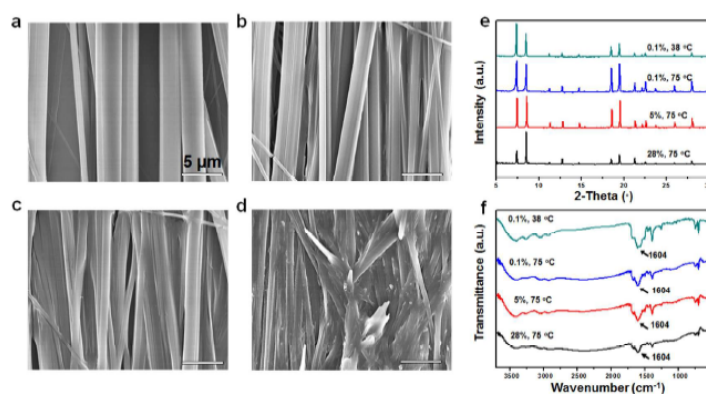


FIGURE A.2: Aligned FF fibers formed under different NH_4OH concentration and temperature. a) SEM image of fibers in 0.006 mol/L NH_4OH at 38 °C. b) SEM image of fibers in 0.006 mol/L NH_4OH at 75 °C. c) SEM image of fibers in 2.89 mol/L NH_4OH at 75 °C. d) SEM image of fibers in 14.80 mol/L NH_4OH at 75 °C. Scale bar, 5 μm . e) FTIR and f) XRD analyses of the FF fibers. $c_0 = 0.026$ g/L, withdrawal speed, 2 $\mu\text{m}/\text{sec}$.

A.3.2 Movie S1

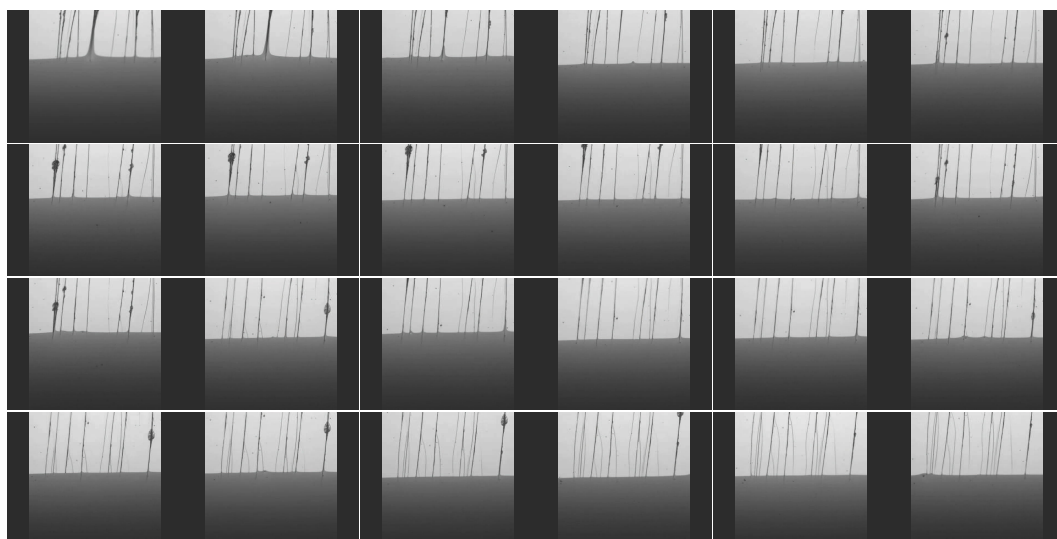


FIGURE A.3: Screen captures (0.5 s apart) of a movie showing the growth of aligned FF single crystals on silicon wafer with the withdrawal of substrate.

A.3.3 Author information, Acknowledgments & Rights

Author Contributions: B.S., Q.L., S.E., L.D., Y.Y., Y.J., R.P.G., G.C., and J.F. performed the experiments. J.L., H.R., H.K., and B.S. designed the study and advised on manuscript preparation. All authors contributed to writing the paper.

Notes: The authors declare no competing financial interest.

Acknowledgments: The authors acknowledge the financial support from National Basic Research Program of China (973 Program, 2013CB932802) and National Natural Science Foundation of China (Project Nos. 21433010, 21320102004, 21673056). B.S., Q.L., H.R., S.E., L.D., R.P.G., Y.J., G.C., J.F., K.H., and J.L. received funding from National Nature Science Foundation China (21433010, 21320102004) and National Basic Research Program of China (2013CB932800). Y.Y. received funding from National Nature Science Foundation of China (21673056).

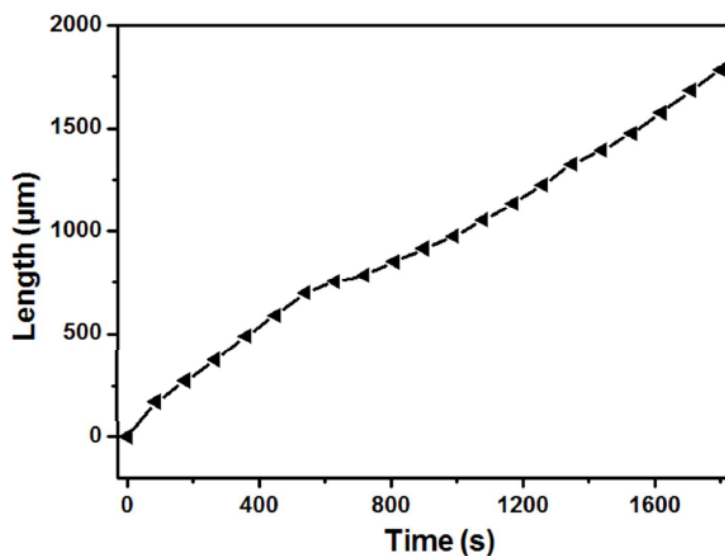


FIGURE A.4: Length of a FF fiber in a capillary as a function of time. The inner diameter of the capillary is 50 μm .

Molecular Formula	$\text{C}_{18}\text{H}_{18}\text{N}_2\text{O}_2$
Molecular weight	294.35
Crystal system	Hexagonal
Space group	P6
Cell parameters	$a = b = 24.77 \text{ \AA}, c = 5.42 \text{ \AA}, \alpha = \beta = 90^\circ, \gamma = 90^\circ$
Cell volume	2881 \AA^3
Z	6
Radiation used	Cu ($\lambda = 1.5418 \text{ \AA}$)
Temperature	25 $^\circ\text{C}$
Range (2θ)	2.75 – 46.70 $^\circ$

TABLE A.1: Structural parameters of a FF single crystal obtained by XRD pattern refinement

A.4 Supporting Information for Chapter 9

A.4.1 Movie S1

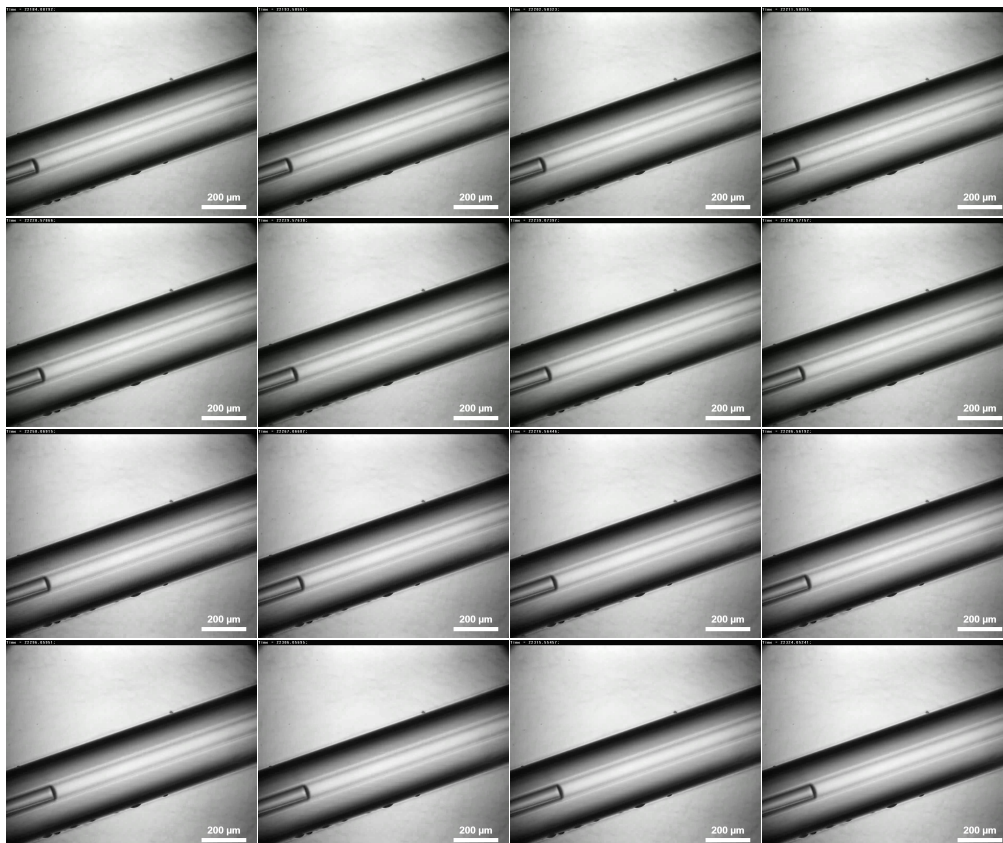


FIGURE A.5: Screen captures (0.5 s apart) of a movie showing directed growth of a FF single crystal in a capillary. The inner diameter of the capillary is 50 μm.

A.4.2 Movie S2



FIGURE A.6: Screen captures (0.5 s apart) of a movie showing disassembly of a FF single crystal in a capillary on addition of solvent. The inner diameter of the capillary is 50 μm .

A.4.3 Author information, Acknowledgments & Rights

Author Contributions: B.S., S.E., L.D., Y.L., G.L., Y.Y., Q.L., M.F., and J.F. performed the experiments. J.L. and H.R. designed the system and advised on manuscript preparation. All authors contributed to writing the paper.

Notes: The authors declare no competing financial interest.

Acknowledgments: The authors acknowledge the financial support from National Basic Research Program of China (973 program, 2013CB932802) and National Natural Science Foundation of China (Project Nos. 21433010, 21320102004, 21673056). B.S., H.R., L.D., S.E., Y.L., G.L., Q.L., M.F., J.F., and J.L. received funding from National Nature Science Foundation of China (21433010, 21320102004) and National Basic Research Program of China (2013CB932800). Y.Y. received funding from National Nature Science Foundation of China (21673056).

A.5 Characterization methods for Chapter 8 and 9

A.5.1 Characterization of FF

The scanning electron microscopy (SEM) images of the samples were obtained by a scanning electron microscope S-4800 (Hitachi, Japan) with a 10 kV accelerating voltage. Atomic force microscope (AFM) images were taken with a NanoWizard III (JPK, Germany). The transmission electron microscopy (TEM) experiments were performed on a JEM-1011 (JEOL, Japan). FTIR spectroscopy was recorded with a Bruker TENSOR-27 spectrometer (Bruker, Germany). XRD patterns were collected

The figure shows two screenshots of the RightsLink website. The left screenshot is for the article "Self-Assembly of Ultralong Aligned Dipeptide Single Crystals" by Bingbing Sun, Qi Li, Hans Riegler, et al., published in ACS Nano in 2017. The right screenshot is for the article "Directed Self-Assembly of Dipeptide Single Crystal in a Capillary" by Bingbing Sun, Hans Riegler, Lulu Dai, et al., published in ACS Nano in 2018. Both screenshots show the article title, author, publication, and date, followed by a "PERMISSION/LICENSE IS GRANTED FOR YOUR ORDER AT NO CHARGE" notice and a list of conditions for use. The conditions include: permission for print and electronic formats, adaptation of figures and tables, printing for records, appropriate credit for the material, and one-time permission for the specified use.

FIGURE A.7: One-time permission for adapted reprint of (left) Bingbing Sun *et al.* "Self-Assembly of Ultralong Aligned Dipeptide Single Crystals". In: ACS nano 11.10 (2017), pp. 10489–10494 and (right) Bingbing Sun *et al.* "Directed Self-Assembly of Dipeptide Single Crystal in A Capillary". In: ACS nano (2018), for usage in this thesis.

on a Rigaku D/max 2500 instrument under the following conditions: Cu $K\alpha$ radiation, scan speed of $2^\circ/\text{min}$, $\lambda = 1.5405 \text{ \AA}$, and 25°C . The polarizing photographs of the aligned crystals were obtained on an Olympus AX70 microscope. The optical waveguide property of the single crystal was tested by self-assembled local illumination microscopy.

A.5.2 Optical Waveguiding Property of the FF Single Crystal

RhB was dissolved in HFP/water solution, and FF powders were then dissolved in this solution for the synthesis of a RhB-doped FF fiber. The two ends of the capillary were broken to let the FF fiber out. One end of the fiber was excited by a laser (488 nm), and images of the capillary were taken by a camera.

List of Abbreviations

vdW	Van der Waals
AFM	Atomic Force Microscopy
SEM	Scanning Electron Microscopy
OM	Optical Microscopy
SC	Spin Casting (or Spin Coating)
CVD	Chemical Vapor Deposition
PVD	Physical Vapor Deposition
LASER	Light Amplification by Stimulated Emission of Radiation
LED	Light-Emitting Diode
FWHM	Full Width at Half Maximum
CMOS	Complementary metal-oxide-semiconductor
CCD	Charge-coupled device
FoV	Field of View
AoI	Area of Interest
px	Pixel
fps	Frames Per Second
DMF	N, N-Dimethylformamide
MCH	Methylcyclohexane
EA	Ethyl Acetate
HFP	Hexafluoropropylene
tol	Toluene
dec	n-Decane
non	n-Nonane
oct	n-Octane
hep	n-Hepane
hex	n-Hexane
NP	Nano particle
PS	Poly Styrene
PMMA	Poly(methyl methacrylate)
FF	Dipeptide diphenylalanine

List of Symbols

p	pressure	$M \cdot L^{-1} \cdot T^{-2}$
T	temperature	Θ
E	evaporation rate	$L \cdot T^{-1}$
K	spin off coefficient	$L^{-2} \cdot T^{-1}$
h_{tr}	transition height	L
t_{tr}	transition time	T
t_{sc}	process time	T
Sh_{tr}	Sherwood number	dimensionless
ω	angular frequency	T^{-1}
η	dynamic viscosity	$M \cdot L^{-1} \cdot T^{-1}$
ν	kinematic viscosity	$L^2 \cdot T^{-1}$
D	diffusion coefficient	$L^2 \cdot T^{-1}$
c_{sat}	saturation concentration	$N \cdot L^{-3}$
c_0	initial concentration	$N \cdot L^{-3}$
c	concentration	$N \cdot L^{-3}$
x_0	initial concentration	$M \cdot M^{-1}$
x	concentration	$M \cdot M^{-1}$
h_{sat}	saturation height	L
$h_{rupture}$	rupture height	L
h_{∞}	far field film thickness	L
h_0	far field film thickness	L
h_f	final film thickness	L
Γ	coverage	$N \cdot L^{-2}$
L	distortion length	L
d_{NP}	nano particle diameter	L
Ma	Marangoni number	dimensionless
λ	wave length	L
θ	contact angle	dimensionless
γ	interfacial tension	$M \cdot T^{-2}$
ρ	density	$M \cdot L^{-3}$

Bibliography

- [1] James Thomson. "XLII. On certain curious motions observable at the surfaces of wine and other alcoholic liquors". In: *Philosophical Magazine Series 4* 10.67 (1855), pp. 330–333.
- [2] Carlo Marangoni. *Sull'espansione delle gocce d'un liquido galleggianti sulla superficie di altro liquido*. 1865.
- [3] David Carteau, Dario Bassani, and Isabelle Pianet. "The "Ouzo effect": Following the spontaneous emulsification of trans-anethole in water by NMR". In: *Comptes Rendus Chimie* 11.4-5 (2008), pp. 493–498.
- [4] DM Lynch and CW Bamforth. "Measurement and characterization of bubble nucleation in beer". In: *Journal of food science* 67.7 (2002), pp. 2696–2701.
- [5] Svenja K Reinke et al. "Changes in contact angle providing evidence for surface alteration in multi-component solid foods". In: *Journal of Physics D: Applied Physics* 48.46 (2015), p. 464001.
- [6] Robert D Deegan et al. "Capillary flow as the cause of ring stains from dried liquid drops". In: *Nature* 389.6653 (1997), p. 827.
- [7] Stephan Eickelmann. "Real-Time Imaging Study of Ultra-Thin Liquid Films in a Spin-Cast Configuration". MA thesis. Potsdam, Germany: University of Potsdam, 2014.
- [8] Stephan Eickelmann and Hans Riegler. "Rupture of ultrathin solution films on planar solid substrates induced by solute crystallization". In: *Journal of Colloid and Interface Science* 528 (2018), pp. 63–69.
- [9] Daniel TW Toolan and Jonathan R Howse. "Development of in situ studies of spin coated polymer films". In: *Journal of Materials Chemistry C* 1.4 (2013), pp. 603–616.
- [10] Leonard W Schwartz et al. "Dewetting patterns in a drying liquid film". In: *Journal of colloid and interface science* 234.2 (2001), pp. 363–374.
- [11] Neil Mulji and Sanjeev Chandra. "Rupture and dewetting of water films on solid surfaces". In: *Journal of colloid and interface science* 352.1 (2010), pp. 194–201.
- [12] Weibin Li, Ding Lan, and Yuren Wang. "Dewetting-mediated pattern formation inside the coffee ring". In: *Physical Review E* 95.4 (2017), p. 042607.
- [13] Emil D Manev and Anh V Nguyen. "Critical thickness of microscopic thin liquid films". In: *Advances in colloid and interface science* 114 (2005), pp. 133–146.
- [14] Uwe Thiele, Michael Mertig, and Wolfgang Pompe. "Dewetting of an evaporating thin liquid film: Heterogeneous nucleation and surface instability". In: *Physical review letters* 80.13 (1998), p. 2869.
- [15] Günter Reiter. "Dewetting of thin polymer films". In: *Physical Review Letters* 68.1 (1992), p. 75.

- [16] Guenter Reiter. "Unstable thin polymer films: rupture and dewetting processes". In: *Langmuir* 9.5 (1993), pp. 1344–1351.
- [17] Günter Reiter, Philippe Auroy, and Loïc Auvray. "Instabilities of thin polymer films on layers of chemically identical grafted molecules". In: *Macromolecules* 29.6 (1996), pp. 2150–2157.
- [18] Jörg Bischof et al. "Dewetting modes of thin metallic films: nucleation of holes and spinodal dewetting". In: *Physical Review Letters* 77.8 (1996), p. 1536.
- [19] Ralf Seemann, Stephan Herminghaus, and Karin Jacobs. "Gaining control of pattern formation of dewetting liquid films". In: *Journal of Physics: Condensed Matter* 13.21 (2001), p. 4925.
- [20] Xiaohong Gu et al. "Hole-growth instability in the dewetting of evaporating polymer solution films". In: *Journal of Polymer Science Part B: Polymer Physics* 40.24 (2002), pp. 2825–2832.
- [21] LS Fisher and AA Golovin. "Nonlinear stability analysis of a two-layer thin liquid film: Dewetting and autophobic behavior". In: *Journal of colloid and interface science* 291.2 (2005), pp. 515–528.
- [22] Uwe Thiele. "Thin film evolution equations from (evaporating) dewetting liquid layers to epitaxial growth". In: *Journal of Physics: Condensed Matter* 22.8 (2010), p. 084019.
- [23] Dirk Peschka, Andreas Münch, and Barbara Niethammer. "Thin-film rupture for large slip". In: *Journal of Engineering Mathematics* 66.1-3 (2010), pp. 33–51.
- [24] Hangjie Ji and Thomas P Witelski. "Finite-time thin film rupture driven by modified evaporative loss". In: *Physica D: Nonlinear Phenomena* 342 (2017), pp. 1–15.
- [25] Stefan Karpitschka, Constans M Weber, and Hans Riegler. "Spin casting of dilute solutions: Vertical composition profile during hydrodynamic-evaporative film thinning". In: *Chemical Engineering Science* 129 (2015), pp. 243–248.
- [26] John E Lennard-Jones. "Cohesion". In: *Proceedings of the Physical Society* 43.5 (1931), p. 461.
- [27] HC Hamaker. "London-VD waals forces in colloidal systems". In: *Recueil des Travaux Chimiques des Pays-Bas* 57.1 (1938), pp. 61–72.
- [28] Pierre-Gilles De Gennes, Françoise Brochard-Wyart, and David Quéré. "Capillarity and Gravity". In: *Capillarity and Wetting Phenomena*. Springer, 2004, pp. 33–67.
- [29] Ralf Seemann, Stephan Herminghaus, and Karin Jacobs. "Dewetting patterns and molecular forces: A reconciliation". In: *Physical Review Letters* 86.24 (2001), p. 5534.
- [30] Uwe Thiele, Manuel G Velarde, and Kai Neuffer. "Dewetting: Film rupture by nucleation in the spinodal regime". In: *Physical review letters* 87.1 (2001), p. 016104.
- [31] Stefan Karpitschka, Ferenc Liebigh, and Hans Riegler. "Marangoni Contraction of Evaporating Sessile Droplets of Binary Mixtures". In: *Langmuir* 33.19 (2017), pp. 4682–4687.
- [32] Franck Girard, Lionel Gastine-Viennot, and Franck Girard Lionel Gastine-Viennot Sandrine Sandrine Bouisset. MARANGONI NUMBER. 2003. URL: <http://hmf.enseeiht.fr/travaux/CD0203/travaux/optmfn/gpfmho/02-03/grp6/def.html>.

- [33] Steven Abbott. *Printing Science: Principles and Practice*. TCNF Ltd & University of Leeds, 2018. URL: https://www.stevenabbott.co.uk/_downloads/Printing%20Science%20Principles%20and%20Practice.pdf.
- [34] Jose Danglad-Flores, Stephan Eickelmann, and Hans Riegler. "Deposition of polymer films by spin casting: A quantitative analysis". In: *Chemical Engineering Science* 179 (2018), pp. 257–264. ISSN: 0009-2509.
- [35] Alfred G Emslie, Francis T Bonner, and Leslie G Peck. "Flow of a viscous liquid on a rotating disk". In: *Journal of Applied Physics* 29.5 (1958), pp. 858–862.
- [36] Dietrich Meyerhofer. "Characteristics of resist films produced by spinning". In: *Journal of Applied Physics* 49.7 (1978), pp. 3993–3997.
- [37] A Acrivos, MJ Shah, and EE Petersen. "On the Flow of a Non-Newtonian Liquid on a Rotating Disk". In: *Journal of Applied Physics* 31.6 (1960), pp. 963–968.
- [38] Peter C Sukanek. "Dependence of film thickness on speed in spin coating". In: *Journal of The Electrochemical Society* 138.6 (1991), pp. 1712–1719.
- [39] CJ Lawrence. "Spin coating with slow evaporation". In: *Physics of Fluids A: Fluid Dynamics* 2.3 (1990), pp. 453–456.
- [40] Warren W Flack et al. "A mathematical model for spin coating of polymer resists". In: *Journal of Applied Physics* 56.4 (1984), pp. 1199–1206.
- [41] SL Burgess and SDR Wilson. "Spin-coating of a viscoplastic material". In: *Physics of Fluids* 8.9 (1996), pp. 2291–2297.
- [42] Nilesh H Parmar, Mahesh S Tirumkudulu, and EJ Hinch. "Coating flow of viscous Newtonian liquids on a rotating vertical disk". In: *Physics of Fluids* 21.10 (2009), p. 103102.
- [43] Taku Ohara, Yoichiro Matsumoto, and Hideo Ohashi. "The film formation dynamics in spin coating". In: *Physics of Fluids A: Fluid Dynamics* 1.12 (1989), pp. 1949–1959.
- [44] Dirk W Schubert and Thomas Dunkel. "Spin coating from a molecular point of view: its concentration regimes, influence of molar mass and distribution". In: *Materials Research Innovations* 7.5 (2003), pp. 314–321.
- [45] DE Bornside, CW Macosko, and LE Scriven. "Spin coating: One-dimensional model". In: *Journal of Applied Physics* 66.11 (1989), pp. 5185–5193.
- [46] A Jeffrey. "THE ONE-DIMENSIONAL HEAT EQUATION:(Encyclopedia of Mathematics and Its Applications, 23)". In: *Bulletin of the London Mathematical Society* 17.6 (1985), pp. 622–623.
- [47] Robert C Weast, Melvin J Astle, William H Beyer, et al. *CRC handbook of chemistry and physics*. Vol. 1990. CRC press, Boca raton FL, 1989.
- [48] Albert Einstein. "Über die von der molekularkinetischen Theorie der Wärme geforderte Bewegung von in ruhenden Flüssigkeiten suspendierten Teilchen". In: *Annalen der physik* 322.8 (1905), pp. 549–560.
- [49] R Köhler, Paul Lazar, and H Riegler. "Optical imaging of thin films with molecular depth resolution". In: *Applied physics letters* 89.24 (2006), p. 241906.
- [50] Z Knittel. "Optics of thin films.(An optical multilayer theory)." In: *Optics of thin films.(An optical multilayer theory).*, by Knittel, Z.. *Wiley series in pure and applied optics (New York, NY (USA): John Wiley & Sons)*, 548 p. (1976).
- [51] Augustin Fresnel. *Sur la loi des modifications imprimées à la lumière polarisée par sa réflexion totale dans l'intérieur des corps transparents*. 1823.

- [52] Charles C Ih. *Speckle elimination by random spatial phase modulation*. US Patent 4,155,630. May 1979.
- [53] Qing-Long Deng et al. "A hybrid temporal and spatial speckle-suppression method for laser displays". In: *Optics Express* 21.25 (2013), pp. 31062–31071.
- [54] F Horowitz et al. "Real-time optical monitoring of spin coating". In: *Journal de Physique III* 3.11 (1993), pp. 2059–2063.
- [55] Dunbar P Birnie III. "Combined flow and evaporation during spin coating of complex solutions". In: *Journal of Non-crystalline solids* 218 (1997), pp. 174–178.
- [56] William Henry Bragg, BA WL Bragg, et al. "The reflection of X-rays by crystals". In: *Proc. R. Soc. Lond. A* 88.605 (1913), pp. 428–438.
- [57] Peter de Groot. "Principles of interference microscopy for the measurement of surface topography". In: *Advances in Optics and Photonics* 7.1 (2015), pp. 1–65.
- [58] Steve J Byrnes. *Science computer programs*. 2018. URL: <http://sjbyrnes.com/science-computer-programs/>.
- [59] Steven J Byrnes. "Multilayer optical calculations". In: *arXiv preprint arXiv:1603.02720* (2016).
- [60] S Karpitschka. "Dynamics of liquid interfaces with compositional gradients". PhD thesis. PhD thesis, Universität Potsdam, 2012.
- [61] Gerd Binnig, Calvin F Quate, and Ch Gerber. "Atomic force microscope". In: *Physical review letters* 56.9 (1986), p. 930.
- [62] AK Baker and PE Dyer. "Refractive-index modification of polymethylmethacrylate (PMMA) thin films by KrF-laser irradiation". In: *Applied Physics A* 57.6 (1993), pp. 543–544.
- [63] Feridun Ay et al. "Prism coupling technique investigation of elasto-optical properties of thin polymer films". In: *Journal of applied physics* 96.12 (2004), pp. 7147–7153.
- [64] Pierre-Gilles De Gennes. "Wetting: statics and dynamics". In: *Reviews of modern physics* 57.3 (1985), p. 827.
- [65] Uwe Thiele. "Open questions and promising new fields in dewetting". In: *The European Physical Journal E* 12.3 (2003), pp. 409–416.
- [66] Daniel Bonn et al. "Wetting and spreading". In: *Reviews of modern physics* 81.2 (2009), p. 739.
- [67] Jacco H Snoeijer and Bruno Andreotti. "Moving contact lines: scales, regimes, and dynamical transitions". In: *Annual review of fluid mechanics* 45 (2013).
- [68] Erik Schäffer et al. "Electrically induced structure formation and pattern transfer". In: *Nature* 403.6772 (2000), p. 874.
- [69] Kajari Kargupta and Ashutosh Sharma. "Templating of thin films induced by dewetting on patterned surfaces". In: *Physical Review Letters* 86.20 (2001), p. 4536.
- [70] A Sharma. "Many paths to dewetting of thin films: anatomy and physiology of surface instability". In: *The European Physical Journal E* 12.3 (2003), pp. 397–408.
- [71] Richard P Wool. "Self-healing materials: a review". In: *Soft Matter* 4.3 (2008), pp. 400–418.
- [72] Taesoo D Lee and Abasifreke U Ebong. "A review of thin film solar cell technologies and challenges". In: *Renewable and Sustainable Energy Reviews* 70 (2017), pp. 1286–1297.

- [73] Andrew M Telford, Stuart C Thickett, and Chiara Neto. "Functional patterned coatings by thin polymer film dewetting". In: *Journal of colloid and interface science* 507 (2017), pp. 453–469.
- [74] A Sheludko. "Thin liquid films". In: *Advances in Colloid and Interface Science* 1.4 (1967), pp. 391–464.
- [75] Malcolm B Williams and Stephen H Davis. "Nonlinear theory of film rupture". In: *Journal of Colloid and Interface Science* 90.1 (1982), pp. 220–228.
- [76] Alexander Oron, Stephen H Davis, and S George Bankoff. "Long-scale evolution of thin liquid films". In: *Reviews of modern physics* 69.3 (1997), p. 931.
- [77] Günter Reiter et al. "Thin film instability induced by long-range forces". In: *Langmuir* 15.7 (1999), pp. 2551–2558.
- [78] Uwe Thiele, Desislava V Todorova, and Hender Lopez. "Gradient dynamics description for films of mixtures and suspensions: dewetting triggered by coupled film height and concentration fluctuations". In: *Physical review letters* 111.11 (2013), p. 117801.
- [79] Noushine Shahidzadeh-Bonn et al. "Salt crystallization during evaporation: impact of interfacial properties". In: *Langmuir* 24.16 (2008), pp. 8599–8605.
- [80] F Lequien et al. "Corrosion influence on the evaporation of sessile droplet". In: *Colloids and Surfaces A: Physicochemical and Engineering Aspects* 546 (2018), pp. 59–66.
- [81] WH Zachariasen. "The crystal lattice of sodium bicarbonate, NaHCO_3 ". In: *The Journal of Chemical Physics* 1.9 (1933), pp. 634–639.
- [82] A Holzwarth, S Leporatti, and H Riegler. "Molecular ordering and domain morphology of molecularly thin triacontane films at SiO_2 /air interfaces". In: *EPL (Europhysics Letters)* 52.6 (2000), p. 653.
- [83] Sergei N Magonov and Natalya A Yerina. "Visualization of nanostructures with atomic force microscopy". In: *Handbook of microscopy for nanotechnology*. Springer, 2005, pp. 113–155.
- [84] Rodrigo Perez-Garcia and Hans Riegler. "Controlled Self-Organized Positioning of Small Aggregates by Patterns of (Sub) nanosized Active Sites". In: *Crystal Growth & Design* 17.4 (2017), pp. 1870–1875.
- [85] H Schollmeyer, B Struth, and H Riegler. "Long chain n-alkanes at SiO_2 /air interfaces: Molecular ordering, annealing, and surface freezing of triacontane in the case of excess and submonolayer coverage". In: *Langmuir* 19.12 (2003), pp. 5042–5051.
- [86] H Schollmeyer, B Ocko, and H Riegler. "Surface freezing of triacontane at SiO_x /air interfaces: Submonolayer coverage". In: *Langmuir* 18.11 (2002), pp. 4351–4355.
- [87] Hans Riegler and Ralf Köhler. "How pre-melting on surrounding interfaces broadens solid–liquid phase transitions". In: *Nature physics* 3.12 (2007), p. 890.
- [88] R Xie et al. "Spinodal dewetting of thin polymer films". In: *Physical Review Letters* 81.6 (1998), p. 1251.
- [89] Stephan Eickelmann et al. "Meniscus shape around nanoparticles embedded in molecularly thin liquid films". 2018.
- [90] Stefan Tenzer et al. "Rapid formation of plasma protein corona critically affects nanoparticle pathophysiology". In: *Nature nanotechnology* 8.10 (2013), p. 772.
- [91] Fangang Meng et al. "Fouling in membrane bioreactors: an updated review". In: *Water research* 114 (2017), pp. 151–180.

- [92] Zhiya Sheng and Yang Liu. "Effects of silver nanoparticles on wastewater biofilms". In: *Water Research* 45.18 (2011), pp. 6039–6050.
- [93] Amir H Bahrami et al. "Wrapping of nanoparticles by membranes". In: *Advances in colloid and interface science* 208 (2014), pp. 214–224.
- [94] Li Shang, Karin Nienhaus, and Gerd Ulrich Nienhaus. "Engineered nanoparticles interacting with cells: size matters". In: *J Nanobiotechnol* 12.5 (2014), b26.
- [95] Wen Jiang et al. "Nanoparticle-mediated cellular response is size-dependent". In: *Nature nanotechnology* 3.3 (2008), p. 145.
- [96] Ralph Weissleder, Matthias Nahrendorf, and Mikael J Pittet. "Imaging macrophages with nanoparticles". In: *Nature materials* 13.2 (2014), p. 125.
- [97] Rachele M Choueiri et al. "Surface patterning of nanoparticles with polymer patches". In: *Nature* 538.7623 (2016), p. 79.
- [98] Anna C Balazs, Todd Emrick, and Thomas P Russell. "Nanoparticle polymer composites: where two small worlds meet". In: *Science* 314.5802 (2006), pp. 1107–1110.
- [99] Terry P Bigioni et al. "Kinetically driven self assembly of highly ordered nanoparticle monolayers". In: *Nature materials* 5.4 (2006), p. 265.
- [100] Marek Grzelczak et al. "Directed self-assembly of nanoparticles". In: *ACS nano* 4.7 (2010), pp. 3591–3605.
- [101] Peter J Yunker et al. "Suppression of the coffee-ring effect by shape-dependent capillary interactions". In: *Nature* 476.7360 (2011), p. 308.
- [102] PH Lizotte et al. "In situ vaccination with cowpea mosaic virus nanoparticles suppresses metastatic cancer". In: *Nature nanotechnology* 11.3 (2016), p. 295.
- [103] Mohammad J Hajipour et al. "Antibacterial properties of nanoparticles". In: *Trends in biotechnology* 30.10 (2012), pp. 499–511.
- [104] Michael R Yeaman. "Platelets in defense against bacterial pathogens". In: *Cellular and molecular life sciences* 67.4 (2010), pp. 525–544.
- [105] Juan Peng et al. "Formation of regular hole pattern in polymer films". In: *Macromolecular Chemistry and Physics* 204.1 (2003), pp. 125–130.
- [106] Deuk Ju Kim, Min Jae Jo, and Sang Yong Nam. "A review of polymer-nanocomposite electrolyte membranes for fuel cell application". In: *Journal of Industrial and Engineering Chemistry* 21 (2015), pp. 36–52.
- [107] P. A. Kralchevsky et al. "Capillary Meniscus Interaction between Colloidal Particles Attachewd to a Liquid-Fluid INterface". In: *Journal of Colloid and Interface Science* 151.1 (1992), p. 79.
- [108] Peter A Kralchevsky and Kuniaki Nagayamaa. "Capillary interactions between particles bound to interfaces, liquid films and biomembranes". In: *Advances in Colloid and Interface Science* 85 (2000), pp. 145–192.
- [109] Jennifer Fiegel et al. "Wetting of a particle in a thin film". In: *Journal of Colloid and Interface Science* 291.2 (2005), pp. 507–514.
- [110] Martin Tress et al. "Shape of a sessile drop on a flat surface covered with a liquid film". In: *Soft matter* 13.20 (2017), pp. 3760–3767.
- [111] Yahachi Saito. "Q Nanoparticles and Nanocapsules". In: *Carbon Nanotubes: Preparation and Properties* (1996), p. 249.
- [112] Jiwen Zheng et al. "Nanopatterned assembling of colloidal gold nanoparticles on silicon". In: *Langmuir* 16.10 (2000), pp. 4409–4412.

- [113] Rongchao Jin, Justin E Jureller, and Norbert F Scherer. "Precise localization and correlation of single nanoparticle optical responses and morphology". In: *Applied physics letters* 88.26 (2006), p. 263111.
- [114] Luca Costa et al. "Real Space Imaging of Nanoparticle Assembly at Liquid-Liquid Interfaces with Nanoscale Resolution". In: *Nano Letters* 16.9 (2016), pp. 5463–5468.
- [115] Yugang Sun and Younan Xia. "Shape-controlled synthesis of gold and silver nanoparticles". In: *Science* 298.5601 (2002), pp. 2176–2179.
- [116] Maria Dienerowitz, Michael Mazilu, and Kishan Dholakia. "Optical manipulation of nanoparticles: a review". In: *Journal of Nanophotonics* 2.1 (2008), pp. 021875–021875.
- [117] Li Li et al. "Single nanoparticle-based heteronanojunction as a plasmon ruler for measuring dielectric thin films". In: *The journal of physical chemistry letters* 6.12 (2015), pp. 2282–2286.
- [118] Qingshan Wei et al. "Fluorescent imaging of single nanoparticles and viruses on a smart phone". In: *ACS nano* 7.10 (2013), p. 9147.
- [119] GG Daaboul et al. "High-throughput detection and sizing of individual low-index nanoparticles and viruses for pathogen identification". In: *Nano letters* 10.11 (2010), pp. 4727–4731.
- [120] Steven M Scherr et al. "Real-time capture and visualization of individual viruses in complex media". In: *ACS nano* 10.2 (2016), p. 2827.
- [121] Weihua Zhang et al. "Trapping and sensing 10 nm metal nanoparticles using plasmonic dipole antennas". In: *Nano letters* 10.3 (2010), pp. 1006–1011.
- [122] Yue Liu and Cheng Zhi Huang. "Real-time dark-field scattering microscopic monitoring of the in situ growth of single Ag@Hg nanoalloys". In: *ACS nano* 7.12 (2013), pp. 11026–11034.
- [123] Lord Rayleigh. "XX. On the equilibrium of liquid conducting masses charged with electricity". In: *The London, Edinburgh, and Dublin Philosophical Magazine and Journal of Science* 14.87 (1882), pp. 184–186.
- [124] Yves Hennequin et al. "Optical Detection and Sizing of Single Nanoparticles Using Continuous Wetting Films". In: *ACS Nano* 7 (2013), 7601–7609.
- [125] Stefan Karpitschka et al. "Nonintrusive Optical Visualization of Surface Nanobubbles". In: *Phys. Rev. Lett.* 109 (6 Aug. 2012), p. 066102. DOI: 10.1103/PhysRevLett.109.066102. URL: <http://link.aps.org/doi/10.1103/PhysRevLett.109.066102>.
- [126] Eann A Patterson and Maurice P Whelan. "Optical signatures of small nanoparticles in a conventional microscope". In: *Small* 4.10 (2008), pp. 1703–1706.
- [127] Eann A Patterson and Maurice P Whelan. "Tracking nanoparticles in an optical microscope using caustics". In: *Nanotechnology* 19.10 (2008), p. 105502.
- [128] J-M GINESTE et al. "Three-dimensional automated nanoparticle tracking using Mie scattering in an optical microscope". In: *Journal of microscopy* 243.2 (2011), pp. 172–178.
- [129] Ravikiran Attota et al. "Nanoparticle size determination using optical microscopes". In: *Applied Physics Letters* 105.16 (2014), p. 163105.
- [130] Onur Mudanyali et al. "Wide-field optical detection of nanoparticles using on-chip microscopy and self-assembled nanolenses". In: *Nature photonics* 7.3 (2013), nphoton–2012.

- [131] PG De Gennes, F Brochard-Wyart, and D Quéré. *Capillarity and Wetting Phenomena*. Springer, New York, 2004.
- [132] Virginie Soulié et al. "The evaporation behavior of sessile droplets from aqueous saline solutions". In: *Physical Chemistry Chemical Physics* 17.34 (2015), pp. 22296–22303.
- [133] CW Frank et al. "Structure in thin and ultrathin spin-cast polymer films". In: *Science* 273.5277 (1996), pp. 912–915.
- [134] Ronald G. Larson and Timothy J. Rehg. *Spin Coating*. Ed. by Stephan F. Kistler and Peter M. Schweizer. Dordrecht: Springer Netherlands, 1997, pp. 709–734.
- [135] K Norrman, A Ghanbari-Siahkali, and NB Larsen. "6 Studies of spin-coated polymer films". In: *Annual Reports Section "C" (Physical Chemistry)* 101 (2005), pp. 174–201.
- [136] Dylan E Haas et al. "Effect of solvent evaporation rate on skin formation during spin coating of complex solutions". In: *Sol-Gel Optics V*. Vol. 3943. International Society for Optics and Photonics. 2000, pp. 280–285.
- [137] Pierre Gilles De Gennes. "Solvent evaporation of spin cast films: "crust" effects". In: *The European Physical Journal E: Soft Matter and Biological Physics* 7.1 (2002), pp. 31–34.
- [138] Sadao Shimoji. "A new analytical model for spin coating process with solvent evaporation". In: *Japanese journal of applied physics* 26.6A (1987), p. L905.
- [139] Samson A Jenekhe. "Effects of solvent mass transfer on flow of polymer solutions on a flat rotating disk". In: *Industrial and engineering chemistry fundamentals* 23.4 (1984), pp. 425–432.
- [140] B Reisfeld, SG Bankoff, and SH Davis. "The dynamics and stability of thin liquid films during spin coating. I. Films with constant rates of evaporation or absorption". In: *Journal of applied physics* 70.10 (1991), pp. 5258–5266.
- [141] B Reisfeld, SG Bankoff, and SH Davis. "The dynamics and stability of thin liquid films during spin coating. II. Films with unit-order and large Peclet numbers". In: *Journal of applied physics* 70.10 (1991), pp. 5267–5277.
- [142] Sadao Shimoji. "Numerical analysis of the spin-coating process". In: *Journal of Applied Physics* 66.6 (1989), pp. 2712–2718.
- [143] RG Picknett and R Bexon. "The evaporation of sessile or pendant drops in still air". In: *Journal of Colloid and Interface Science* 61.2 (1977), pp. 336–350.
- [144] KS Birdi, DT Vu, and A Winter. "A study of the Evaporation Rates of Small Water Drops Placed on a Solid Surface". In: *The Journal of Physical Chemistry* 93 (1989), pp. 3702–3703.
- [145] C Mathew Mate and VJ Novotny. "Molecular conformation and disjoining pressure of polymeric liquid films". In: *The Journal of chemical physics* 94.12 (1991), pp. 8420–8427.
- [146] DE Bornside, CW Macosko, and LE Scriven. "Spin coating of a PMMA/chlorobenzene solution". In: *Journal of The Electrochemical Society* 138.1 (1991), pp. 317–320.
- [147] George DJ Phillies. "Hydrodynamic scaling of viscosity and viscoelasticity of polymer solutions, including chain architecture and solvent quality effects". In: *Macromolecules* 28.24 (1995), pp. 8198–8208.
- [148] WG Cochran. "The flow due to a rotating disc". In: *Mathematical Proceedings of the Cambridge Philosophical Society*. Vol. 30. 3. Cambridge University Press. 1934, pp. 365–375.

- [149] Beatrice Guerrier et al. "Drying kinetics of polymer films". In: *AIChE Journal* 44.4 (1998), pp. 791–798.
- [150] MORIO OKAZAKI et al. "Drying mechanism of coated film of polymer solution". In: *Journal of Chemical Engineering of Japan* 7.2 (1974), pp. 99–105.
- [151] BD Washo. "Rheology and modeling of the spin coating process". In: *IBM Journal of Research and Development* 21.2 (1977), pp. 190–198.
- [152] JJ Hernandez et al. "Structure and morphology of thin films of linear aliphatic polyesters prepared by spin-coating". In: *Langmuir* 26.13 (2010), pp. 10731–10737.
- [153] A Weill and E Dechenaux. "The spin-coating process mechanism related to polymer solution properties". In: *Polymer Engineering & Science* 28.15 (1988), pp. 945–948.
- [154] Sasha Y Heriot and Richard AL Jones. "An interfacial instability in a transient wetting layer leads to lateral phase separation in thin spin-cast polymer-blend films". In: *Nature materials* 4.10 (2005), p. 782.
- [155] Paul C Jukes et al. "Time-resolved light scattering studies of phase separation in thin film semiconducting polymer blends during spin-coating". In: *Macromolecules* 38.6 (2005), pp. 2030–2032.
- [156] P Mokarian-Tabari et al. "Quantitative evaluation of evaporation rate during spin-coating of polymer blend films: Control of film structure through defined-atmosphere solvent-casting". In: *The European Physical Journal E* 33.4 (2010), pp. 283–289.
- [157] Stephen Ebbens et al. "In situ imaging and height reconstruction of phase separation processes in polymer blends during spin coating". In: *ACS nano* 5.6 (2011), pp. 5124–5131.
- [158] Daniel TW Toolan et al. "Direct observation of morphological development during the spin-coating of polystyrene–poly (methyl methacrylate) polymer blends". In: *Journal of Polymer Science Part B: Polymer Physics* 51.11 (2013), pp. 875–881.
- [159] Bingbing Sun et al. "Self-Assembly of Ultralong Aligned Dipeptide Single Crystals". In: *ACS nano* 11.10 (2017), pp. 10489–10494.
- [160] Hiromi Minemawari et al. "Inkjet printing of single-crystal films". In: *Nature* 475.7356 (2011), p. 364.
- [161] Frank-J Meyer Zu Heringdorf, MC Reuter, and RM Tromp. "Growth dynamics of pentacene thin films". In: *Nature* 412.6846 (2001), p. 517.
- [162] Bo Tang et al. "Hydrothermal synthesis of ultralong and single-crystalline Cd (OH) 2 nanowires using alkali salts as mineralizers". In: *Inorganic chemistry* 44.8 (2005), pp. 2568–2569.
- [163] Joanna Aizenberg et al. "Direct fabrication of large micropatterned single crystals". In: *Science* 299.5610 (2003), pp. 1205–1208.
- [164] Huayan Yang et al. "All-thiol-stabilized Ag 44 and Au 12 Ag 32 nanoparticles with single-crystal structures". In: *Nature communications* 4 (2013), p. 2422.
- [165] Michael J Burek et al. "High quality-factor optical nanocavities in bulk single-crystal diamond". In: *Nature communications* 5 (2014), p. 5718.
- [166] Pengli Zhu et al. "Solvent-Induced Structural Transition of Self-Assembled Dipeptide: From Organogels to Microcrystals". In: *Chemistry-A European Journal* 16.10 (2010), pp. 3176–3183.
- [167] Lang Jiang et al. "Single-crystalline, size, and orientation controllable nanowires and ultralong microwires of organic semiconductor with strong

- photoswitching property". In: *Journal of the American Chemical Society* 130.12 (2008), pp. 3937–3941.
- [168] Christos D Dimitrakopoulos and Patrick RL Malenfant. "Organic thin film transistors for large area electronics". In: *Advanced materials* 14.2 (2002), pp. 99–117.
- [169] Alejandro L Briseno et al. "Patterning organic single-crystal transistor arrays". In: *Nature* 444.7121 (2006), p. 913.
- [170] Lihi Adler-Abramovich et al. "Self-assembled arrays of peptide nanotubes by vapour deposition". In: *Nature nanotechnology* 4.12 (2009), p. 849.
- [171] Charlotte AE Hauser and Shuguang Zhang. "Nanotechnology: peptides as biological semiconductors". In: *Nature* 468.7323 (2010), p. 516.
- [172] Shuguang Zhang. "Fabrication of novel biomaterials through molecular self-assembly". In: *Nature biotechnology* 21.10 (2003), p. 1171.
- [173] Hongwei Duan et al. "Directing self-assembly of nanoparticles at water/oil interfaces". In: *Angewandte Chemie International Edition* 43.42 (2004), pp. 5639–5642.
- [174] Hongwei Duan et al. "Magnetic colloidosomes derived from nanoparticle interfacial self-assembly". In: *Nano letters* 5.5 (2005), pp. 949–952.
- [175] Katsuhiko Ariga et al. "Enzyme nanoarchitectonics: organization and device application". In: *Chemical Society Reviews* 42.15 (2013), pp. 6322–6345.
- [176] Rein V Ulijn and Andrew M Smith. "Designing peptide based nanomaterials". In: *Chemical Society Reviews* 37.4 (2008), pp. 664–675.
- [177] Yuri Lvov and Elshad Abdullayev. "Functional polymer–clay nanotube composites with sustained release of chemical agents". In: *Progress in Polymer Science* 38.10–11 (2013), pp. 1690–1719.
- [178] Aleksandra P Dabkowska et al. "Fluid and highly curved model membranes on vertical nanowire arrays". In: *Nano letters* 14.8 (2014), pp. 4286–4292.
- [179] Katsuhiko Ariga, Taizo Mori, and Jonathan P Hill. "Mechanical control of nanomaterials and nanosystems". In: *Advanced materials* 24.2 (2012), pp. 158–176.
- [180] Mao Li et al. "Paradigm shift from self-assembly to commanded assembly of functional materials: recent examples in porphyrin/fullerene supramolecular systems". In: *Science and technology of advanced materials* 13.5 (2012), p. 053001.
- [181] Tao Li et al. "Biomolecular assembly of thermoresponsive superlattices of the tobacco mosaic virus with large tunable interparticle distances". In: *Angewandte Chemie International Edition* 52.26 (2013), pp. 6638–6642.
- [182] Thomas O Mason et al. "Expanding the solvent chemical space for self-assembly of dipeptide nanostructures". In: *ACS nano* 8.2 (2014), pp. 1243–1253.
- [183] Aviad Levin et al. "Ostwald's rule of stages governs structural transitions and morphology of dipeptide supramolecular polymers". In: *Nature communications* 5 (2014), p. 5219.
- [184] Jin-Qiu Lin, Shi-Wei Luo, and Yun-Dong Wu. "Theoretical study of sheets formed by β -peptides". In: *Journal of computational chemistry* 23.16 (2002), pp. 1551–1558.
- [185] Yun-Dong Wu and De-Ping Wang. "Theoretical studies of β -peptide models". In: *Journal of the American Chemical Society* 120.51 (1998), pp. 13485–13493.

- [186] Xuehai Yan, Pengli Zhu, and Junbai Li. "Self-assembly and application of diphenylalanine-based nanostructures". In: *Chemical Society Reviews* 39.6 (2010), pp. 1877–1890.
- [187] Xuehai Yan, Junbai Li, and Helmuth Möhwald. "Self-Assembly of Hexagonal Peptide Microtubes and Their Optical Waveguiding". In: *Advanced Materials* 23.25 (2011), pp. 2796–2801.
- [188] Lihi Adler-Abramovich and Ehud Gazit. "The physical properties of supramolecular peptide assemblies: from building block association to technological applications". In: *Chemical Society Reviews* 43.20 (2014), pp. 6881–6893.
- [189] Ehud Gazit. "Peptide nanostructures: Aromatic dipeptides light up". In: *Nature nanotechnology* 11.4 (2016), p. 309.
- [190] Stephan F Kistler, Peter M Schweizer, et al. "Liquid film coating". In: *Chapman Hall* (1997).
- [191] K Jradi et al. "Enhancing nucleation and controlling crystal orientation by rubbing/scratching the surface of a thin polymer film". In: *The European Physical Journal E* 29.4 (2009), pp. 383–389.
- [192] AV Markov et al. "Comparison of deep levels spectra and electrical properties of GaAs crystals grown by vertical Bridgeman and by liquid encapsulated Czochralski methods". In: *Solid-State Electronics* 46.2 (2002), pp. 269–277.
- [193] Aviad Levin et al. "Elastic instability-mediated actuation by a supramolecular polymer". In: *Nature Physics* 12.10 (2016), p. 926.
- [194] B Levich and L Landau. "Dragging of liquid by a plate". In: *Acta Physiochim* 17 (1942), 42–54.
- [195] Xuehai Yan et al. "Uniaxially oriented peptide crystals for active optical waveguiding". In: *Angewandte Chemie International Edition* 50.47 (2011), pp. 11186–11191.
- [196] Bingbing Sun et al. "Directed Self-Assembly of Dipeptide Single Crystal in A Capillary". In: *ACS nano* (2018).
- [197] Yu Huang et al. "Directed assembly of one-dimensional nanostructures into functional networks". In: *Science* 291.5504 (2001), pp. 630–633.
- [198] Deirdre O'carroll, Ingo Lieberwirth, and Gareth Redmond. "Microcavity effects and optically pumped lasing in single conjugated polymer nanowires". In: *Nature nanotechnology* 2.3 (2007), p. 180.
- [199] Guillaume Crosnier et al. "Hybrid indium phosphide-on-silicon nanolaser diode". In: *Nature Photonics* 11.5 (2017), p. 297.
- [200] Kuiqing Peng et al. "Uniform, Axial-Orientation Alignment of One-Dimensional Single-Crystal Silicon Nanostructure Arrays". In: *Angewandte Chemie International Edition* 44.18 (2005), pp. 2737–2742.
- [201] Do Hwan Kim et al. "High-mobility organic transistors based on single-crystalline microribbons of triisopropylsilylethynyl pentacene via solution-phase self-assembly". In: *Advanced Materials* 19.5 (2007), pp. 678–682.
- [202] Vikram C Sundar et al. "Elastomeric transistor stamps: reversible probing of charge transport in organic crystals". In: *Science* 303.5664 (2004), pp. 1644–1646.
- [203] Yong Sheng Zhao et al. "Low-Dimensional Nanomaterials Based on Small Organic Molecules: Preparation and Optoelectronic Properties". In: *Advanced Materials* 20.15 (2008), pp. 2859–2876.

- [204] Qingxin Tang et al. "Micrometer-and nanometer-sized organic single-crystalline transistors". In: *Advanced Materials* 20.15 (2008), pp. 2947–2951.
- [205] Ling Zang, Yanke Che, and Jeffrey S Moore. "One-dimensional self-assembly of planar π -conjugated molecules: adaptable building blocks for organic nanodevices". In: *Accounts of chemical research* 41.12 (2008), pp. 1596–1608.
- [206] Galit Fichman et al. "Spontaneous structural transition and crystal formation in minimal supramolecular polymer model". In: *Science advances* 2.2 (2016), e1500827.
- [207] Meital Reches and Ehud Gazit. "Casting metal nanowires within discrete self-assembled peptide nanotubes". In: *Science* 300.5619 (2003), pp. 625–627.
- [208] He Zhang et al. "Enzyme-Responsive Release of Doxorubicin from Monodisperse Dipeptide-Based Nanocarriers for Highly Efficient Cancer Treatment In Vitro". In: *Advanced Functional Materials* 25.8 (2015), pp. 1193–1204.
- [209] Qianli Zou et al. "Biological photothermal nanodots based on self-assembly of peptide–porphyrin conjugates for antitumor therapy". In: *Journal of the American Chemical Society* 139.5 (2017), pp. 1921–1927.
- [210] Xingcen Liu et al. "Transformation of Dipeptide-Based Organogels into Chiral Crystals by Cryogenic Treatment". In: *Angewandte Chemie* 129.10 (2017), pp. 2704–2707.
- [211] Qi Li et al. "Controlled rod nanostructured assembly of diphenylalanine and their optical waveguide properties". In: *ACS nano* 9.3 (2015), pp. 2689–2695.
- [212] Partha Bairi et al. "Supramolecular differentiation for construction of anisotropic fullerene nanostructures by time-programmed control of interfacial growth". In: *ACS nano* 10.9 (2016), pp. 8796–8802.
- [213] Abraham JP Teunissen et al. "Scope and limitations of supramolecular autoregulation". In: *Bulletin of the Chemical Society of Japan* 89.3 (2016), pp. 308–314.
- [214] Makoto Sakurai, Pradyot Koley, and Masakazu Aono. "A new approach to molecular self-assembly through formation of dipeptide-based unique architectures by artificial supersaturation". In: *Chemical Communications* 50.83 (2014), pp. 12556–12559.
- [215] Juan Wang et al. "Trace solvent as a predominant factor to tune dipeptide self-assembly". In: *ACS nano* 10.2 (2016), pp. 2138–2143.
- [216] Juan Wang et al. "Peptide self-assembly: thermodynamics and kinetics". In: *Chemical Society Reviews* 45.20 (2016), pp. 5589–5604.
- [217] Juan Wang et al. "Trace Water as Prominent Factor to Induce Peptide Self-Assembly: Dynamic Evolution and Governing Interactions in Ionic Liquids". In: *Small* 13.44 (2017).
- [218] Mingxian Liu et al. "Stripe-like clay nanotubes patterns in glass capillary tubes for capture of tumor cells". In: *ACS applied materials & interfaces* 8.12 (2016), pp. 7709–7719.
- [219] Carl Henrik Görbitz and Frode Rise. "Template-directed supramolecular assembly of a new type of nanoporous peptide-based material". In: *Journal of Peptide Science* 14.2 (2008), pp. 210–216.
- [220] S Zschiegner et al. "Pore opening effects and transport diffusion in the Knudsen regime in comparison to self-(or tracer-) diffusion". In: *EPL (Europhysics Letters)* 78.2 (2007), p. 20001.
- [221] DS Scott and FAL Dullien. "Diffusion of ideal gases in capillaries and porous solids". In: *AIChE Journal* 8.1 (1962), pp. 113–117.

-
- [222] W.G. Pollard and Richard David Present. "On gaseous self-diffusion in long capillary tubes". In: *Physical Review* 73.7 (1948), p. 762.
- [223] Qi Li et al. "Self-Assembly of Cationic Dipeptides Forming Rectangular Microtubes and Microrods with Optical Waveguiding Properties". In: *Advanced Optical Materials* 3.2 (2015), pp. 194–198.
- [224] Márcia I Souza et al. "The role of water and structure on the generation of reactive oxygen species in peptide/hypericin complexes". In: *Journal of Peptide Science* 20.7 (2014), pp. 554–562.
- [225] C Merkl, T Pfohl, and H Riegler. "Influence of the molecular ordering on the wetting of SiO₂/air interfaces by alkanes". In: *Physical review letters* 79.23 (1997), p. 4625.

Acknowledgements

First of all I would like to thank Hans Riegler for the possibility to develop this thesis at the Max Planck Institute of Colloids and Interfaces. I am also obliged to him for his enthusiastic, tireless discussions, that have lead to a profound understanding of the presented phenomena. Also, I enjoyed the great freedom I had to realize my own ideas.

I am indebted to my colleague and friend José Dangel-Flores, for his enduring support in the lab, his expertise in drinking and preparing coffee, and his company during uncountable amounts of experiments. It is a great pleasure to also thank my current and former colleagues from the whole "Riegler-Group", Guoxiang Chen, Rodrigo Perez-Gracia, Marie Jennain, Stefan Karpitschka and Chenyu Jin, and all the others, who shared many hours with me in the cramped lab, and never-ending scientific discussions in the "coffee-corner-group-meetings". I would like to thank my colleague Guoxiang, who recently left to China on his way to Canada, for his collaboration and preparation of nanoparticle. Great thanks to Stefan, supervising me during my master thesis and to prepare my path in designing my own experiments, and to Marie, in being the most heart-full french person i ever met. And I hope Chenyu can now finally remember the correct spelling of my first name. All other colleagues from the MPIKG, I owe many thanks for the friendly and cooperative atmosphere, and the enjoyable summer schools.

I thank Bingbing Sun, who visited our group for a research stay, for a fruitful collaboration leading up to a couple of publications in high impact journals and Jumbai Li for the interesting and nice collaboration. My special thanks are to Stephanie Riedel, for her great assistance in all administrative belongings, Jeanette Ziegler at the University of Potsdam, for her help with the administrative hurdles submitting my thesis, and to Andreas Kretzschmar, Marco Bott and Mike Born from the mechanics and electrics workshop. Most of the data in this thesis were generated on the wonderful precise tools made by them. I'm indebted to my new group for their support in the last stages of writing this thesis. Especially to Jasmin Heideprim, for supplying me with the needed brain-food in form of chocolate and gummy bears! I also would like to acknowledge the financial and institutional support from Prof. Reinhard Lipowsyky.

Last but not least I would like to thank my friends and especially my family, for all the good time and their understanding for the absent-minded physicist. But most importantly I am truly indebted and thankful to my partner selflessly supporting me in all aspects of life.

Eidesstattliche Erklärung

Hiermit versichere ich, Stephan Felix EICKELMANN, die vorliegende Arbeit „Experimental Study of Liquid Interfaces with Compositional Gradients - Distortion & Rupture of Ultra-Thin Films and Other Effects“ selbstständig und nur unter Verwendung der angegebenen Quellen und Hilfsmittel angefertigt zu haben. Übernommene Textstellen sind als solche gekennzeichnet.

Des Weiteren erkläre ich die Kenntnisnahme der dem angestrebten Verfahren zugrunde liegende Promotionsordnung. Ich habe die Arbeit an keiner anderen Hochschule vorgelegt und mich zu keinem früheren Zeitpunkt um ein Doktorgrad beworben.

Potsdam, Juni 2018

Stephan Felix EICKELMANN